TECHNISCHE UNIVERSITÄT WIEN
Vienna University of Technology

Diese Dissertation haben begutachtet:

Ao.Univ.Prof. Dipl.-Ing. Dr.techn. Martin Gröschl

Ass.Prof. Priv.Doz. Dr. Stefan Greisenegger

DISSERTATION

Noninvasive Acoustic Response Analysis of Microbubbles in Biological Tissue

ausgeführt zum Zwecke der Erlangung des akademischen Grades eines
Doktors der technischen Wissenschaften

unter der Leitung von

Ao.Univ.Prof. Dipl.-Ing. Dr.techn. Martin Gröschl
Institut für Angewandte Physik (E134)
Technische Universität Wien

und

Associate Professor Thilo Hölscher, M.D.
BURL Concepts, Inc.
San Diego, Kalifornien

eingereicht an der Technischen Universität Wien
Fakultät für Physik

von

Dipl.-Ing. Maximilian Dirnbacher
Matrikelnummer: 0530484
Steckhovengasse 3
1130 Wien

Wien, im Mai 2016

(Dipl.-Ing. Maximilian Dirnbacher)

TECHNISCHE UNIVERSITÄT WIEN
Vienna University of Technology

DISSERTATION

Noninvasive Acoustic Response Analysis of Microbubbles in Biological Tissue

submitted in partial fulfillment of the requirements for the
Doctor Degree in Technical Sciences

under the supervision of

Ao.Univ.Prof. Dipl.-Ing. Dr.techn. Martin Gröschl
Institute of Applied Physics (E134)
Vienna University of Technology

and

Associate Professor Thilo Hölscher, M.D.
BURL Concepts, Inc.
San Diego, California

to the Vienna University of Technology
Faculty of Physics

by

Dipl.-Ing. Maximilian Dirnbacher
Registration Number: 0530484
Steckhovengasse 3
1130 Vienna

Statement of Authorship

Dipl.-Ing. Maximilian Dirnbacher

I hereby certify that this dissertation has been composed by myself, and describes my own work, unless otherwise acknowledged in the text. All references and verbatim extracts have been quoted, and all sources of information have been specifically acknowledged. It has not been accepted in any previous application for a degree.

Date	Dipl.-Ing. Maximilian Dirnbacher

Acknowledgements

Three years ago, I was given the grand opportunity to do research for this dissertation in the start-up company BURL Concepts, Inc. in San Diego, California. With this regard, I owe my deepest gratitude to Prof. Martin Gröschl who encouraged me to participate in the doctoral program and continued being my advisor from the Vienna University of Technology, immediately after I received my Master's degree.

Research at BURL Concepts, Inc. would not have been possible without its founders Prof. Thilo Hölscher and Dr. James Brailean. I would like to thank them both for involving me in something that has the potential to help many people all over the world. In particular, Prof. Hölscher has been unwavering in his personal and professional support since I first got to know him, for which I am deeply grateful. May our friendship continue to evolve and grow! It was an honor to learn from a great businessman like Dr. Brailean, not only from an economic perspective. With his electrical engineering background, he passed on his extremely valuable expertise (including the hazard of using square waves) to the entire research team. Furthermore, I very much appreciate having such competent coworkers, who were always willing to help when the need arose.

The biggest gratitude I owe to my family, who supported me on this road of life with all their energy, to my friends, that I can always count on and to my gorgeous girlfriend (best friend and family), Katharina, who never has left my side supporting me in any possible way.

Abstract

The broad range of neurological brain diseases, e.g. *stroke* or several neurodegenerative diseases such as Alzheimer's disease, emphasizes the importance to develop innovative, affordable medical care solutions for present and future generations in the field of neuroscience. *Noninvasive transcranial ultrasound* for diagnostic and potential therapeutic purposes shows great promise in this regard. The performed studies help to understand the fundamental mechanisms and effects of transcranial ultrasound, especially in combination with *microbubbles*, tiny gaseous bodies that are commonly used as contrast agents in diagnostic ultrasound, such as liver imaging or assessment of cardiovascular functions[10].

Extensive analysis of acoustic responses by microbubbles and human tissue to 220 kHz ultrasound with low acoustic intensities ($\ll$100 mW/cm^2) was the main objective of this project in order to lay the foundation to a variety of innovative ultrasound applications, which are not imaging technologies. Despite complete characterization of our customized transducers used for the entire research activities, results provide an exceptional content of information about the basic anatomy of a human skull and its impact on the properties of the acoustic field. This includes in-vitro measurements with customized transducers and hydrophones, devices to receive acoustic pressure waves underwater. In the following, microbubbles are included in experiments. Upon excitation with ultrasound, depending on the acoustic intensity, microbubbles will either scatter the incident wave or start oscillating, thereby emitting so called *harmonics*. Physics behind microbubbles and human tissue behavior during ultrasound exposure is in general well understood. However, this accounts for acoustic excitation at working frequencies used in medical imaging, which are usually higher than 1 MHz. Only very little is known about the effect of lower frequencies on acoustic responses[1]. Last but not least, we proof the safety of our transducers in in-vivo studies on rabbits and apply them for the first time on postmortem cadaver heads with the goal to examine tissue responses.

All in all, transcranial ultrasound provides many intriguing pathways in both diagnostic and treatment oriented. This research, however, represents a novelty in diagnostic, non-imaging, ultrasound and is the basis to technologies with the potential to significantly improve today's health-care.

Kurzfassung

Erkrankungen des menschlichen Gehirns wie der *Schlaganfall* oder längerfristige pathologische Zustände wie Alzheimer machen es nötig, Forschung auf dem Gebiet der Neurowissenschaften voranzutreiben. In der heutigen Medizin bedarf es der Entwicklung innovativer, effizienter und kostengünstiger Methoden, um betroffenen Personen zu helfen. Mit *nichtinvasivem trasnkraniellem* Ultraschall ist eine Möglichkeit gegeben, oben angeführte Erkrankungen zu diagnostizieren und in der Folge zu behandeln. In den zugrundeliegenden Forschungstätigkeiten werden deshalb die akustischen Effekte von transkraniellem Ultraschall auf biologisches Gewebe untersucht. Besondere Aufmerksamkeit wird dabei dem durch *Mikrobläschen* kontrastmittelverstärktem Ultraschall gewidmet, der heutzutage in bildgebenden Verfahren zur Darstellung von Leber- und Herzfunktionen verwendet wird [10].

Im Gegensatz zu den meisten Ultraschalltechniken verwenden wir für alle Messungen eine niedrige Frequenz von 220 kHz, sowie eine geringe akustische Intensität von unter 100 mW/cm^2. Die Auswirkungen dieser Parameter auf die akustischen Antworten von Mikrobläschen sowie des menschlichen Gewebes sind von größter Relevanz, da sie das Fundament für eine erfolgreiche Entwicklung innovativer, nicht bildgebender Ultraschallverfahren legen.

Zunächst charakterisieren wir Schallköpfe, die eigens für unseren Gebrauch angefertigt wurden, hinsichtlich ihrer akustischen Eigenschaften. Die darauffolgenden Studien helfen die Auswirkungen des menschlichen Schädelknochens auf die akustischen Feldparameter zu verstehen. Die Experimente werden dann durch Mikrobläschen ergänzt, die bei Anwendung von Ultraschall verschiedene akustische Antworten geben. Bei niedrigen Intensitäten können Mikrobläschen als Streuobjekte behandelt werden. Im Gegensatz dazu sind bei höheren Intensitäten Schwingungen der Bläschen zu erwarten, die so genannte *Harmonische* zur Folge haben. Zahlreiche Forschungsarbeiten beschreiben den zugrundeliegenden physikalischen Mechanismus der Mikrobläschen. Dies gilt aber nur für kontrastmittelverstärkten, bildgebenden Ultraschall von höherer Frequenz (<1 MHz). Die Auswirkung von niederen Frequenzen auf akustische Signale ist im Gegensatz dazu nicht gut erforscht [1]. Des Weiteren beweisen wir die Sicherheit unserer Anwendung an einem Kaninchenmodell und untersuchen schlussendlich akustische Signale, die wir aus Studien an menschlichen Leichen erhalten.

Das im Rahmen dieser Dissertation angeeignete Wissen stellt die Grundlage einer Vielfalt an diagnostischen als auch therapeutischen Ultraschallanwendungen in der Medizin dar. Im Speziellen ermöglicht die durchgeführte Forschungsarbeit die Entwicklung von innovativen, diagnostischen und nicht bildgebenden Verfahren, die mit nichtinvasivem, transkraniellem Ultraschall funktionieren.

Contents

1 Introduction **1**
1.1 Transcranial Ultrasound . . . 1
1.2 Stroke . . . 2
1.3 Stroke Diagnosis and Treatment with Ultrasound . . . 4
1.4 Diagnostic Ultrasound and biological Structures . . . 5
1.4.1 Acoustic Parameters . . . 5
1.4.2 Thermal and Mechanical Effects . . . 5
1.4.3 The Safety Aspect . . . 6
1.5 Ultrasound Transducers . . . 7
1.5.1 Characteristics of Piezoelectric Materials for Ultrasound Transducers . 7
1.5.1.a PZT . . . 9
1.5.1.b PVDF . . . 9
1.5.2 Electrical and Mechanical Coupling of Elements . . . 10
1.5.3 Beam Characteristics . . . 10
1.6 Wave Propagation Theory . . . 11
1.6.1 Linear and Nonlinear Wave Propagation . . . 12
1.6.2 Cavitation . . . 14
1.6.3 Harmonics . . . 14
1.7 Signal Analysis . . . 15
1.7.1 Pulse Inversion . . . 15
1.7.2 Matched Filter . . . 16

2 Methodology **17**
2.1 Research Objects . . . 17
2.1.1 Microbubbles . . . 17
2.1.2 Human Cadaver Skulls . . . 17
2.1.3 Rabbits for Safety Studies . . . 18
2.1.4 Acrylic Chamber . . . 18
2.1.5 Postmortem Tissue . . . 18
2.2 Research Instruments . . . 18
2.2.1 Transducer . . . 18
2.2.1.a Transmitter . . . 19
2.2.1.b Receiver . . . 21

2.2.2 Analog Filters . . . 22
2.2.3 Acoustic Intensity Measurement System . . . 26
2.2.4 Function Generator . . . 27
2.2.5 Oscilloscope . . . 27
2.2.6 Listening Devices . . . 27
2.2.7 PXI platform . . . 28
2.2.7.a NI Arbitrary Waveform Generator . . . 28
2.2.7.b NI Data Acquisition Module . . . 28
2.2.8 Power Amplifier . . . 28
2.2.9 Soniq . . . 29
2.2.10 MATLAB . . . 30
2.2.11 LabVIEW . . . 30
2.3 Research Algorithms . . . 30
2.4 Experimental Parameters . . . 33
2.4.1 Waveform . . . 33
2.4.2 Duty Cycle . . . 33
2.4.3 Measurement Time . . . 34
2.4.4 Ramp-Up . . . 34
2.4.5 Pulse Inversion . . . 34
2.4.6 Transmit Configuration . . . 34
2.4.7 Acquisition Configuration . . . 35
2.5 Transducer Characterization . . . 36
2.5.1 Impedance Measurements . . . 36
2.5.2 3D Acoustic Field Scans and Efficiency Measurements . . . 36
2.5.3 Sensitivity . . . 38
2.5.4 Time and Frequency Domain Analysis . . . 39
2.6 Mechanical Index, Thermal Index Cranial and Intensity . . . 39
2.7 Transcranial Field Assessments . . . 40
2.8 In-Vitro Acoustic Response Studies . . . 42
2.8.1 Skull Response Studies . . . 42
2.8.2 Microbubble Response Studies in AIMS tank . . . 43
2.8.3 Microbubble Response Studies with Acrylic Chamber . . . 45
2.9 Animal Safety Studies . . . 46
2.10 Human Cadaver Studies . . . 48
2.11 Acoustic Response Analysis in LabVIEW . . . 50

3 Results **55**
3.1 Transducer Characterization . . . 55
3.1.1 Impedance Measurements . . . 55
3.1.2 Field Characterization . . . 60
3.1.2.a Transducer 4.1 Efficiency . . . 60
3.1.2.b Transducer 4.2 Efficiency . . . 60
3.1.2.c Transducer 5.1 Efficiency . . . 60

3.1.2.d Transducer 5.2 Efficiency 60
3.1.2.e Transducer 5.2 Sensitivity 65
3.1.3 Analysis of Time Signal and individual Frequency Components 69
3.2 Mechnical Index, Thermal Index Cranial, Intensity Calculations 71
3.3 In-Vitro Studies 71
3.3.1 Transcranial Studies 71
3.3.1.a Transcranial Field Assessments 71
3.3.1.b Skull Response Studies 76
3.3.2 Microbubble Response Studies in AIMS tank 81
3.3.3 Microbubble Response Studies in Acrylic Chamber 84
3.3.3.a Impact of Transducer driving Voltage on Microbubble Response 84
3.3.3.b Microbubble Dose Escalation Studies 86
3.3.3.c Measurements through Acrylic Chamber Wall 87
3.4 Animal Safety Studies 88
3.4.1 Ultrasound Parameters 88
3.4.2 Animal Safety and Survival Analysis 88
3.4.3 Behavioral Assessment 88
3.5 Human Cadaver Studies 88

4 Discussion and Conclusion 97
4.1 Transducers 97
4.1.1 Impedance Measurements 97
4.1.2 Acoustic Field Properties 97
4.1.3 Time and Frequency Domain Analysis 98
4.2 Critical Ultrasound Parameters 99
4.3 In-Vitro Studies 99
4.3.1 Human Skull Response and Impact 99
4.3.2 Microbubble Response 100
4.3.2.a Studies in AIMS tank 100
4.3.2.b Studies in Acrylic Chamber 100
4.4 Animal Safety Studies 101
4.5 Human Cadaver Studies 101
4.6 Signal Detection and Analytical Methods 102

5 Summary 103
5.1 Transducers 103
5.2 Transcranial Assessments 103
5.3 Microbubbles 103
5.4 Safety Aspect 104
5.5 Human Cadaver Studies 104

6 Outlook 105

Bibliography 107

List of Figures **111**

List of Tables **114**

CHAPTER 1

Introduction

In the past, ultrasound in medicine has reached broad acceptance as it represents one of the safest, most reliable and noninvasive diagnostic procedures worldwide. Beyond the already existing variety of imaging applications in many fields, such as pelvic, cardiovascular, orthopedic or abdominal ultrasound and of methods to monitor basic body functions, e.g. Doppler echocardiography, there is still a need for innovative ultrasound technologies that need to find their way into todays clinical practice in order to help people all over the world.

1.1 Transcranial Ultrasound

Noninvasive transcranial ultrasound, i.e. acoustic waves that penetrate the skull bone, is an important advancement in neuroscience. This includes diagnostic applications that evaluate the neurological condition of a patient, like transcranial Doppler Sonography, as well as therapeutic approaches that create clinical effects at a certain location within the human brain, e.g. transcranial focused ultrasound. Doppler Sonography is used to view intracranial basal artery blood flow, indicating flow speed and direction. This method allows, for example, to detect large occlusions of intracranial vessels (e.g. ischemic strokes) and changes in cerebral perfusion or hemodynamics. Although ultrasound technology has significantly advanced over the past years, Doppler Sonography still lacks in resolution and provides a limited view of the important vessels. In the most cases, experienced sonographers, only, are able to overcome these major drawbacks of the procedure.

Great promise in therapeutic ultrasound show technologies that use focused ultrasound (FUS) to deliver high acoustic pressures to a treatment area within the brain. This includes tumor ablation and the temporary opening of the *blood-brain barrier (BBB)* for targeted drug delivery. The BBB regulates diffusion of therapeutic drugs to the central nervous system and represents a selective barrier for agents that may help treating diseases such as Alzheimer's or Huntington [8]. The necessary acoustic pressure to cause BBB opening was significantly reduced using FUS in combination with microbubbles, tiny gaseous bodies, that are known as contrast agent in medical diagnostic ultrasound (e.g. liver or cardiovascular imaging). However, today, researchers put

effort in getting a better understanding of mechanisms and effects involved in the application of FUS, which is inevitable to guarantee safety of this technology [27].

1.2 Stroke

Stroke is a devastating neurovascular event that happens worldwide to over 15 million people each year. It is the second most common cause of death and the reason for severe disabilities, such as speech disorder, paralysis and sensory and visual loss[7]. Relatives and close friends, too, go through extremely tough times by taking care of the survivors. When it comes to stroke the common phrase *"Time is Brain"* points out the critical time factor, as the human nervous tissue is rapidly lost as stroke progresses.

Neuronal brain cells (neurons) are energetically expensive to maintain as they require constant supply with oxygen and nutrients, e.g. glucose. If deprived longer than 60 seconds, they rapidly start to undergo programmed cell death (apoptosis) in quantity with dramatic consequences for the patient afflicted. This infarct of neuronal tissue and the loss of brain functions due to insufficient metabolism is referred to as stroke[25].

Blood supply of the two brain hemispheres (left and right) originates from a pair of branches, the common carotid and the vertebral arteries. The common carotid arteries give rise to the internal carotid arteries, which in turn bifurcate into the anterior and middle cerebral arteries (Figure 1.1 C). Parts of the frontal and parietal lobe, the rostral part of the temporal lobe, and the *diencephalon* receive blood from the anterior cerebral arteries. Blood supply of the frontal and parietal lobe is provided by the middle cerebral arteries [15]. The basilar artery forms where the left and the right vertebral arteries are joined. At the so called *Circle of Willis* (enlargment of the boxed area in Figure 1.1), the basilar artery and the internal carotid arteries confluence [29]. In addition, at this point, the posterior cerebral arteries as well as the anterior and posterior communicating arteries originate. In the case of an occlusion, the communicating arteries may still be able to preserve brain tissue perfusion (cerebral collateral circulation)[31].

Most common underlying reasons for stroke are *thrombo-embolic* events originating from the heart, where pathologic cardiogenic conditions, such as atrial fibrillation, encourage formation of blood clots (thrombus)[2]. Following the blood stream, such a thrombus may cause sudden occlusion of larger as well as smaller branches, thus obstructing blood supply of certain brain regions (ischemia). So called *ischemic strokes* are most likely to occur within the middle cerebral artery and its branches. In fewer cases, the anterior or posterior cerebral arteries are affected[15]. It is noteworthy, that 80% of victims suffer from ischemic strokes, which is one out of two main types of strokes. Within the other form of stroke, i.e. *hemorrhagic*, rupture of a weakened brain vessel leads to bleeding into surrounding brain tissue usually caused by either aneurysm or arterio-venous malformation [29].

The complex hemodynamics within the brain regulated by the mean arterial blood pressure(ABP), intracranial pressure(ICP) as well as the cerebrovascular impedance that considers vessel radius, viscoelastic properties of arterial walls and blood inductance[25]. An intracerebral hemorrhage is associated with ICP changes due to bleeding within the brain. In fact, during an hemorrhagic event, ICP increases and compresses brain tissue. Similar to an ischemic stroke,

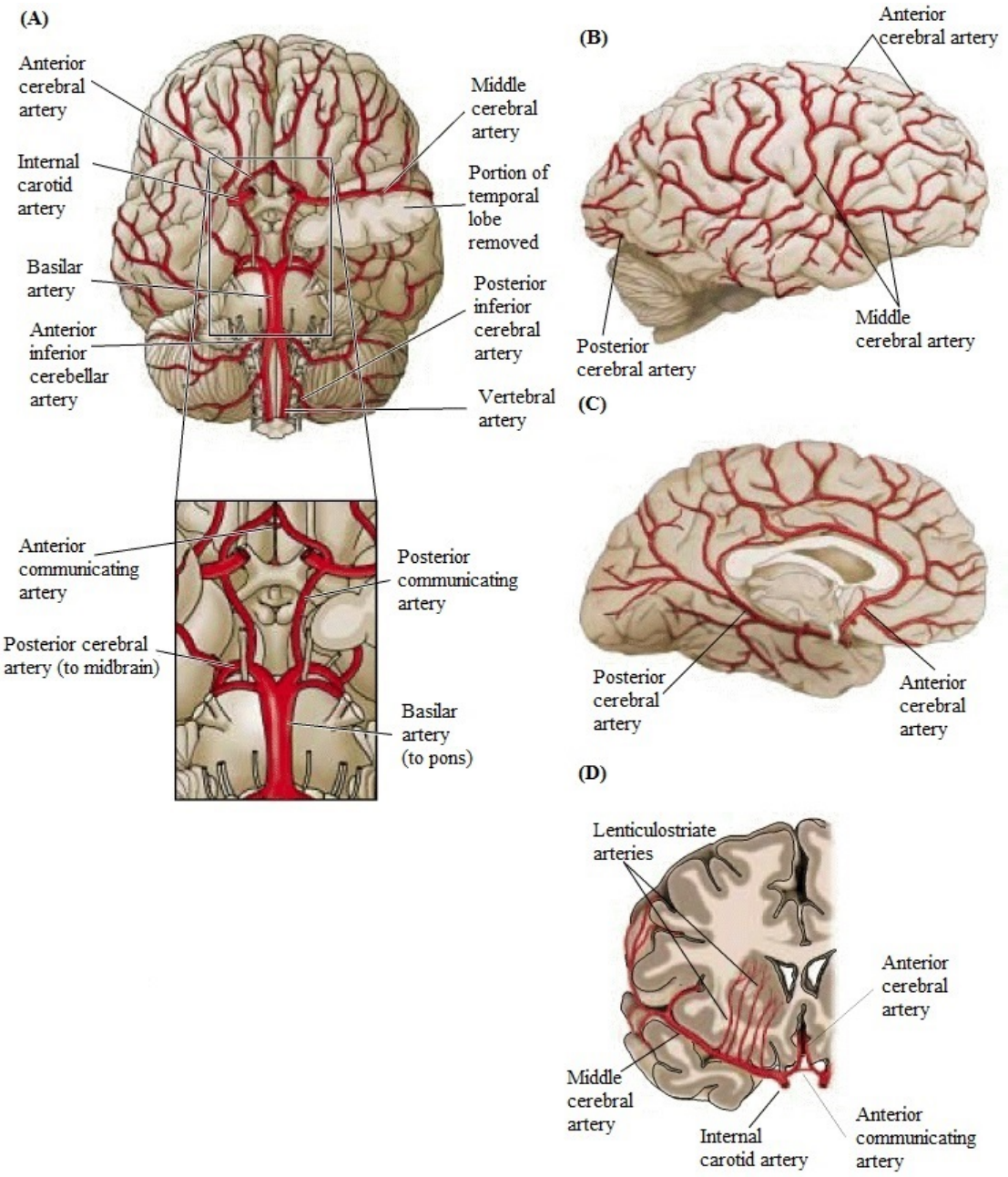

Figure 1.1: The major arteries of the brain. (A) Ventral view. The enlargement of the boxed area shows the circle of Willis. Lateral (B) and (C) midsagittal views showing anterior, middle, and posterior cerebral arteries. (D) Idealized frontal section showing course of middle cerebral artery[29]

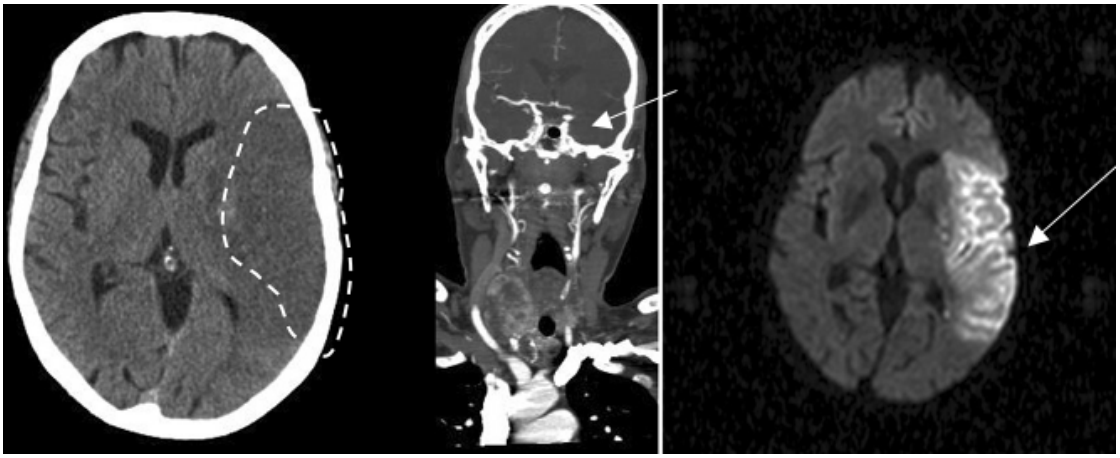

Figure 1.2: Cerebral Infarction Example of a cerebral infarction on the left hemisphere due to a M1 thrombosis of the middle cerebral artery: computed tomography (CT) scan with a demarcation zone (left side), CT angiography which shows a stop of flow (see arrow in the middle), DW MRI (diffusion weighted magnetic resonance imaging) which shows the extend of edema caused in the zone of tissue infarction (courtesy Department of Neuroradiology, Medical University of Vienna)[15]

.

this prevents oxygen and nutrients to reach important brain parts, which ultimately enhances destruction of brain tissue.

1.3 Stroke Diagnosis and Treatment with Ultrasound

The current gold standard to treat strokes is the application of *tissue plasminogen activator(tPA)*, a thrombolytic enzyme, responsible to catalyze the process of blood clot breakdown, thus improving endovascular recanalization, which is necessary to restore brain perfusion. Especially in combination with ultrasound, enhanced treatment efficacy with tPa was demonstrated and discussed within the scope of several research activites [24][32][13]. Nevertheless, treatment with tPa is an extremely regulated procedure as administration to patients who are not eligible to receive tPa may have fatal consequences. Limitations, for example, exclude such patients that suffer from intracranial hemorrhage or those who got diagnosed with stroke later than 4 hours after symptom onset. As a result, recent research and development focuses on innovative technologies, such as neurovascular interventions.

Ultimately, success of stroke treatment relies on the underlying diagnosis and although every minute counts for stroke victims, little effort is dedicated to development of cost effective, safe and fast stroke diagnosis methods. Research done within the scope of this dissertation, lays the foundation for a transcranial ultrasound platform that is used to diagnose strokes on site.

1.4 Diagnostic Ultrasound and biological Structures

In-vivo, complex acoustic responses are not solely tissue-related, they furthermore depend on applied ultrasound parameters (e.g. frequency, amplitude) as well as physiological conditions (e.g. blood circulation).

1.4.1 Acoustic Parameters

Frequency, acoustic pressure and intensity are probably the most important ultrasound parameters to consider when describing possible interactions of ultrasound with biological structures (i.e. bioeffects). Two types of effects, the *thermal* (e.g. tissue heating) and *mechanical* (e.g. cavitation), are mainly related to the parameters frequency and intensity, respectively[12][1][6].

In common therapeutic and diagnostic ultrasound, particularly in imaging modalities, where high axial resolution is demanded, working frequencies are usually within 1 to 20 MHz and it is therefore understandable why research focuses more on this higher range. Although, there are obvious advantages of higher frequencies, such as the improved spatial resolution, a variety of innovative diagnostic and therapeutic ultrasound applications exploit benefits of using lower frequencies (i.e. < 1 MHz), which provide, for example, less thermal effects and higher penetration depth[12].

Another important ultrasound parameter is the *peak negative pressure (PNP)*, which indicates the most negative acoustic pressure of a propagating wave. Based on the PNP, the *spatial peak-temporal average intensity (I_{SPTA})* may be calculated. From a regulatory and safety standpoint, this parameter is of great interest, because it indicates the acoustic power per unit of area (W/cm^2). In order to calculate I_{SPTA}, we first have to determine the *instantaneous acoustic intensity* with

$$I = \frac{PNP^2}{2\rho c} \tag{1.1}$$

considering the propagation medium density ρ as well as the speed of sound c[19]. The spatial peak-temporal average intensity (the average of intensity over time) may then be calculated in the following equation:

$$I_{\text{SPTA}} = Intensity \cdot DC \tag{1.2}$$

where *DC* is the used Duty Cycle[12].

1.4.2 Thermal and Mechanical Effects

Thermal effects become apparent, because of the attenuating character of the propagation medium. An ultrasound wave, traveling through a biological structure will mainly be absorbed and only weakly scattered, whereas attenuation is the sum of both phenomena. The linear frequency dependent [19] attenuation coefficient α (dB/cm) is a tissue-specific parameter that defines the energy loss of a propagating wave due to absorption and scattering. Due to the fact that bone has a large attenuation coefficient α of approximately 20 dB/cm, the thermal effect is higher than for a medium like soft tissue (e.g. fat: 0.6 dB/cm). However, applications using low ultrasound

frequencies are less likely to cause thermal effects in bone than, for example, imaging modalities that operate at frequencies higher than 1 MHz. In addition to its frequency dependency, the magnitude of the thermal effect becomes more prominent at higher intensities[1].

Mechanical effects, on the other side, such as *cavitation* or *acoustic micro-streaming*, depend on intensity, that is related to the acoustic peak negative pressure and considers density of the propagation medium as well as the medium-specific speed of sound. Of all the mechanical effects, cavitation is particularly of importance, because of the potential risk to harm biological tissue. In liquid medium (e.g. blood), high enough acoustic pressure may cause formation of tiny bubbles (i.e. cavities), which will oscillate upon ultrasound excitation (i.e. stable cavitation). If pressure is further increased, the bubbles may grow in size until they violently collapse at a certain pressure threshold (i.e. inertial cavitation). This ultimate event might cause harmful effects to living biological tissue as it is usually accompanied by extreme temperature rise and acoustic pressure release [17].

Both, thermal and mechanical, are ambiguous effects considering, on the one side, their ability to damage tissue, but on the other side, the fact to be viable for therapeutic applications such as thermal ablation of tumors with *high-intensity focused ultrasound(HIFU)*[30][5] or temporary opening of the blood-brain barrier with cavitation for the purpose of targeted drug delivery[39][14].

1.4.3 The Safety Aspect

Any medical application needs to be safe and it is ultimately the manufacturer who is responsible to guarantee safety of the own product. In conventional ultrasound technologies, potential risk of bringing harm to tissue is low in comparison to other methods. However, safety limits for critical parameters exist and are specified by the regulatory agencies such as the *Food and Drug administration(FDA)*[26].

Two *indices*, a *thermal(TI)* and *mechanical(MI)*, have been established as indicators for the likelihood of thermal and mechanical effects caused by ultrasound. The risk of thermal damage by ultrasound is expressed by the thermal index:

$$TI = \frac{W}{W_{\text{deg}}} \tag{1.3}$$

W represents the power input to tissue in Watt and W_{deg} is tissue-specific power to raise the temperature by 1°C in the affected tissue. For applications where the transducer is placed close to the skull bone, the *cranial bone thermal index(TIC)* is indicated. Furthermore, relating PNP and the working frequency f, the mechanical index calculates as follows:

$$MI = \frac{PNP}{\sqrt{f}} \tag{1.4}$$

The mechanical index is the standard acoustic quantity indicating the likelihood of mechanical effects, such as cavitation.

The three parameters *TI, MI* and I_{SPTA} are important from a regulatory point of view. Regulations of the thermal index are not as strict as in the case of the mechanical index. A thermal

index below 6 is in general acceptable, but may be exceeded if justified. Although the occurrence of cavitation is likely at an mechanical index of 0.7[20], FDA, for example, defines a maximum of 1.9. Furthermore, the limit for spatial peak-temporal average intensity is 720 mW/cm^2.

1.5 Ultrasound Transducers

Ultrasound transducers that convert an electrical signal into acoustic wave, and vice versa, exist in various forms. They have to be designed with regard to the used material, geometry as well as costs, but ultimately in view of the application. It is understandable, for example, that non-destructive testing techniques to test pipelines at constructions sides for defects requires rather robust transducers to withstand exposure to rough environments (e.g. temperature fluctuations). On the other side, in medical diagnostics, transducers are mainly used in the hospital and can therefore be designed to generate high-resolution images of biological structures. Especially, in the medical ultrasound field, safety plays a critical role. Applications should therefore be efficient in a way by exposing the human body to the least amount of energy needed to obtain all clinical information.

Energy conversion may be accomplished in different ways, such as by coupling of internal dielectric polarization and strain (i.e. piezoelectricity) or using technologies like capacitive micromachined ultrasonic, electromagnetic acoustic or optical transducers. Ultimately, which transducer principle to use depends on the application.

1.5.1 Characteristics of Piezoelectric Materials for Ultrasound Transducers

In common ultrasound piezoelectric materials dominate current design. Different kinds of such materials are available, whereas they are assigned to one of the four main groups which are *piezoceramics*, *piezocrystals*, *piezopolymers* and *piezocomposites* [9]. Each group offers various advantages and disadvantages with regard to their electromechanical behavior and manufacturing costs. In addition to the material, geometry and electrical properties are critical parameters to be considered in transducer design. Several physical characteristics define a piezoelectric material. The most important are *resonant frequency*, *acoustic impedance*, *coupling coefficients* and *quality factor Q*.

If voltage is applied to a thin piezoelectric disk, assuming outer diameter significantly larger than thickness (20t < D), two types of resonance geometries, i.e. thickness and radial, may be observed (Figure 1.3). In thickness mode waves will propagate in axial direction, whereas radial mode excites in radial direction. In most cases, a transducer is optimized to operate in thickness mode to achieve the highest possible transmission effciency or receiving sensitivity. The presence of radial modes may decrease this ability as it generates unwanted emission of ultrasound energy, i.e. *side lobes* or so called *parasitic vibrations*.

At a certain frequency, which is the resonant frequency, the transducer operates most efficiently. This transducer specific frequency is determined by the thickness of the piezoelectric element. At resonant frequency, the wavelength is exactly twice its thickness, and reverberations propagate between the transducers transmission side and backing layer without causing destruc-

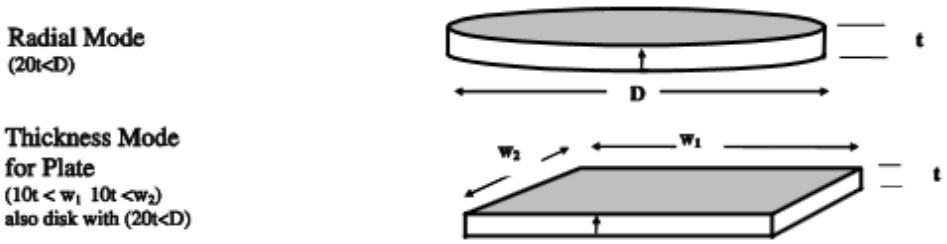

Figure 1.3: Resonance Geometries [34]

tive interference. This implicates optimal conversion from either electrical to mechanical (i.e. transmission) or from mechanical to electrical energy (i.e. reception)[9].

The quality of a transmitted or received ultrasound pulse is expressed by the ratio of the working frequency to the frequency bandwidth of a transducer. The resulting *Q-factor* indicates the sharpness of the frequency response and is determined according to [19] as follows:

$$\mathrm{Q-factor} = \frac{\text{resonant frequency(MHZ)}}{\text{frequency bandwidth(MHZ)}} \tag{1.5}$$

Higher *Q-factors* are usually desirable, which requires trade-offs in either lowering bandwidth or the use of a higher center frequency.

A very important indicator for efficiency is the *coupling coefficient* k_c, which is the ratio of converted *mechanical energy* to input *electrical energy* [19]

$$k_\mathrm{c} = \frac{\text{mechanical energy converted to electrical energy}}{\text{applied mechancial energy}} \tag{1.6}$$

or converted electrical energy to input mechanical energy

$$k_\mathrm{c} = \frac{\text{electrical Energy converted to mechanical energy}}{\text{applied electrical energy}} \tag{1.7}$$

It is important to mention, that the coupling coefficient k_c is not an efficiency factor, but indicates the extent of the piezoelectric effect. Anyways, coupling coefficients in thickness and radial mode differ not only from one to the other piezoelectric material group, there is also variation amongst a group.

The performance furthermore depends on the *acoustic impedance* differences between transducer and medium. Acoustic impedances vary amongst piezoelectric materials. Piezoceramics compared to piezopolymers, for example, have rather high acoustic impedances. Although the coupling coefficient in thickness mode is rather high for piezoceramics, the impedance mismatch

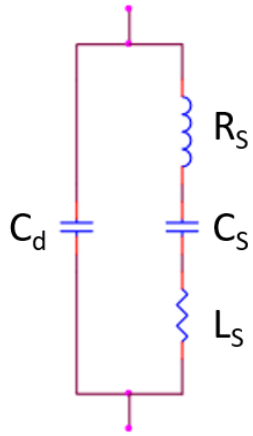

Figure 1.4: Transducer Equivalent Circuit

between a transducer and the medium of propagation, for example water, causes reflections at the boundary from high to low impedance. Usually, the impedance matching layer is designed to have a thickness of 1/4 of the desired wavelength (commonly know as quarter-wavelength acoustic matching layer)[19].

1.5.1.a PZT

Lead zirconate titanate(PZT) is the most common piezoceramic in use today for a variety of medical applications. PZT can be shaped into any configuration and dimensioned precisely in the micrometer to centimeter range. Such elements usually have a high sensitivity and a broad frequency bandwidth. The rather high coupling coefficient makes PZT a very efficient material. However, due to its high density the high acoustic impedance is a disadvantage, but may be overcome by the use impedance matching layers.

Similar to a quartz crystal, the resonant behavior of PZT can be described by an equivalent series RLC circuit (Figure 1.4), that considers dielectric as well as mechanical aspects of the piezoelectric material. Whereas R_S, L_S and C_S describe the mechanical properties, a capacitance C_d in parallel should represent the electrode coated ceramic (i.e. the dielectric). Due to the frequency- dependent impedance of the reactive parts (inductance, capacitance) the reactance in the series branch approaches zero from any value below the resonant frequency. At resonant frequency, the impedance equals the resistance and is therefore a minimum[35]. Increasing the frequency further above the resonant point leads to the so called anti-resonance. At this point the impedance reaches a maximum with the parallel capacitance in resonance.

1.5.1.b PVDF

The piezopolymer *polyvinylidene fluoride(PVDF)* has compared to PZT a low density, flexiblity with regard to geometry and can be manufactured at low costs. In addition, it works over a broad range of frequencies and withstands high pressure without loosing its piezoelectric properties.

In medical imaging PVDF is a popular material as well. Unlike in the case of PZT, acoustic impedances of the polymer and human tissue are way better matched. It is therefore understandable, that todays research focuses on its development. However, if no innovative methods are applied, due to its lower electromechanical coupling coefficient in thickness mode, and increased radial mode, PVDF is usually less sensitive than PZT.

1.5.2 Electrical and Mechanical Coupling of Elements

Although, a single piezoelectric element can accomplish both types of energy conversion due to reciprocity of the piezoelectric effect, in some cases it is preferential to have elements separated and designed for either transmission or reception only. Realistically, a single element transducer will not stop oscillating at the same time as the electric excitation is completed(i.e. ringdown). In this case the transducer is only capable of receiving at highest sensitivity as soon as there is no more ringdown happening. Therefore, dual element transducers in which transmission and receiving element are physically decoupled, are commonly used if the acoustic reflectors are close to transducer. In a so called *monostatic* arrangement of the two elements, where transmitter and receiver are at the same place, ringdown can be significantly decreased. However, proper electrical and mechanical isolation of two elements for monostatic transducers is usually not trivial. [21]. Ringdown happens due to electrical and mechanical coupling (also referred to as *crosstalk*), which are potential problems when it comes to the ability to detect weak acoustic emission with a monostatic transducer arrangements. If the two elements are both connected to the same system, they will interfere electrically. To eliminate electrical coupling, ideally, two elements have to be completely isolated from another, e.g. by proper shielding of cables or ground of the research platform.

Mechanical coupling on the other side occurs due to the physical proximity of different resonant systems. Upon oscillation, a piezoelectric element may excite neighbor elements, too. Eliminating this form of crosstalk is extremely challenging and only possible to some extend, especially in the transducer configuration used for this research (i.e. receiver disk within transmit ring). Mechanical crosstalk becomes in particular a problem if near by objects are the main target of investigation. As mentioned, any piezoelement has a ringdown phase after being active, which will also interfere with surrounding elements. To prevent mechanical coupling, a transducer should have a high *Q-factor* and acoustic damping material (i.e. acoustic barrier) built in between elements that are supposed to work separated. Ultimately, if the application allows it, a monostatic dual element transducer may be split into a bi-static transducer, where transmission and reception happen at different locations [21].

1.5.3 Beam Characteristics

The behavior of a transducer with respect to the generated acoustic field may be described by several field parameters. The knowledge about shape and important parameters, such as intensity or peak negative pressure, of an acoustic field is critical for any ultrasound application. Characterizing an acoustic field and the underlying wave propagation of a transducer can be challenging and is mainly defined already in the transducer design.

Particular attention needs to be paid on the sound beam pattern. When transmitting ultrasound, the beam shape will experience deformations as wave propagation progresses. In the so called near field, multiple constructive and destructive interference patterns of ultrasound waves originating from the transducer surface occur which have a converging effect on the beam shape. Starting with beam diameter of the transducer aperture, at one point along the propagation direction, the beam diameter becomes narrowest. This location is commonly referred to as *focus or focal point*. The near field length, however, is a function of the transducers operating frequency as well as its diameter and may be calculated by

$$N = \frac{d^2}{4 \cdot \lambda} \quad or \quad N = \frac{r^2}{\lambda} \tag{1.8}$$

where N is the near field length, d the transducer diameter or r its radius and λ the wavelength (considering the propagation medium). This implicates a longer near field with increasing frequency or larger element diameter. The focal zone, or focus, represents the transition between near field and the so called far field. Waves in the near field are difficult to describe due to their extensive variations in constructive and destructive interference. This zone is oftentimes referred to as *dead zone* as measurements are complicated in this region. Beyond the focus, however, the far field is more consistent as ultrasound intensity behaves according to inverse square law and therefore decays with the square of distance from the transmitting source[20].

Most transducers in medical imaging require a high lateral resolution and are therefore focused. This may be accomplished by either using a piezoelectric element with a concave shape or so called acoustic lenses that are placed in front of the transducers surface. Compared to unfocused transducers, focusing yields to an increased ultrasound intensity and a narrower beam in the focal zone. This allows to focus the highest acoustic beam intensity on a structure of interest. On the other side, if focusing is accomplished, the ultrasound beam diverges more rapidly in the far field than in case of unfocused transducers.

1.6 Wave Propagation Theory

Propagation of acoustic waves is a complex process that needs to be well understood to describe interactions of ultrasound with tissue. The physics behind it consider factors such as frequency, acoustic pressure or the medium a wave travels through.

In general acoustic wave propagation theory a mechanical perturbation introduced at one or several points in medium causes particles to oscillate around their equilibrium position thus generating disturbance in pressure. Energy is thereby passed on from one particle to the other. This dynamic process, i.e. wave propagation, causes areas of high pressure and particle density which are commonly referred to as zones of *compression*. On the contrary, in the so called *rarefaction* areas, pressure and density are low because particles are further apart. This implicates fluctuations in local total pressure and density in the medium as acoustic waves propagates through. The acoustic pressure (sound pressure) p_a is then defined as the pressure variation about the ambient pressure p_0. The total pressure p equals

$$p = p_0 + p_a \tag{1.9}$$

Within an acoustic cycle, sound pressure varies over time in a sinusoidal pattern: during compression it reaches a maximum (i.e. peak positive pressure) and during rarefaction a minimum (i.e. peak negative pressure or peak rarefactional pressure). In medical ultrasound, particular attention is paid to the peak negative pressure as this is an important safety parameter[12].

For acoustic waves through air and liquids, wave motion is longitudinal as the direction of particle displacement vector and wave propagation are the same. In elastic solids transverse (or shear) waves may occur, where due to the shear modulus of the material, particle displacement happens perpendicular to the direction of wave propagation. Displacements induced by shear waves are in general rather small and experience high attenuation by tissue. In addition, shear waves travel slower than longitudinal waves. However, some innovative techniques, e.g. elastography, detect shear waves in order to quantify the elastic modulus of a biological tissue, thus being able to discern healthy from pathologic tissue [3].

1.6.1 Linear and Nonlinear Wave Propagation

Both, linear and nonlinear acoustics are very complex physical branches. Describing interactions of ultrasound with biological tissue, however, requires an understanding of the fundamental processes. When talking about wave propagation, linear acoustic theory applies in almost any case, even if nonlinear effects occur. In a highly attenuative fluid, for example, nonlinear wave propagation may cause higher frequencies (i.e. harmonics) in addition to the fundamental frequency. However, these harmonics will be weak components that are well absorbed by the propagation medium. Ultimately, only the initial linear component will be left and wave propagation may be sufficiently described by the classic linear wave equation

$$\frac{1}{{c_0}^2} \cdot \frac{\partial^2 p_\mathrm{a}}{\partial t^2} - \nabla^2 p_\mathrm{a} = 0 \tag{1.10}$$

where c_0 is the compressional wave propagation velocity, or in other words, the speed of sound. In linear acoustics, an acoustic wave travels through medium at a constant speed. Furthermore, it assumes a low wave amplitude, which causes the pressure-density relation to be linear[12]. As mentioned, under certain conditions nonlinear wave propagation is significant in presence and a linear approach is not applicable anymore. Whether nonlinearities occur while the acoustic wave is traveling depends on a variety of parameters. The Newton-Laplace Equation demonstrates that most of these parameters are related.

$$c = \sqrt{\frac{\gamma \cdot p}{\rho}} \tag{1.11}$$

The speed of sound in an ideal gas depends only on the temperature, whereas when looking at realistic scenarios, especially if liquids or solids are involved, a process may become rather complex. Common physical relationships between density, pressure and temperature, like the fact that pressure is proportional to density and that density decreases with an increase of temperature, help to understand how these parameters influence another. Equation 1.11 shows that the speed of sound c increases in materials with higher elasticity (i.e. higher stiffness), e.g. human bone structures, and decreases in easily deformable materials, such as soft tissue. Note, that Laplace added the heat term γ in order to refer to the adiabatic character of the acoustic cycle. The product $\gamma \cdot p$ is the bulk modulus that mainly indicates the stiffness of a material.

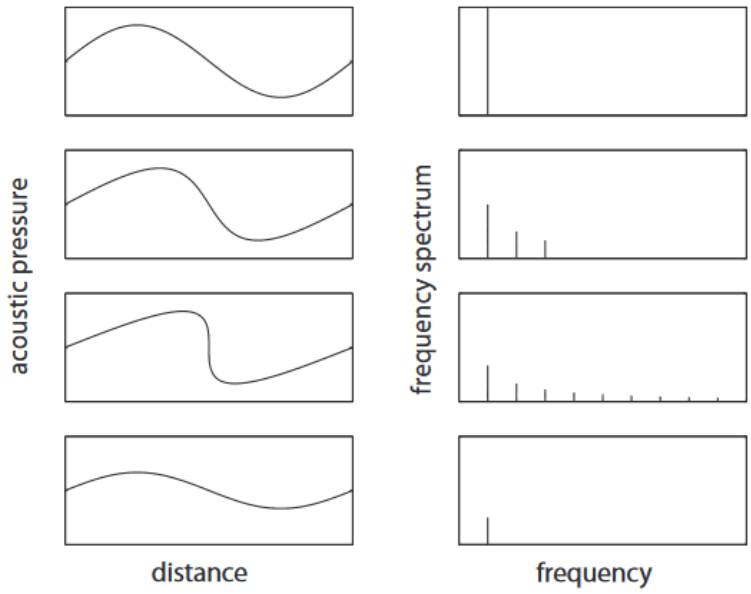

Figure 1.5: Waveform Steeping

Due to the nonlinear pressure-density relation and with help of the Newton-Laplace equation, nonlinear wave propagation can be explained. At low acoustic pressure, a plane wave propagates through a medium without causing distortion (i.e. linear wave propagation). Compression and expansion are oscillating around the mean static pressure. At higher acoustic pressure, asymmetries will appear: the medium will experience an increase in density during the compression and a decrease in density during the rarefactional phase. According to 1.11, this implicates that the wave travels faster during compression and slower during rarefaction. As a consequence, the initially sinusoidal wave distorts as the regions of high pressure are convected in propagation direction. This ultimately results in the appearance of nonlinearities, i.e. the introduction of harmonic components.

The effect of waveform steeping (Figure 1.5) is cumulative, which means energy transfer to higher harmonics increases along the wave propagation direction. Harmonic evolution can therefore be expressed as a function of distance x. According to Wallace et al. [38], the following equation allows, for example, to calculate the amplitude P_2 of the second harmonic frequency:

$$p_2(x) = \frac{1}{2}\beta\omega x \frac{{p_0}^2}{\rho_0 {c^3}_0} \tag{1.12}$$

where β = 1 + $\frac{B}{2A}$ is the coefficient of nonlinearity, intrinsic to the host medium, ω the angular frequency of the fundamental, p_0 is the initial pressure of the fundamental frequency component of the wave, ρ_0 is the density of the propagation medium, and c_0 is the small-signal sound speed in that medium.[38]

Attention should be paid to the nonlinear coefficient β, that represents a measure of acoustic nonlinearity of the medium. It implicates that nonlinear wave propagation depends not only on

acoustic parameters, such as pressure, but also on material properties.

As mentioned, when the wave continues to travel it develops a vertical tangent. The time waveform will at some point along the propagation direction, i.e. the *shock formation distance*, eventually develop an acoustic shock front. The shock formation distance l_d, where the waveform attains for the first time an infinite slope, may be calculated by

$$l_{\mathrm{d}} = (\frac{\rho c^2}{2\pi})\frac{1}{p_0 f \beta} \tag{1.13}$$

Equation 1.13 demonstrates that the generation of nonlinearities depends on a variety of factors. It can be seen, for example, that a higher nonlinear coefficient β results in earlier discontinuities, and so does an increase in frequency. Theoretically, at the shock formation distance l_d the high pressure wave should overtake the low pressure wave. However, realistically this will not happen as due to the frequency dependency of the absorption coefficient, generated harmonics will be attenuated rapidly, thus sort of stabilizing the shock[16].

1.6.2 Cavitation

Cavitation describes the oscillation of tiny gas bubbles (i.e. cavitation nuclei) in a liquid due to the applied acoustic field. According to sinusoidal acoustic pressure changes (i.e. between peak positive and peak negative pressure), a gas bubble will sequentially be compressed and expanded, thus decreasing or increasing in its radius. A good approximation for this spherical process is the *Rayleigh-Plesset equation* [18], which is used to calculate changes in bubble radius over time considering pressure conditions, densities, initial radius, liquid properties as well as surface tension of the bubble. However, the process of bubble oscillation is nonlinear as described by Lauterborn and Mettin [22] due to the fact, that a bubble may be expanded to an arbitrary extent. Compression on the contrary is limited to a value near zero. At low wave amplitudes, bubble oscillation around its equilibrium radius is negligible small (i.e. stable cavitation). Increasing the acoustic pressure leads to stronger nonlinearities, thereby enlarging the bubble due to the asymmetries of peak positive to peak negative pressure. During the rarefactional phase of an acoustic cycle, a bubble grows in size due to diffusion of gas into it, whereas during compression, less gas exits the bubble due to the thicker bubble skin, but smaller diffusion area [5]. At a specific cavitation threshold the bubble is expanded to such an extent that it is unable to withstand the compressional pressure from the surrounding liquid and collapses rapidly (i.e. intertial cavitation) [18]. Acoustic cavitation requires attention and has to be recognized in order to guarantee the safety of an application.

1.6.3 Harmonics

Following the principle of nonlinear wave propagation explained in the previous section 1.6.1, ultrasound propagating through tissue will cause generation of tissue harmonics. The presence of such frequency components is exploited in diagnostic ultrasound such as *tissue harmonic imaging(THI)* with the main benefit of an increased signal-to-noise ratio(SNR) by minimizing artifacts due to the prominent fundamental frequency[36][23]. Some body regions, however, are limited with regard to being examined with ultrasound. This includes the human

brain which is essentially protected by the skull bone. Techniques like transcranial Doppler Sonography to quantify blood perfusion of the brain show in this case low diagnostic value unless additional contrast enhancing methods are used. One promising approach is application of microbubbles[28]. Many of these ultrasound contrast agents are commercially available, primarily approved for cardiac function assessments using ultrasound imaging, but also for non-cardiac applications such as liver tumor imaging. Due to their size similar to blood cells (<10 μm), microbubbles do not penetrate the interior surface of blood vessels (endothelium) and are equally distributed in the entire vascular system within a few heart beats [10] after injection. Once in the human body, they circulate freely following the arterial-venous circulatory system. To increase their lifetime, microbubbles are encapsulated with a shell made of a low solubility, high molecular weight gas such as a perfluorcarbon[28]. Their shells are finally metabolized in the liver and their gas is exhaled through the lungs.

In comparison to other contrast agents, microbubbles differ in a way that they may change their physical properties upon ultrasound exposure, whereas their behavior depends on various factors, such as the acoustic pressure and frequency they are excited with[10]. Due to the high acoustic impedance between the surrounding fluid (e.g. blood) and gas inside, microbubbles are efficient nonlinear scatterers, significantly improving the signal-to-noise ratio of an acoustic response. However, at higher acoustic pressures, microbubbles behave similar to cavitation nuclei in stable cavitation: during contraction of oscillation, bubbles grow rapidly, whereas in the compressional phase, they minimum radius is limited due to stiffing of the gas inside the bubble. These asymmetric-nonlinear oscillation result in the appearance of harmonics. Further increase in acoustic pressure will at some point lead to microbubble destruction[28].

Due to presence of nonlinearities caused by microbubbles at already lower acoustic pressure, a clear separation between microbubbles responses and tissue harmonics is possible[11][4]. Almost any of the available microbubbles are used in imaging modalities, thus being resonant at frequencies higher than 1 MHz. It is therefore understandable, that research mainly focuses on microbubble responses to higher frequencies, whereas their behavior at lower frequencies remains poorly understood.

1.7 Signal Analysis

In practice, a poor SNR makes it difficult to extract and analyze acoustic responses from a received signal. Ultimately, the success depends on the instrumentation, such as transducer sensitivity, but furthermore on the applied post-processing and signal analysis. Today, a variety of tools, e.g. the Fast-Fourier transform(FFT) or matched filters are available for the purpose of signal analysis.

1.7.1 Pulse Inversion

The technique of pulse inversion is commonly used in tissue harmonic imaging [23][33], where harmonic responses originating from human tissue provide diagnostic information. This specific pulsing scheme, in general, improves SNR as it suppresses the fundamental frequency content and odd harmonics, but at the same time pronounces the even harmonic content of an acous-

tic response. Pulse inversion respresents a a promising approach to differentiate microbubble response and tissue harmonics[4].

1.7.2 Matched Filter

Extracting signals out of noisy environment requires innovative techniques. The method of matched filters, is particularly present in todays world of telecommunications, but may be applied to other fields of science, such as acoustics, too. A Matched Filter is the operation which provides the maximum SNR prior to detection. Essentially, it isolates a signal of interest assuming it is in the presence of White Noise. It reduces the noise variance, but preserves the signal energy. The working principle requires a detection threshold, which is derived from a simple hypothesis test. The so called *Nyman-Pearson threshold* is thereby optimal given a Probability of *False Alarm (P_{fa})* and is calculated with an *estimated noise variance* ${\delta_0}^2$ after matched filtering

$$\gamma = {\delta_0}^2 Q^{-1}(P_{\mathrm{fa}}) \tag{1.14}$$

where Q expresses the right-tail probability for *normal (Gaussian) random variables* [40].

CHAPTER 2

Methodology

2.1 Research Objects

This section describes all objects that were used to examine the activity of microbubbles and their interaction with biological tissue.

2.1.1 Microbubbles

For research activities, two agents have been used: *SonoVue* and *BR38*. Both agents are manufactured by Bracco (Bracco Suisse S.A, Geneva, Switzerland). Due to the fact that research with SonoVue and BR38 is usually done at higher frequencies the behavior of the microbubbles at the low transmit frequency as used in this project (i.e. 220 kHz) is not very well explored yet. Both agents are lipid-coated microbubbles. SonoVue containing sulphur hexaflouride gas, which dissolves in the blood and is subsequently exhaled. The bubbles have a mean diameter of 2.5 μm and are therefore larger than Br38 with a mean diameter of 1.4 μm. All agents are stored in a non reconstituted, lyophilized powder form, which in most cases gives them a 2 years shelf life, which decreases down to a couple of days upon reconstitution. Microbubbles were reconstituted with 5 mL of sterile saline (0.9% sodium chloride) in a vial injected through the rubber stopper of the vial. Afterwards the vial is manually agitated for 10 seconds. For any flow study that required an injection of the microbubbles into a water beaker, the bubbles and water were mixed for approximately 2 minutes to assure an equally dispersed medium.

2.1.2 Human Cadaver Skulls

Any of 40 ex-vivo human calvaria and five ex-vivo entire human skulls were used to examine the effect of the intervening bone structure on the acoustic parameters. Physical properties, such as skull thickness or density were collected over time within the scope of a previous project and supported our research activities [37]. In general, all specimens were stored in a dry state and immersed into degassed water over a couple of days prior to experiments. This rehydration was

necessary to eliminate any air trapped in the bony structures. There was no additional tissue fixation other than the initial embalming of the donated body part. Eventually, any specimen had a mounting fixture connected to it for the purpose of positioning.

2.1.3 Rabbits for Safety Studies

36 rabbits were provided by the Cedars-Sinai Medical Center's Department of Neurology and Neurosurgery for the purpose of safety studies. Rabbits were anesthesized with isoflurane for 30 minutes, followed by 60 minutes recovery phase. The reason to do so was to account for potential effects due to the isoflurane. After 60 minutes the animals were anesthesized again with isoflurane for the time period of the ultrasound and microbubble application (SonoVue), which was about 40 minutes total. After the procedure that used ultrasound in combination with microbubbles the animals were allowed to recover and monitored for the following 48 hours. Ultimately, they were euthanized for brain histology.

2.1.4 Acrylic Chamber

With the goal to provide a standardized, reproducible, and reliable experimental set up we decided to design and develop an acrylic box shown in Figure 2.1. This customized pressure box has diameters of 100 mm (width) x 150 mm (height) x 200 mm (length). It has a lid which can be sealed and currently one inlet which carries a pressure valve. This allows measurements that require a pressurized target volume. Towards the bottom of the box there are various inlets and outlets which can be used, for example, to introduce pressure sensors, *polyethylene(PE)* test tubes or to apply flow, if wanted.

2.1.5 Postmortem Tissue

Human cadaver heads provided by the University of California, San Diego(UCSD), Division of Anatomy, were used to investigate signals received from biological tissue. Experiments were done up to 48 hours after death. Information on the cadavers comprised age and gender, but not the cause of death.

2.2 Research Instruments

2.2.1 Transducer

The current inventory comprises five generations of transducers, whereas within a single generation, except the third, there is more than one transducer. The labeling of transducers by the manufacturer neglects a discern between generations. Hence, we agreed upon a customized nomenclature within the research facilities. A transducer is either abbreviated with "X" or "Xdr" followed by the generation index (i.e. 1 to 5) and its index within this generation (i.e. 1 to total number of transducers within a generation). "X52" or "Xdr5.2" defines for example the 2nd transducer of the last generation (i.e. 5th).

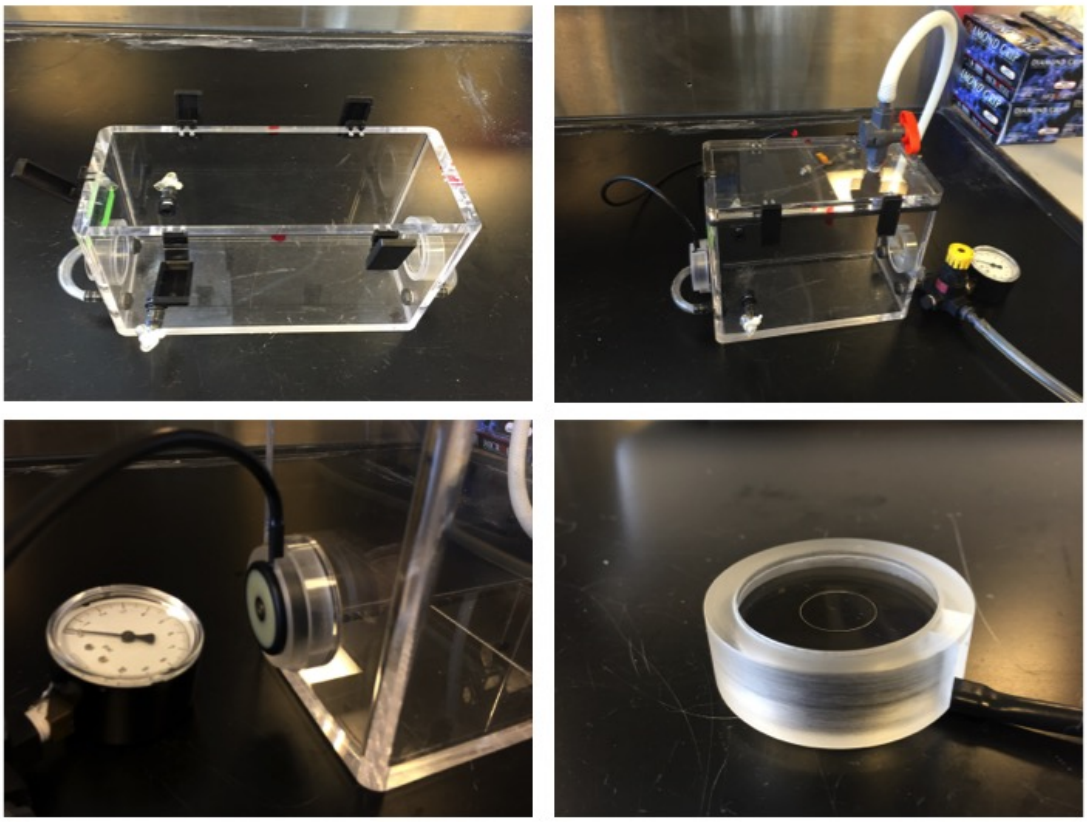

Figure 2.1: Acrylic Pressure Chamber

Throughout the underlying research activities, the basic concept of a dual-element transducer (see Figure 2.2) was maintained. Any of the transducers customized for our purpose by the company Sonic Concepts, Inc. consists out of a center disk and an outer ring assembled in one casing. The center element is a PCD (Passive Cavitation Detector) surrounded by a transmitting ring. Due to the acoustic properties of the examined biological tissue, the transmit efficiency as well as the PCD are of great importance. Hence, transducer development was a constant companion during the entire research project. In general, very little about the manufacturing process (e.g. materials used) is known due to nondisclosure by the manufacturer.

2.2.1.a Transmitter

As mentioned previously all transducers are built to transmit at a frequency of 220 kHz. The outer-ring, a flat active area, is unfocused and has its natural focus at about 3 to 5 cm depending on the transducer. For any transmitter a *1-3 piezo composite* was used. The pillar dicing depth was increased from generation to generation and finally reached a maximum of 95% in the fourth and fifth generation. This significantly improved transducer efficiency due to lower tendency to emission of radial modes.

Figure 2.2: Dual-Element Transducer

Impedance Matching Impedance of the transmit element is an important parameter which contributes to the transmitter efficiency of the transducer. In order to optimize the power transfer from the driving source (e.g. 50 Ω signal generator) to the load (i.e. the transmitter element) an impedance matching circuit was designed for each transducer. In general, the maximum power-transfer from a source to a load is achieved if the load is properly matched to the source impedance. Unlike for DC sources where the source resistance needs to be equal the load resistance, matching the source to a reactive load, such as the transducer, is not as trivial. In general, there are two common methods for impedance matching which are the use of transformers or matching networks. In our case, matching is accomplished by a transformer, where the load impedance is transformed as a square of the voltage- transformation ratio. Due to the actual step-up character of the transformer, the voltage from the signal generator is transformed according to the ratio N which is the number of turns on the input winding divided by the number of turns on the output winding. Note, if not indicated differently, that any voltage value mentioned within this dissertation, defines the *voltage peak-to-peak (V_{PP})* at a specific transducer after the transformer rather than the output voltage of the source, i.e. the signal generator. With the aim to determine this actual driving voltage, we immersed each transducer into a water filled chamber and split the output signal of the impedance matching circuit with a BNC T-connector. One signal line terminated in the transducer, the other into a digital oscilloscope (DSO5012A from Agilent Technologies, CO, USA). Table 2.1 indicates the input voltage and the output voltage of the impedance matching circuit. It furthermore indicates the transformer voltage ratio.

Table 2.1: Impedance Matching Circuit Transformation

Transducer	Input Voltage	Output Voltage	Transformer Ratio	**Mean Transformer Ratio**
	0.01	0.073	7.25	
X41	0.05	0.359	7.18	
	0.1	0.706	7.06	
	0.5	3.58	7.16	
				7.16
	0.01	0.075	7.5	
X42	0.05	0.367	7.345	
	0.1	0.726	7.263	
	0.5	3.660	7.32	
				7.36
	0.01	0.0713	7.125	
X51	0.05	0.348	6.963	
	0.1	0.693	6.925	
	0.5	3.487	6.974	
				7.00
	0.011	0.0784	7.447	
X52	0.051	0.4	7.901	
	0.102	0.783	7.709	
	0.5	3.910	7.82	
				7.72

2.2.1.b Receiver

Detecting the oftentimes weak acoustic response of microbubbles or other structures of interest can be difficult. Hence, having a PCD element of high sensitivity is very important for our research. In the introduction, some materials of PCD elements are described and compared to each other. The material used for the first four transducer generations was PVDF. Narrowing the bandwidth of frequencies of interest down to 660 kHz (i.e. 660 kHz to 1320 kHz), made it possible to change from a broadband PVDF to a tuned PZT element, thus significantly improving the sensitivity of the receiver in the fifth transducer generation. This implicated a 35 dB signal suppression at 220 kHz relative to the passband from 660 kHz to 1320 kHz which furthermore contributed to a better performance. The elements are dimensioned to overlap the transmit focal region, i.e. 25 to 65 mm axially. In any generation, unlike the transmit element, a bulk structure

Figure 2.3: Impedance Matching Circuit for Transducer 5.1, Input right, Output left. Power plug for Mini Fan from Top

was used for the PCD elements.

2.2.2 Analog Filters

Quite a lot of effort has been put into analog filter design, especially if the use of a filter improves the ability to detect microbubble related acoustic events at low excitation voltages. Although the PCD element of the latest transducer version has in comparison to previous generations a limited 6 dB bandwidth, i.e. +/- 25%, with the center frequency at 1 MHz, the prominent character but low information content of the fundamental at 220 kHz remained a concern. This gave rise to eliminate the fundamental component prior to digitizing by using a filter in the analog domain. Throughout the project various filters were applied and their design was constantly improved along the research activities. All of them were customized by the company Frequency Devices (Ottawa, IL, USA). Initially, as the frequencies of interests were not clearly defined, it was preferable designing filters to suppress the fundamental frequency only. Eventually, a 2 MHz anti- aliasing low pass filter was added to this 220 kHz Notch filter. As explained above, recent research revealed a specific bandwidth of frequencies of interest, which simplified the filter design to a bandpass filter. In order to achieve the maximum voltage transfer between the receiver and the data acquisition module any filter was customized to match the PCD impedance of a specific transducer generation.

Notch and Low Pass Filter Combination This filter was tailored to the fourth transducer generation. It is a 220 kHz five pole passive notch filter in front of a 2 MHz five pole low pass filter. It has 6500 Ω input and output impedances and a female SMA input connector and a male SMA output connector. The output is internally terminated in 6500 Ω. The insertion loss at 110 kHz and 330 kHz is less than 3 dB and insertion loss at 220 kHz is greater than 50 dB.

Bandpass Filter As along the project a certain passband of frequencies emerged, the Notch and Low Pass Filter combination became obsolete. Despite the natural passband of about 650 kHz to 1300 kHz of the fifth transducer generation bandpass filters were designed for both the fourth and fifth generation. The reason for an additional bandpass filter in the receiving path in case of the fifth generation is the fact that the total suppression is effectively the sum of both accomplished suppressions, i.e. by the PCD element and by the bandpass filter. Hence, the receiving performance is maximized. However, both bandpass filter generations are six pole Butterworth filters with a center frequency of 933 kHz. Both filter versions have a female SMA input connector and a male SMA output connector. Due to the impedance differences of the PCD elements, the two filter generations have different input and output termination impedances. The insertion loss for both filters is greater than 50 dB at 220 kHz and less than 3 dB in the frequency range of interest (Figures 2.5 to 2.8).

Insertion Loss To minimize insertion loss caused by the filter it is important that the impedances of the receiver and the filter are properly matched. As explained in 2.2.1.b the impedances of the PCD element of each transducer are measured over a broad bandwidth in an water environment. These values are forwarded to the filter manufacturer and used to calculate the average impedance value over the frequencies of interest (e.g. 750 Ω from 660 kHz to 1320 kHz for transducer 5.1 and 5.2). Insertion loss is then tested as shown in Figure 2.4. The acquisition of a baseline (i.e. normalize) requires a resistor in series with the source R_{rcv} that represents the PCD element of the specific transducer. For this purpose, we assume testing of transducer 5.2, which has, as mentioned above, a mean impedance of 750 Ω. Considering the 50 Ω nominal output impedance R_{Source} of the source, the setup additionally requires a parallel resistor $R_{sim\ filter}*$ of 800Ω to substitute the internal filter resistor. Proper impedance matching is accomplished if $R_{sim\ filter}*$ has a value that equals the sum of R_{Source} and R_{rcv}. In this example $R_{sim\ filter}* = R_{Source} + R_{sim\ filter}* = 50\,\Omega + 750\,\Omega = 800\,\Omega$. Once the baseline is established, $R_{sim\ filter}*$ is replaced by the analog filter with the internal resistor $R_{sim\ filter}**$. For both measurements the signal generator is controlled to generate a frequency sweep from 0 to 3 MHz of a sinusoidal continuous wave. The output signal is digitized and its amplitude is plotted over frequency. Figure 2.5 to 2.8 show the results of the insertion loss measurements for transducers 4.1 to 5.2.

Front-End Low Pass Filter The main purpose of the low pass filter was to eliminate artificial 660 and 880 kHz components which were thought to be introduced along the signal generation path. It became clear that the occurrence of these frequencies is related to the mechanical and electrical cross-talk explained in 1.5.2. The conclusion was that the use of a front-end low pass filter is not beneficial.

Artificial Harmonics caused by Vertical Range Mismatch Using analog filters to eliminate the fundamental frequency component involves the risk of generating artifical harmonics due to a Vertical Range Mismatch. The signal reduction occurs to such an extent that it causes a mismatch regarding the current Vertical Range adjustment. The signal amplitude is significantly below the 50 % cut-off of the smallest vertical range to be chosen on either one of the available PXI DAQ options (i.e. 8-bit or 14-bit). A Vertical Range to signal amplitude ratio less than 50 %

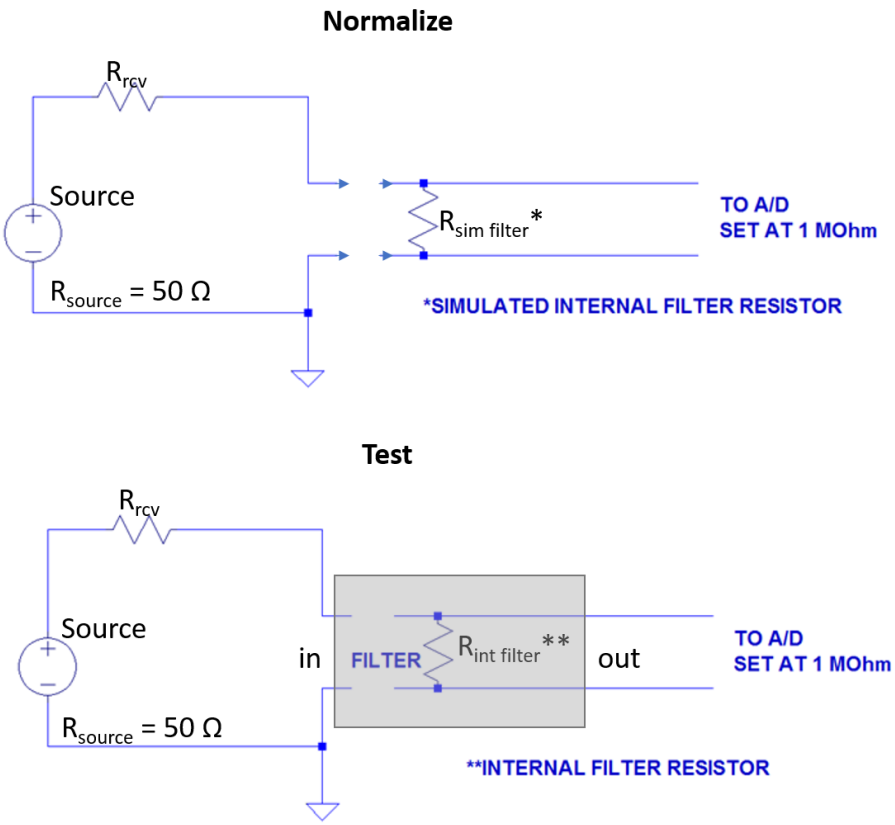

Figure 2.4: Analog Filter Insertion Loss Measurement

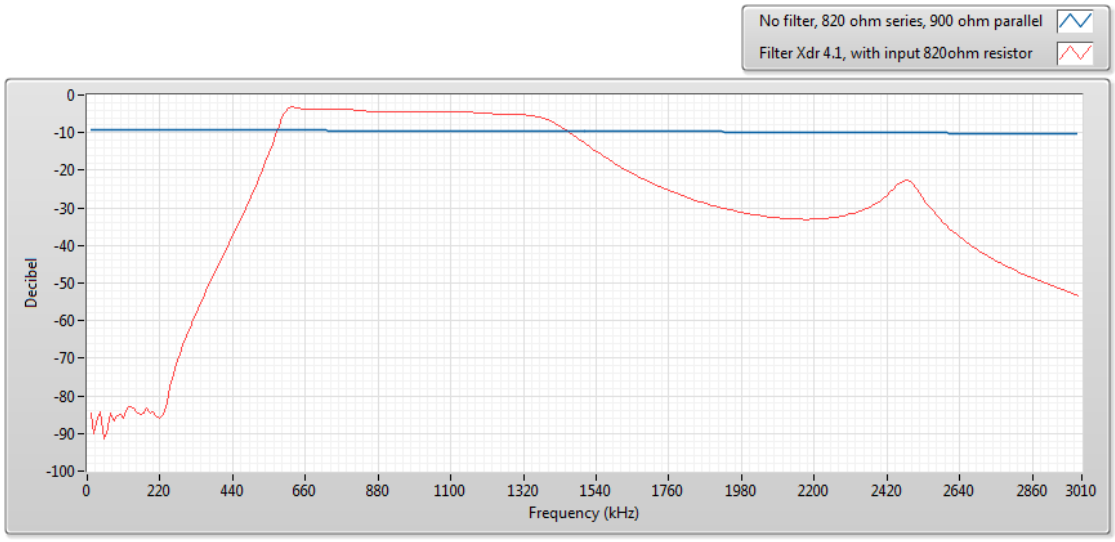

Figure 2.5: Insertion Loss Xdr 4.1

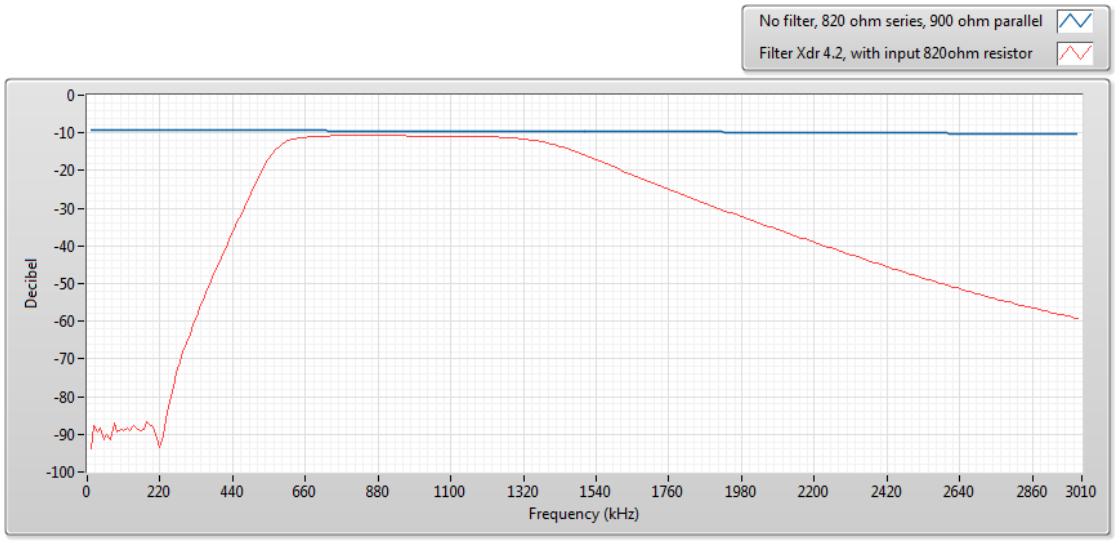

Figure 2.6: Insertion Loss Xdr 4.2

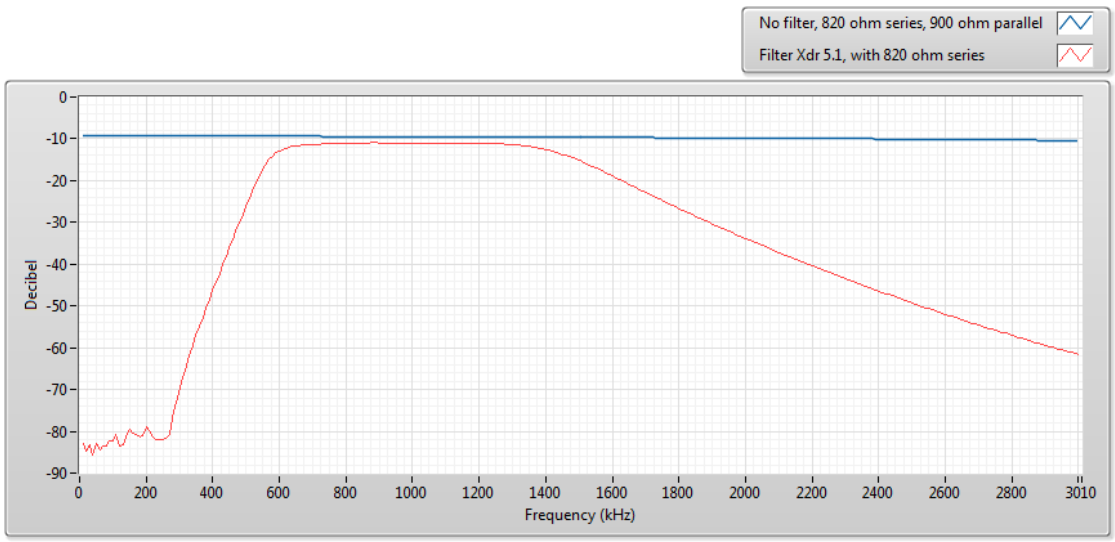

Figure 2.7: Insertion Loss Xdr 5.1

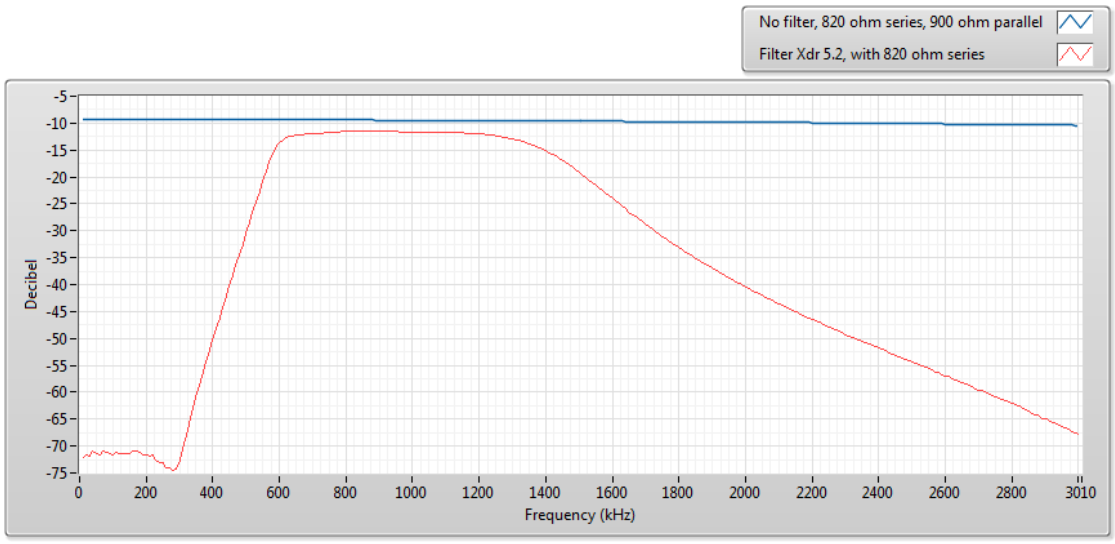

Figure 2.8: Insertion Loss Xdr 5.2

creates the appearance of artificial harmonic components. However, on the contrary to clipping (i.e. if the signal exceeds a current vertical range setting) this was considered to be a negligible small error.

2.2.3 Acoustic Intensity Measurement System

The scanning system AI (Acoustic Intensity Measurement System, ONDA, Inc., USA) is an extremely valuable system to perform acoustic measurements in the 1-, 2-, or 3-dimensional space. Usually, a hydrophone is connected to the motion unit, to determine for example the 3D Pressure Field. The motion unit is part of an automated scanning tank filled with degassed water, also referred to as the wet tank or AIMS tank. The stepper motors are controlled by the software package Soniq (ONDA, Inc., USA), installed on a Windows platform. Especially field characterization requires precise and automated movement of an instrument, such as the hydrophone within the wet tank. AIMS allows to navigate the stepper motors in x-,y-, and z-direction in the millimeter range, thus changing the position of the hydrophone within the tank very accurately. Figure 2.9 shows the general assembly of components.

Water Preparation Due to the negligible small attenuation coefficient of water, all of the reported experiments are done in a pre-conditioned environment. Unlike in-vivo measurements a constant attenuation coefficient can be assumed under controlled water conditions. To assure that the water has a minimal impact on the results, the AIMS tank is cleaned and refilled with fresh deionized water on a weekly basis and degassed prior to any set of measurements with the laboratory water filtration and purification system. Proper degassing is of immanent importance as small dissolved gases may form bubbles, thus attenuating the ultrasound energy. Prior to and after a measurement conductivity, total dissolved solids(TDS), and temperature in the wet tank

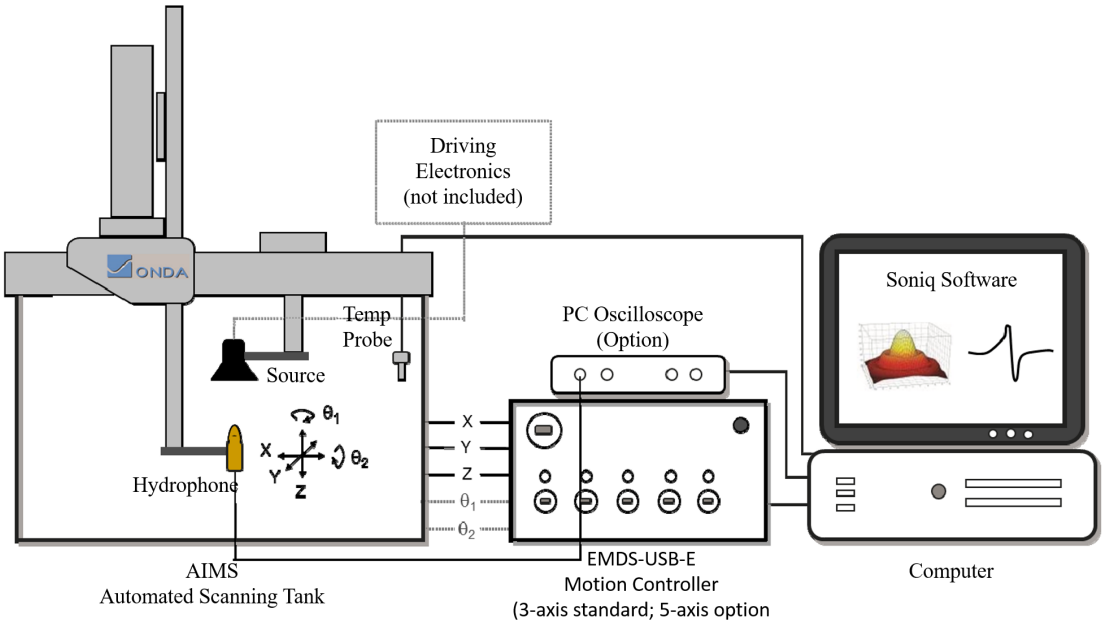

Figure 2.9: AIMS Simple Measurement Overview (www.ondacorp.com)

are measured with a conductivity meter (Oakton Con 11) and a dissolved oxygen meter (Oakton DO6). These values are duly noted in a water quality log along with date, time and relevant comments. There are no specifications for conductivity or TDS, however the readings should not differ much from previous readings. Typical values are less than 3 parts per million dissolved oxygen and dionization to less than 0.05 microsiemens conductivity. The water temperature is between 20°C to 22°C.

2.2.4 Function Generator

Measurements for the purpose of transducer characterization were mainly performed with a bench top function generator (Agilent 3320A, Agilent Technologies, CO, USA).

2.2.5 Oscilloscope

A digital oscilloscope (DSO7012B from Agilent Technologies, CO, USA) captured waveforms (voltage) and connected to the AIMS computer through USB. This 12-bit oscilloscope with a maximum sampling rate of 2 GS/s, was used in combination with the 3320A function generator to characterize transducers.

2.2.6 Listening Devices

Beside the inner PCD element of each transducer, some studies required stand-alone listening devices. For these measurements a hydrophone (Model Y120 from Sonic Concepts Bothell,

WA, USA) was used. The Y120 covers a frequency range from 50 kHz to 1.9 MHz.

2.2.7 PXI platform

Although a PXI platform from National Instruments(NI) is not necessarily dedicated to acoustic measurements it served the purpose for the vast majority of experiments. The easy application of various NI modules, such as arbitrary waveform generators or data acquistion modules(DAQ), provided the required flexibility in our research.

2.2.7.a NI Arbitrary Waveform Generator

For any experiments that involves the NI PXI platform, the NI PXI-5421, an arbitrary waveform generator to generate the transducer driving signal, was used.

2.2.7.b NI Data Acquisition Module

Due to the fact, that the relevance of ADC parameters, such as resolution and sampling rate, was not clearly determined at the beginning, quite a few data acquisition modules were evaluated. Some rather loose requirements for a resolution higher than or equal to 8-bit and a sampling rate greater than or equal to 100 MHz for the sake of anti-aliasing led ultimately to the decision to purchase various kinds of data acquisition modules:

- NI USB-5133: USB- module, 8-bit resolution, maximum sampling rate of 100 MS/s
- NI PXIe-5122: 14-bit resolution, maximum sampling rate of 100 MS/s
- NI PXI-5114: 8-bit resolution, maximum sampling rate of 250 MS/s

However, the LabView algorithm sets the sampling rate and number of samples to acquire. If not indicated differently, the NI-PXIe 5122 was used for any acquisition with the PXI. Commonly, in this work, we referred to the NI Data Acquisition Module as *DAQ* or *Scope*.

2.2.8 Power Amplifier

Low efficiency of the transmission pathway or the poor performance of the PCD elements regarding sensitivity, oftentimes required an additional amplifier stage in the transmission pathway. This was especially the case for the older transducer versions. At first, the basic assumption behind an amplifier was the higher the acoustic pressure, the greater the acoustic response of the tissue or microbubbles would be. Higher acoustic pressure on the other hand requires a higher driving voltage of the transducer. Furthermore, without power amplifier acoustic response analysis at higher driving voltages would not be feasible. All signal generators available in the research facilities are capable of generating around 10 V_{PP} maximum (stand-alone signal generator: 10 V_{PP}; PXI module: 12 V_{PP}). At the beginning of the project for transducers with poor efficiency and the interest in the wrong target frequencies, driving voltages up in the 300 V_{PP} range were desired at the transducer. Taking the impedance matching network as an step-up transformer with a multiplication factor of 6 into account, requires 50 V_{PP} at the input

of the matching circuit. In this case the use of an amplifier was inevitable. Although amplifiers with various gains were used throughout the project, the current inventory comprises two 40 Watts amplifiers 240L from Electronics & Innovation, Ltd.. The amplifiers operate in a frequency range from 10 kHz to 12 MHz. One observation when using the amplifier was that the input signal gets inverted, which was confirmed by the manufacturer. However, this fact may be neglected as it does not influence transducer performance.

Power Requirement Considering 100 V_{PP} as the maximum desired voltage at the matching circuit input, 40 Watts as power specification were determined based on the following calculations:

With

$$V_{\text{rms}} = \frac{V_{\text{PP}}}{2 \cdot \sqrt{2}} = \frac{100\ \text{V}_{\text{PP}}}{2 \cdot \sqrt{2}} = 35.36\ \text{V}_{\text{rms}} \tag{2.1}$$

and an *impedance* of 50 Ω *power P* becomes

$$P = \frac{{V_{\text{rms}}}^2}{R} = \frac{35.36\ \text{V}_{\text{rms}}}{50\ \Omega} = 24.99\ \text{W}. \tag{2.2}$$

The initial concern of driving the amplifiers into saturation was addressed by using 40 Watts amplifiers.

Gain Upon receiving the amplifiers, the gain at 220 kHz using a 100 mV_{PP} continuous wave signal into the amplifier input was measured. The output was measured with the oscilloscope (50 Ω input impedance). Gain was then calculated as the ratio of the output voltage on the oscilloscope to the input voltage from the signal generator. A very first check showed a gain of 330 or 50.37 dB for amplifier 1 (i.e. SN200) and a gain of 315 or 49.97 dB for amplifier 2 (i.e. SN201). According to the manufacturer's specification sheet both 240L amplifiers have a nominal power gain of 50 dB. Therefore, the measured values agree with the values provided in the documentation. However, both instruments, are marked with their gain and tested prior to any measurement set.

Linearity When it comes to linearity the amplifiers output has less relevance than the actual acoustic pressure delivered at a certain point within the field. Hence, the pressure field (i.e. peak negative pressure) was measured in the wet tank if the output of the amplifier increases from 10 V_{PP} to 100 V_{PP} in 10 V_{PP} increments. The pressure field was picked up by the hydrophone Y120 003 placed 30 mm from the transducer. Ideally, a good linearity between the power amplifier and the measured peak negative pressure should be observed. Slightly different gains are not of concern. Both amplifiers were evaluated with this method.

2.2.9 Soniq

The software package Soniq (former AIMS) from ONDA, Inc., USA was included in AIMS and installed on the AIMS computer. It is, as mentioned above, responsible to control the stepper motor. In addition, Soniq may be used to indicate acoustic parameters, such as PNP, or to capture

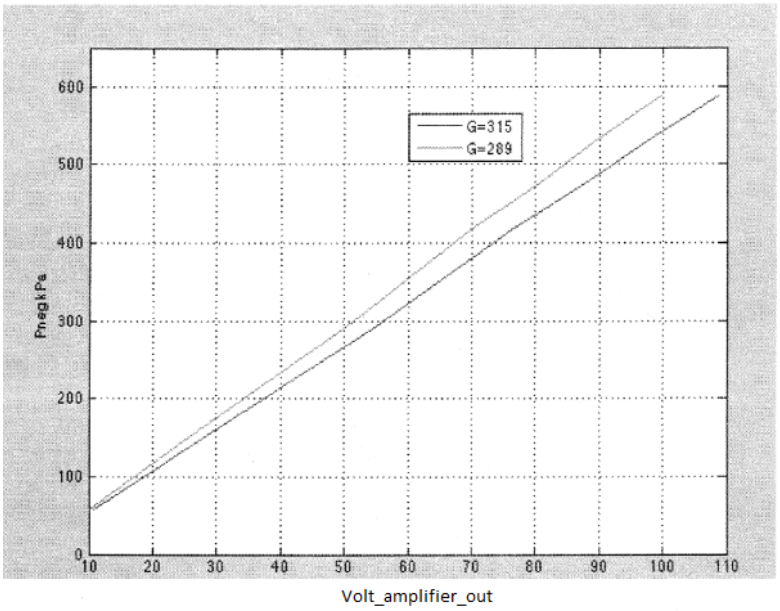

Figure 2.10: Example Power Amplifiers Linearity, Output Voltage/ Peak Negative Pressure

data acquired with the DSO7012B oscilloscope and forward it to MATLAB for further analysis (e.g. for the purpose of transducer characterization).

2.2.10 MATLAB

The software MATLAB (The MathWorks, Inc.) is used in combination with AIMS. Routines initiated and terminated data acquisition, retrieved and stored data captured with AIMS. Furthermore, any data that was acquired with Soniq was post-processed and analyzed offline in MATLAB.

2.2.11 LabVIEW

LabVIEW 2014 was installed on the NI controller of both PXI systems. The *NI-FGEN* and *NI-SCOPE* drivers with already existing *virtual instruments*(VI) provided by National Instruments, were used to control signal generation and data acquisition.

2.3 Research Algorithms

Various algorithms were developed in LabVIEW to control all sort of measurement parameters in real-time, but also to post-process and analyze data offline. Algorithms evolved during the research according to our gained knowledge and were adapted to the purpose of each experiment. Initially, a rather complex algorithm was put together that should facilitate the operation by any member of the research team. This first version was used in experiments that required a high

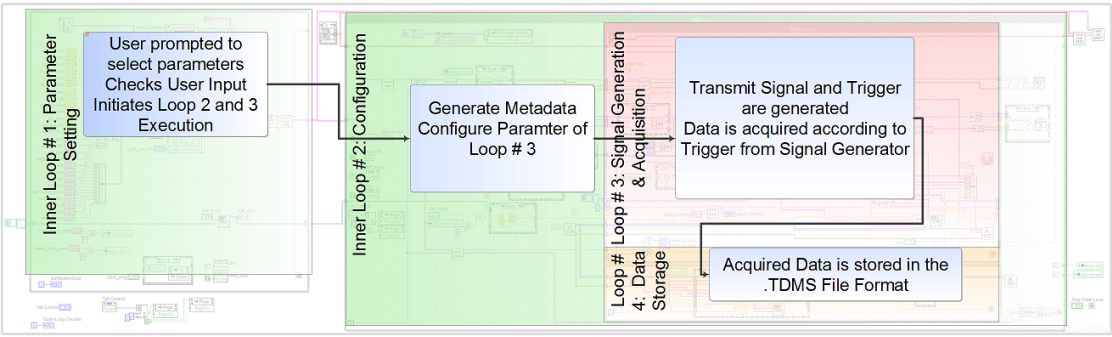

Figure 2.11: LabVIEW Code for Automated Acquisition

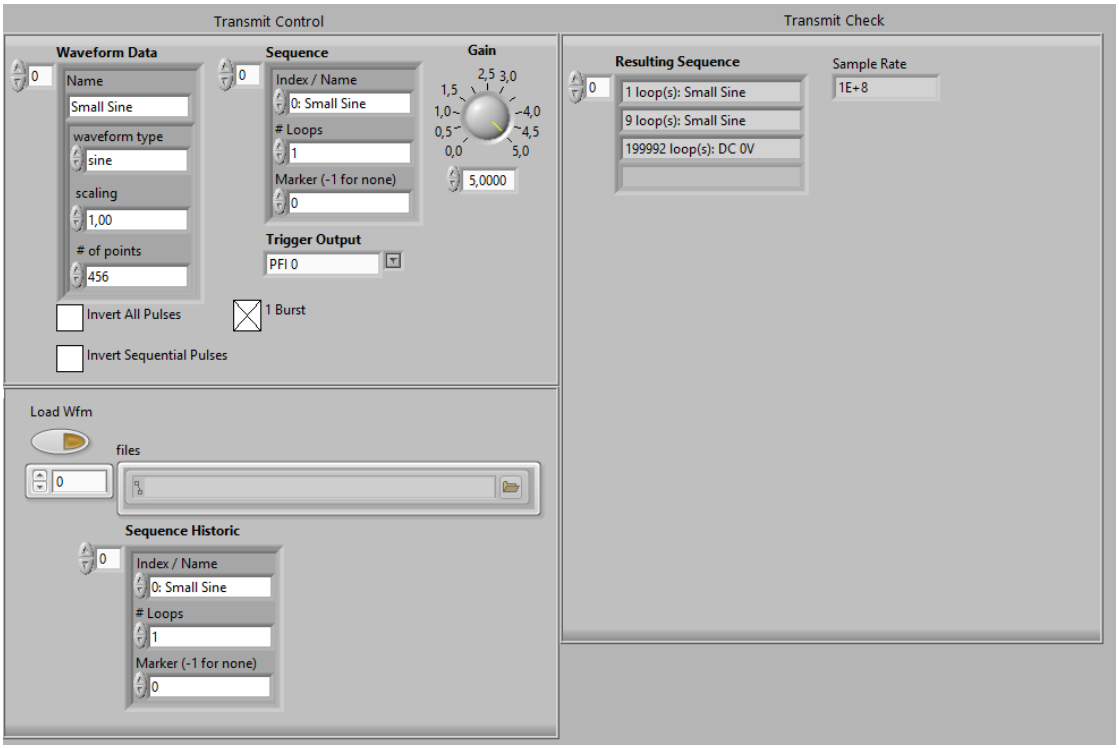

Figure 2.12: LabVIEW Transmission Control

degree of automation, such as in measurements over longer duration (e.g. animal safety studies). A general work flow is provided in the schematic 2.11. The most recent version was trimmed to perform acoustic measurements of smaller quantity, for example, in the customized acrylic chamber or in the human cadaver studies. The front panel for the version is shown in Figure 2.12 and 2.13. Note, that in this case, two VIs were created, one for generating the transmitted signal and another for data acquisition.

Figure 2.13: LabVIEW Acquisition Control

Acquisition Trigger In most cases, the processes of transmitting and receiving, were, from a timing perspective, closely linked together when it comes to acoustic measurements. Accurate timing between these two is a critical factor. Data acquisition was therefore commonly triggered by a transmit event. This means, once a pulse was transmitted, a trigger was sent either through the PXI's backplane or a BNC cable from the trigger output of the arbitrary waveform generator to the trigger input of the data acquisition module.

Data Storage During acquisition a specified amount of samples was written to a *NI Technical Data Management Streaming(TDMS)* file and stored for post processing. TDMS is a file format from NI and facilitates post processing and the application of a database in LabVIEW. A real-time indicator displayed the acquired signal in the time and frequency domain. Depending on the acquired amount, data was stored either as binary or as double-precision numeric data type. Especially, the former LabVIEW versions, required a sophisticated data management. If not properly stored as binary type, datasets could reach the size of Gigabytes, which was highly impracticable for working with the measurement file. Storing binary data required the record of the DAQ gain and offset for reconstruction from binary to voltage values. Hence, a property node in the VI's block diagram read the current gain and offset of the DAQ. The conversion from binary data points to double-precision values (i.e. voltage) looked as follows:

$$\text{Voltage} = \frac{\text{Binary Value} \cdot \text{DAQ Gain}}{\text{DAQ Offset}} \tag{2.3}$$

2.4 Experimental Parameters

The arbitrary waveform generator NI PXI-5421 generated, if not indicated differently, a sinusoidal driving pulse of 220 kHz. Depending on the transducer efficiency, some experiments used the additional power amplifier. Regardless of the power amplifier, the driving signal is forwarded to the impedance matching network before it reaches the transducer. This is where the electric transmit path terminates and the transducer converts electrical energy into acoustic energy. The acoustic wave propagates through the target (e.g. biological tissue) and reflections are picked up by the receiver. Determining the optimal excitation pulse was one of the biggest challenges throughout the project. The right choice depended mainly on the application. Basically any of the following transmit parameters were evaluated for our purpose:

- Waveform
- Frequency (f)
- Amplitude (V_{PP})
- Pulse Repetition Time (s)
- Duty Cycle (%)
- Measurement Time
- Ramp-Up (%)
- Pulse Inversion

2.4.1 Waveform

The standard input waveform to the transducer is sinusoidal. Even if the sinusoidal excitation pulse happens to be not very pure, the transducers are capable of compensating for it considering their bandwidth and physical properties. Initially, a waveform consisted of three parts, which was a ramp-up, the actual pulse of a certain width and an off-time (i.e. zero sequence) to accomplish the defined pulse repetition time. Changes in data analysis led to the decision removing the ramp-up. If the arbitrary waveform generator module from National Instruments is used, waveforms are generated at the maximum sampling rate (i.e 100 MS/s) in order to achieve the best resolution.

2.4.2 Duty Cycle

Given in % the duty cycle is the ratio between the pulse width and pulse repetition time. A pulse width of 10 ms, for example, with a 1 second pulse repetition time yields a 1% duty cycle, whereas 100% is the same as a continuous wave. Due to mathematical relation of duty cycle, pulse width and pulse repetition time, only two parameters need to be specified.

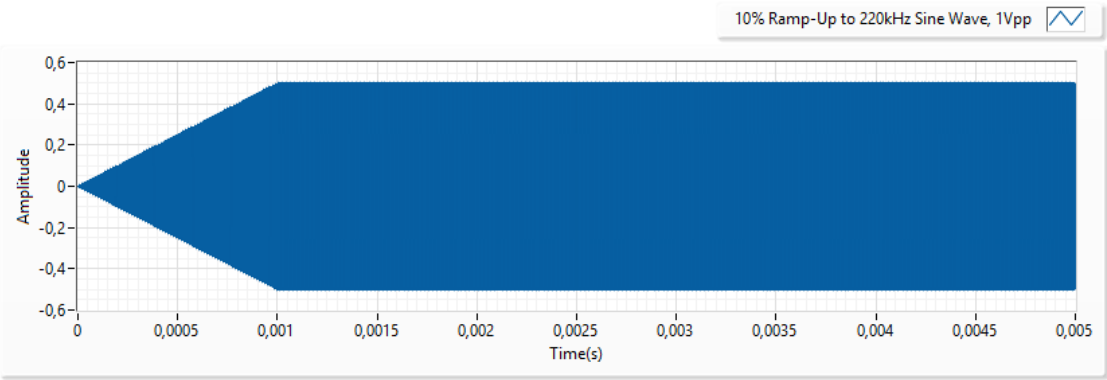

Figure 2.14: Example of 5 ms 220 kHz Driving Pulse with initial 10% Ramp-Up

2.4.3 Measurement Time

This duration is defined by the repetitions of a single waveform. The measurement time results from the multiplication of the total number of pulses and the pulse repetition time.

2.4.4 Ramp-Up

During the ramp-up sequence a specified percentage % of the pulse is shaped as a ramp-up. This part happens at the beginning of the pulse. Values between 0 and 100% are possible, but default are 10%. The signals amplitude increases from 0 V_{PP} to the final amplitude of the pulse (see Figure 2.14).

2.4.5 Pulse Inversion

The feature of pulse inversion (Figure 2.15) in post-processing requires a certain transmission sequence. Therefore, two identical pulses but of opposing polarity are transmitted consecutively. Ultimately, pulse inversion happens in the post-processing where an acquired pair of responses is added in the time domain.

2.4.6 Transmit Configuration

Amongst all parameters, amplitude changes between different measurements are of course most common. Whereas in some experiments, such as transducer characterization, continuous waves were used, initially, 16 combinations of duty cycle and pulse repetition times(PRT) were defined and selectable in the LabVIEW algorithm.

Later on, the settings were changed to the extend of significantly shorter pulse width in the less than 100 microsecond range. In order words, rather than generating thousands of cycles, the number was decreased to either 10 or 20 cycles of 220 kHz. Considering a period P of 4.545 μs, 10 cycles have a 45.4 μs and 20 cycles a 90.90 μs pulse width.

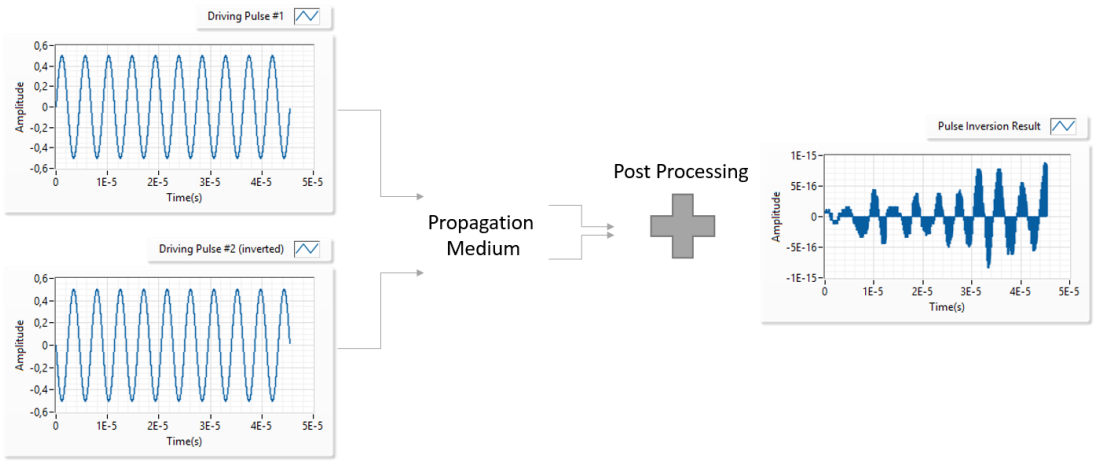

Figure 2.15: Principle of Pulse Inversion

Table 2.2: Data Acquisition Loops

PRT(s)	PW(s)	DC % result
1	0.01	1
1	0.002	0.2
1	0.003	0.3
1	0.005	0.5
0.5	0.01	2
0.5	0.002	0.4
0.5	0.003	0.6
0.5	0.005	1
0.2	0.01	5
0.2	0.002	1
0.2	0.003	1.5
0.2	0.005	2.5
0.1	0.01	10
0.1	0.002	2
0.1	0.003	3
0.1	0.005	5

2.4.7 Acquisition Configuration

On the receiving side, if not indicated differently, the highest sampling rate was used and number of samples to collect were chosen to fulfill the purpose of the experiment.

2.5 Transducer Characterization

Like any other laboratory equipment, upon arrival of a transducer had to undergo standardized test procedures to assure proper functioning. This included a visual inspection and the measurement of the impedance of the transmitting as well as the receiving element. Furthermore, the acoustic behavior of a transducer was measured within the so called free-field measurements. Therefore, 3D scans of the acoustic PNP field were done with AIMS. In addition, characterization required examination of the received time signal in both, the time and frequency domain. Due to the reciprocity of efficiency and sensitivity, in order to perform a check of the sensing element, it may be used as a transmit element. A standard procedure to evaluate the PCD element was initially not in place and ultimately developed for the 5th transducer generation only. How the PCD performance was examined, is described in 2.5.3.

2.5.1 Impedance Measurements

After visual inspection, the impedance of the transducer was measured with the TE3001 One Port Network Analyzer (Trewmac Systems, Australia). Controlled by a software package on a Windows platform, the probe of the analyzer was connected to the transducer under test, which is itself was immersed in the wet tank for proper loading of the transducer element. Although all experiments were performed with the transducer placed in an water environment, the impedance was also measured in the dry state (i.e. transducer in air). The impedance was determined for both elements of each transducer. For the transmit element a frequency range from 100 kHz to 440 kHz in steps of 2 kHz (i.e. 171 points) was used. For the PCD element the frequency range was 100 kHz to 2 MHz in 10 kHz steps (i.e. 191 points). The program then displayed the impedance data at these frequency points either in polar or rectangular form. Figure 2.16 shows the setup how the TE3001 and the computer were used to measure the impedance of transducer 5.2 in the wet tank.

2.5.2 3D Acoustic Field Scans and Efficiency Measurements

In this measurement category, no reflectors located along the wave propagation axis. This is why the type of experimental setup is commonly referred to *free-field measurements*. The overall aim of this method is to determine the 3D Pressure Field for an individual transducer. Measurements were done with all available transducers. A transducer was mounted to a stainless steel rod, which attached to a customized holder to keep the transducer in a fixed position and immersed at about 100 mm below the water surface, oriented along the lengthwise axis of the wet tank. Perpendicular to the transducer aperture, a Y120 hydrophone was mounted to the stepper motor controller and lowered into the wet tank, approximately coaxial with the transducer, with a separation distance of 40 mm. The step motor system from AIMS allowed to position the Y120 at preset coordinates, and to move the hydrophone for a 3D scan of the acoustic pressure field. Figure 2.17a and 2.17b show the general setup.

The transducer was connected to output of an associated impedance matching box, which was in turn connected to the output of the Agilent 3320 signal generator on its input. The output of the signal generator was set to a sine wave frequency of 220 kHz, and an amplitude

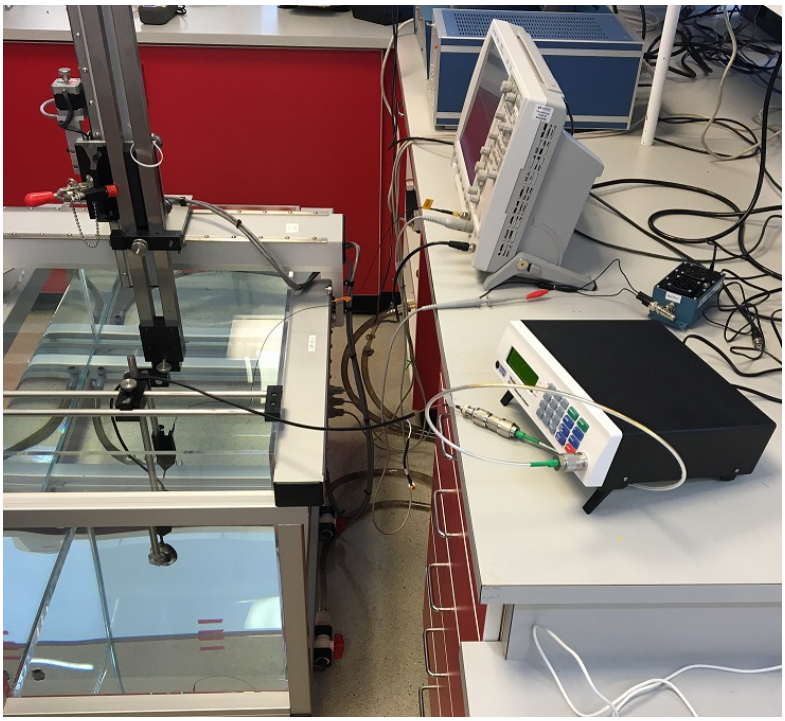

Figure 2.16: Impedance Measurement Setup

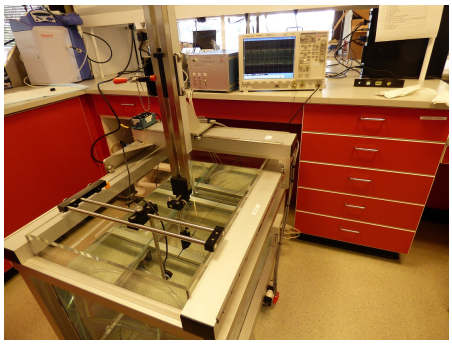

(a) 3D Acoustic Field Scans, Experimental Setup

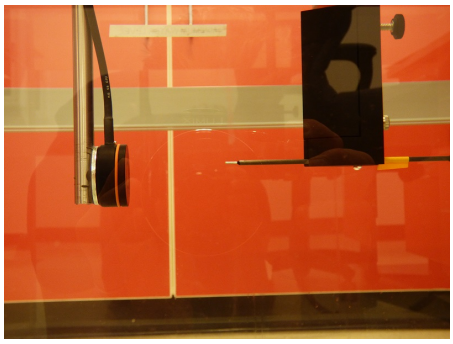

(b) 3D Acoustic Field Scans, Setup of Xdr and Hydrophone

Figure 2.17: Acoustic Field 3D Scan Measurements Setup

of 10 V_{PP}. The hydrophone was connected to the channel 1 input of the AIMS oscilloscope (Agilent DS07012B). Scan dimensions were from -10 mm to +10 mm in the Up/Down (y-axis) and Front/Back (x-axis) directions. The limits of the Left/Right (z-axis) were from 5 mm to 100 mm as measured from the transducer face. 3D data sets were acquired and stored on the AIMS computer and data wass analyzed in MATLAB using customized reconstruction routines.

2.5.3 Sensitivity

At one point during our research it was noted that the receive sensitivity of a disc style transducer varies with distance. In other words, there is a 3D receive sensitivity pattern that is analogous to the 3D transmit pressure wave patterns that we accustomed to viewing. However, in the past the receive sensitivity field has not been measured for our transducers, and it was unclear how to proceed with measurement. Therefore, an objective was formed around measuring and characterizing the receive sensitivity characteristics of a disc transducer. Initially, the measurement of the PCD sensitivity was essentially a two-step process, the first being the measurement of the acoustic field of a specified transmitter using a calibrated hydrophone. For this purpose, a 1Mhz transducer (PA768 from Precision Acoustics) was selected as a transmission source to produce signals at 880, 1100 and 1320 kHz. The transducer was driven with the Agilent signal generator, using a 10 cycle burst, 10 V_{PP} amplitude, and 20 ms burst period. The Y120 hydrophone normally used at 220 kHz was selected to measure the pressure wave of the transducer over distance. The hydrophone sensitivity has calibration values over a range of frequencies but interpolation and extrapolation was necessary to cover certain frequencies, thus introducing some error in the magnitude that would be measured at those frequencies, although the shape obtained would be true nevertheless. The hydrophone was used to measure pressure along the axial centerline of the pressure wave of the emitter, at 10 mm increments from 20 mm to 160 mm. In the second step, transducer 5.2 was inserted on axis in place of the hydrophone, and the voltage from the transducer recorded versus distance along the acoustic centerline. Finally, a calculation of *volts over pascal* was performed in the expectation that this would represent the transducer's sensitivity. The sensitivity curve was compared with a simulated curve, and was found to diverge substantially at longer distances. Also noteworthy along the way, it was found that longer pulse bursts caused harmonics in the tank. It was confirmed that 10 cycle bursts with 10 ms quiet time between bursts provided a repeatable results without significant tank effects.

However, it was suggested that the measurement technique explained above is not really valid because the transducer PCD receiver element is a disc approximately 14 mm diameter, while the hydrophone is a point receiver at the exact centerline. Therefore, the amount of energy striking the face of the PCD is different than the point measurements on the axis. So, another measurement technique was identified where the hydrophone would take many measurements over 2D surfaces representing the 14 mm surface of the PCD, with the average pressure being calculated over the 2D surface. Then, transducer 5.2 voltage measurements were divided by the average pressure values for the 2D surfaces to calculate the sensitivity in units of μV_{PP}/Pa. Again, we were expecting that this would result in a measurement of transducer receiver sensitivity versus distance. During the process of working on these measurements, through external consultations and research, the team confirmed that the receive sensitivity fields of a disc element should be equal and opposite to the transmit pressure fields for the same frequency. Given

this, an alternative of measuring the receive sensitivity fields by driving the receiver element as a transmitter was proposed. The transducer supplier confirmed that the receiver element could be driven in this manner. Since only the shape of the field was critical for this measurement, the lack of a matching impedance circuit for the receive element was ignored. The receive element was driven at our signal frequencies (i.e. 880, 1100 and 1320 kHz), and the needle hydrophone used to measure the 3D pressure fields. These 3D pressure fields were compared to simulated 3D pressure fields for the receiver element acting as a transmitter at the target frequencies. The correlation between simulations and actuals was excellent. During this sequence of measurements, it was also discovered that in order for the actual measurements to converge with simulated data when in the near field of the source transducer, it was necessary to take multiple samples (8 were chosen) averaged over time, at each point of the 2D circular area. When not in the near field, correlation with the simulated data was achieved even without taking multiple measurements at each point. In addition to measuring the output of transducer 5.1 (driving the receiver backwards) with the hydrophone and 2D circular plots, the 5.2 transducer was placed opposite the 5.1 to capture similar measurements that were expected to correlate to the 2D circular averages from the hydrophone. Due to the relatively new establishment of this method, sensitivity for transducer 5.2 was determined only.

2.5.4 Time and Frequency Domain Analysis

As described above, a completed transducer characterization includes analysis of both,time and frequency domain. For this purpose, the transducer was removed from the AIMS wet tank and immersed into a customized acrylic chamber which will be described later on. In this experimental setup the PXI waveform generator drove the transducer with 10 cycles of 220 kHz sinusoidal pulse (i.e. 45.45 μs) at 10 V_{PP} and the NI PXIe-5122 was used to acquire data. Both, transmission and acquisition were initiated simultaneously in LabVIEW. Analysis in LabVIEW allowed to determine the transducer specific ring-up and ring-down phase. Due to the fact, that transmission and acquisition were active simultaneously, the experiment indicated the extent of electrical and mechanical cross-talk. It further served as a functionality assessment of the transducer. In time domain, for each transducer ring-up, ring-down and cross-talk were specified. The time window for frequency analysis was calculated by visually subtracting the number of transmitted cycles (i.e. usually 10 or 20) from the point where ring-down ended. The frequency analysis was important to characterize the transducer with regard to its individual frequency components.

2.6 Mechanical Index, Thermal Index Cranial and Intensity

From a regulatory standpoint *MI*, *thermal index cranial(TIC)* and I_{spta} are critical parameters that need to be calculated for an ultrasound application for risk assessment purposes. Based on the equations provided in the introduction, these three parameters were calculated from measured peak negative pressures and instantaneous acoustic power. *TIC* and I_{spta} were calculated assuming a 0.5% duty cycle. Acoustic pressures were determined using the same experimental setup as for 3D acoustic scans with AIMS. The bench top function generator in combination with the power amplifier generated signals from 10 to 100 V_{PP} in 10 V_{PP} increments at the input

of the impedance matching network. Due to essentially the same efficiencies of transducer 4.1, 4.2, 5.1 and 5.2, results are only shown for transducer 4.1.

2.7 Transcranial Field Assessments

In general the experimental setup is similar to free-field measurements described in 2.5.2. The main difference is the introduction of bone, which is essentially the most critical biological structure within this research. Like in the previous section, the 3D Pressure Field was measured with the hydrophone controlled by AIMS. The experiments were done for an individual transducer with a human half skull for varying positions. Like in the previous section, assessments were done with all available transducers.

Positioning of the Skull The human half skull was positioned with its exterior temporal bone surface 5 mm from the transducer face (Figure 2.18, 2.19 and 2.20) at the following three different positions:

1. Lateral-Posterior
2. Lateral-Superior
3. Lateral-Anterior

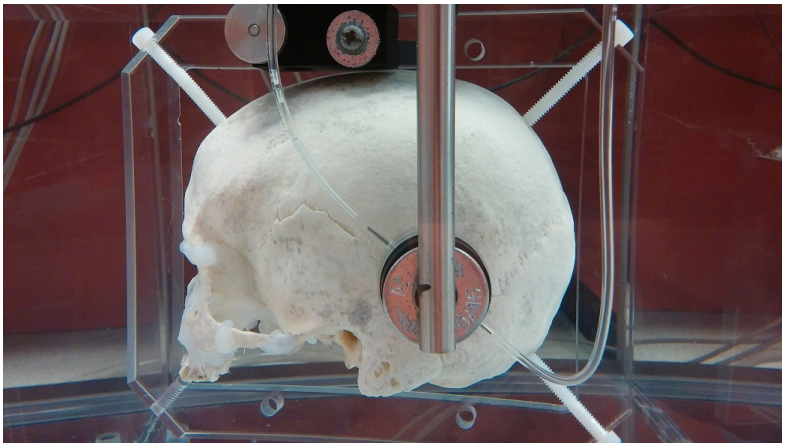

Figure 2.18: Lateral-Posterior (Position 1)

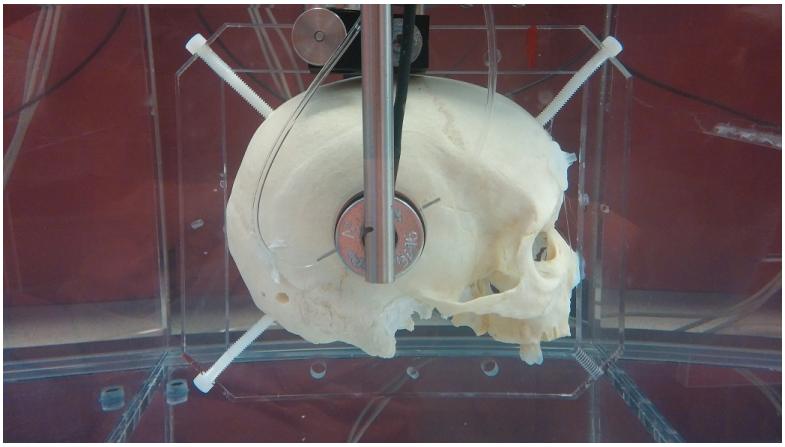

Figure 2.19: Lateral-Superior (Position 2)

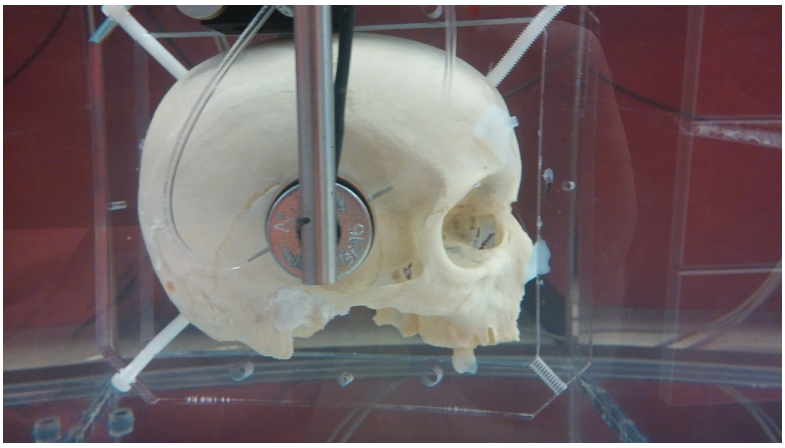

Figure 2.20: Lateral-Anterior (Position 3)

Scan Dimensions For each scan condition, the measurement spacing was 1 mm. The hydrophone was moved within scan dimensions from -10 mmto +10 mm in the Up/Down (y-axis) and Front/Back (x-axis) directions. The limits of the Left/Right (z-axis) were from 20 mm to 100 mm as measured from the transducer face.

Data Storage, Preparation and PNP Loss Calculation A MATLAB routine stored the data and reconstructed the acoustic volume in a post-processing step. The volumetric shape was then compared to the free-field measurements in order to determine the influence of the intervening skull. For the purpose of PNP loss calculation, an algorithm identified the maximum PNP in the X/Y plane at a distance of 40 mm away from the transducer face (i.e. *Sk PNP Z40*). By comparing this value to the maximum of the free-field measurements in the same plane (i.e *FF PNP Z40*) with Equation 2.4,

$$\text{PNP Loss } \% = 100 \cdot (1 - \frac{\text{Sk PNP Z40}}{\text{FF PNP Z40}}) \tag{2.4}$$

the *PNP* loss in percentage was calculated. Note, that the distance of 40 mm away from the transducer was chosen to accomplish a reasonable comparison method.

2.8 In-Vitro Acoustic Response Studies

Not only the detection of microbubbles, but more so the characterization of acoustic responses caused by the gaseous bodies, were the main objectives. Furthermore, the separation of acoustic responses and their allocation to distinct tissue, was one of the major research questions. In-vitro studies were done in either the AIMS tank or the customized acrylic box, with or without microbubbles and with or without biological structures along the acoustic propagation direction. This includes the mimicking of a flow system, in form of a PE tube, or a perfused volume, as for example, simulated in the acrylic box. Furthermore, the human ex-vivo cadaver skulls were used to investigate upon the effect of bone structure on the acoustic field. Except for these transcranial field assessment with AIMS, for most of the experiments the PXI was used as a research platform. Hence, the following section focuses mainly on setups that involved the PXI system.

2.8.1 Skull Response Studies

As a follow up to 2.7, the purpose of the studies was to assess the impact of skull on acoustic wave propagation. Ultimately, the goal was to find out whether increasing distances between transducer and skull impact signal detection and, if so, whether this is dependent on varying output voltage.

For skull response studies, any of the transducers was driven with the NI PXI-5421 waveform generator and data got acquired with the NI PXIe-5122. The PXI waveform generator was connected through a BNC-cable to its corresponding impedance matching network. To examine potential occurrence of nonlinear wave propagation at higher voltages, the power amplifier was required and inserted in between the waveform generator and the impedance matching circuit. The output of the impedance matching network was further connected to the transmit element of the transducer. On the receiver side, the PCD element was connected to the PXI data acquisition module. No analog filter in the receiving path was used for these studies. Transmission and acquisition were triggered simultaneously through a BNC connector of the arbitrary waveform generator and the DAQ. The PXI system was connected to a conventional computer screen.

The prototype transducer was mounted to a stainless steel rod, which attached to a customized holder to keep the transducer in a fixed position. The other end of the stainless steel rod was mounted to the 3D step motor system of the AIMS. The step motor system allowed to position the transducer at preset coordinates with respect to the skull bone at any given time.

In this experiment, the skull was positioned with its exterior temporal bone surface in various distances away from the transducer face. Distances of 0, 5, 10, 20 and 30 mm were evaluated.

Parameter Settings The transducers were driven by 20 cycles of 220 kHz (i.e. 90.90 μs). The amplitude of a pulse remained a variable throughout the studies. The intention was to cover effects caused by both, lower and higher driving voltages. Data acquisition operated at a sampling rate of 100 MS/s and collected 300,000 samples (i.e. 3 ms worth of data).

2.8.2 Microbubble Response Studies in AIMS tank

How microbubbles are responding to acoustic stimulation by the use of ultrasound, is one of the main research questions within the scope of this project. Initially, all measurements were performed in the AIMS tank with a flow system until the decision was made to translate the experiments from the wet tank to a small customized acrylic chamber. First and foremost an obvious benefit of the acrylic chamber is its smaller form factor. In addition, for reasons explained in 2.8.3, a larger microbubble volume is preferential to a flow system of relatively small volume compared to the acrylic chamber.

Flow System All measurements that include flow were performed in the AIMS tank, which was filled with degassed (<3 ppm), deionized water. Immersed into the water tank was a non circulating, open loop flow system. The flow system included a reservoir beaker, filled with 1500 ml of degassed, deionized water. The beaker was placed outside the water tank.

From the reservoir a 3/8“ flexible silicon tubing (Cole Parmer), the *Inlet*, was connected to an acrylic frame which was to 50% immersed below the water surface. The acrylic frame was mounted to an aluminum rod. The rod itself was fixed to an aluminum fixture mounted to the upper rim of the water tank. 5 cm below the water surface, a T-connector was mounted permanently to the acrylic frame and connected the plastic tubing with a PE test tube (length: 15 cm), preferred for acoustic measurements. The PE test tubing (Advanced Polymers) has an inner diameter of 0.170“ and a wall thickness of 0.003“. The third outlet of the T-connector was capped. The other end of PE test tube was connected to a second T-connector, permanently fixed to the acrylic frame as well, on its opposite side. From the second T-connector another plastic tube, the *Outlet*, ran outside the water tank into a second beaker, used as a waste water reservoir.

Flow Pump Between the reservoir beaker and the acrylic frame, the *Inlet* plastic tubing ran through a peristaltic pump (Masterflex L/S, Cole-Parmer Instruments) to create flow and no flow conditions. We were able to generate flow conditions between 0 - 500 ml/min with this pump. However, if not indicated differently, we generated 10 ml/min to match blood flow within the human brain.

Experimental Setup Overview The experimental setup was very similar to the one described in 2.8.1. In addition, the analog filters, customized for transducers 4.1 to 5.2, were used. The transducer was positioned in such a way that the center of the focus was aligned with the center of the PE tube at half its length. In average, the distance between transducer aperture and outer wall of the PE test tube was 4 cm. Figures 2.21, 2.22 and 2.23 show the general setup for experiments including a flow system.

Figure 2.21: Overview Setup with PXI and AIMS tank

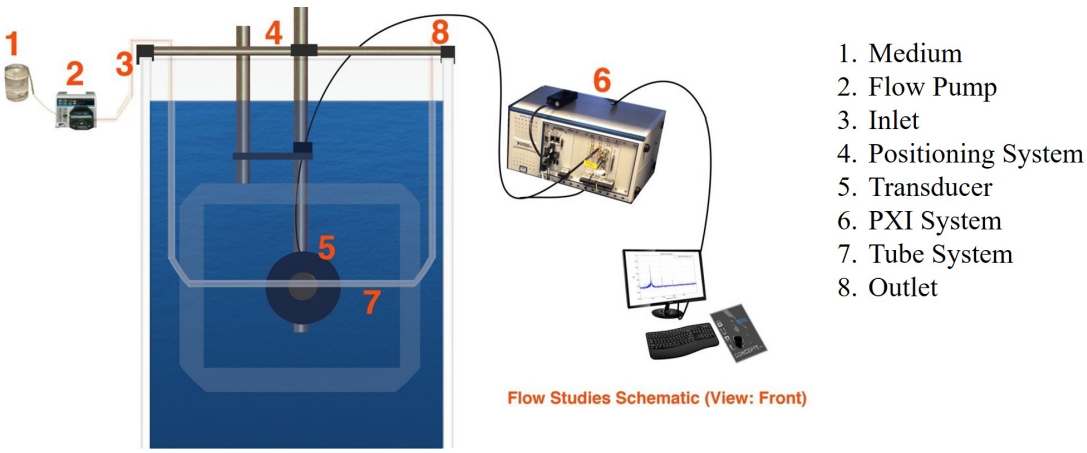

Figure 2.22: Flow Studies Schematic, Front View

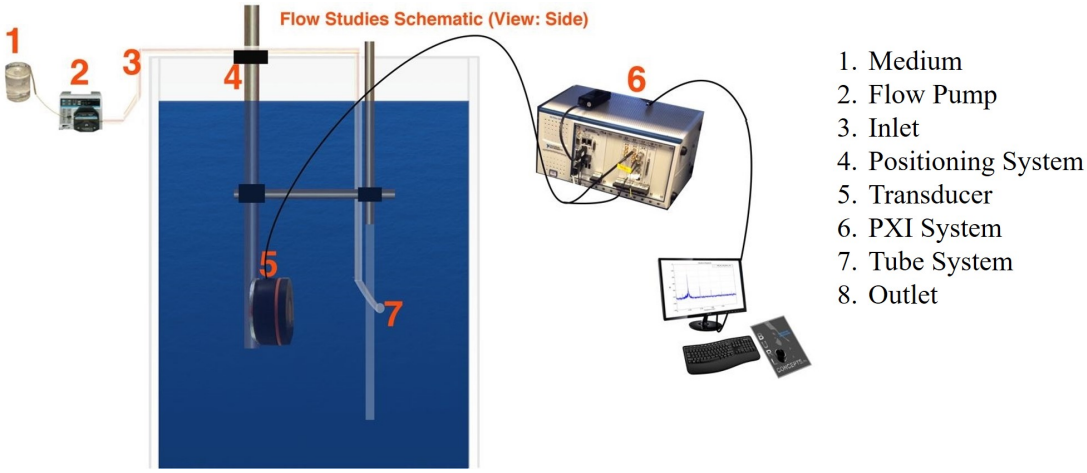

Figure 2.23: Flow Studies Schematic, Side View

Parameter Settings Measurements with the PE tube were done at an earlier stage of this research project when a pulsing scheme out of 16 available combinations (Table 2.2) was used to drive a transducer. A ramp-up, described in 2.4, was applied on all driving pulses. At three different input voltages, defined by the user, 100 pulses were transmitted and the first 50,000 samples of a response (i.e. 5 ms worth of data at sampling rate of 100 MS/s) were acquired simultaneously. All 50,000 points were stored in .TDMS files and used for post-processing in LabVIEW.

2.8.3 Microbubble Response Studies with Acrylic Chamber

At some point within the research, we agreed upon that the setup needs significant improvement in order to study microbubble responses. Although the PE tube has minimal impact on the acoustic field with regard to generation of harmonic content, it complicated measurements. The setup demanded accurate positioning of a transducers focal zone with regard to the tube. Furthermore, and more of relevance, was the fact, that the tube did not represent a very realistic scenario with regard to real life conditions. In biological tissue, microbubbles are distributed in the vascular system, which is essentially a volume of bubbly liquid rather than one vessel of small diameter similar to the PE tube. Transition to the acrylic chamber was accompanied by decreasing the transmitted pulse width to 20 cycles. This should first of all show whether microbubble excitation may be accomplished with very short pulses and furthermore prevent convolution of wall echoes within the chamber. In addition, we only transmitted one pulse per condition. Our concern was that we could not rule out microbubble destruction if more consecutive pulses are transmitted. All these facts convinced us of the more reasonable approach of microbubble response studies in the acrylic chamber, which was customized to provide the freedom to perform a variety of experiments.

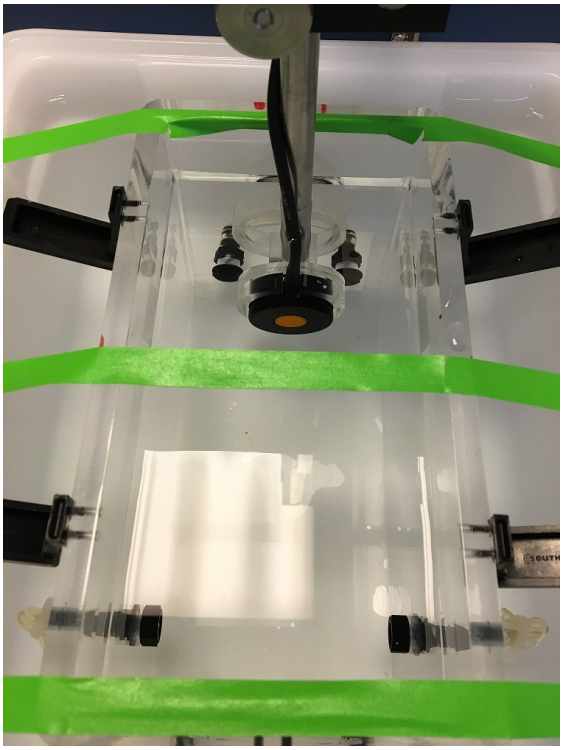

(a) Setup Microbubble Chamber with Transducer positioned inside

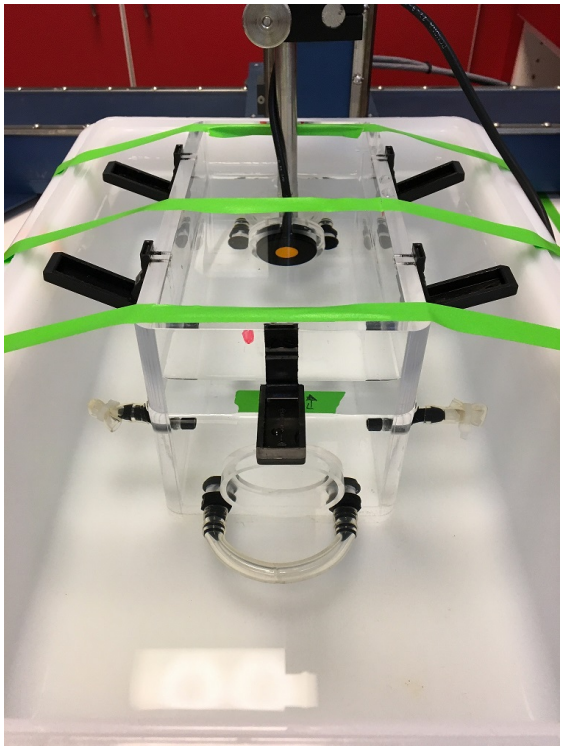

(b) Setup Microbubble Chamber with Transducer positioned outside

Figure 2.24: Setup Measurements with Acrylic Chamber

Experimental Setup Overview A transducer was placed either inside (Figure 2.24a) or outside (Figure 2.24b) the box depending whether the intention was to mimic intervening bone structure or not. The transducer was positioned that it transmitted along the longer side of the box. If inside, the transducers back was thereby as close as possible to the wall in order to maximize the propagation length. If outside, the transducers face was approximately 2 mm away from the wall.

Parameter Settings The transducers were driven with 10 or 20 cycles of 220 kHz (i.e. 90.90 μs). The amplitude of a pulse remained a variable throughout the studies. The intention was, again, to cover effects caused by both, lower and higher driving voltages. Data acquisition operated at a sampling rate of 100 MS/s and collected 300,000 samples (i.e. 3 ms worth of data). In addition, driving pulses were transmitted to allow pulse inversion in post-processing.

2.9 Animal Safety Studies

Animal studies were performed on rabbits in Cedars-Sinai Medical Center's Department of Neurology and Neurosurgery.

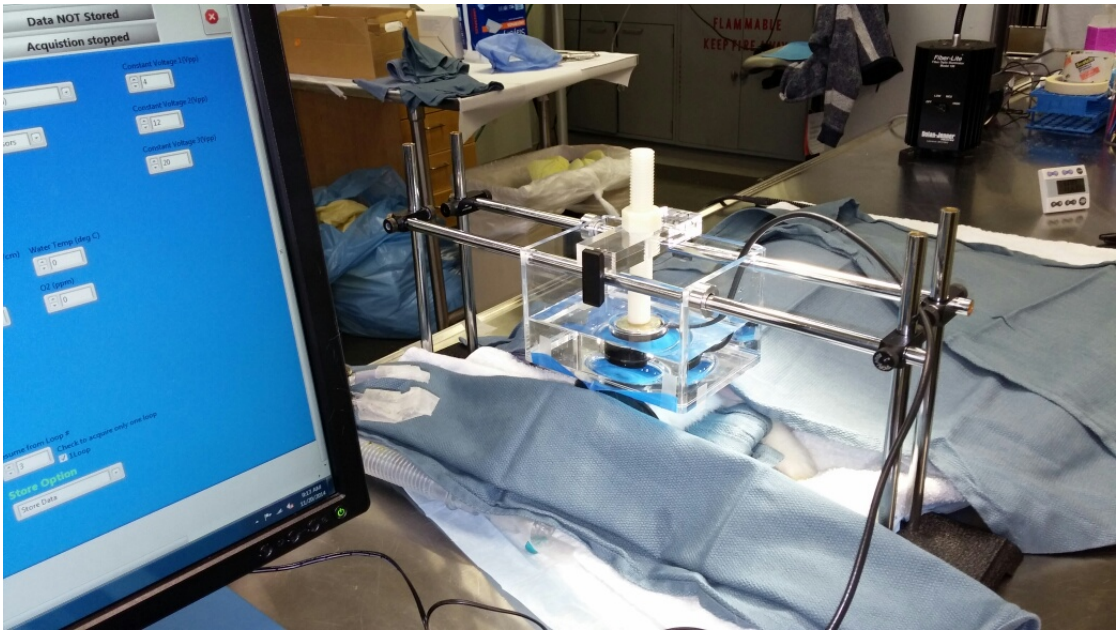

Figure 2.25: Animal Safety Studies Setup

Rabbit Groups Studies included healthy rabbits (also referred to as *normal*) and a *Small Clot Embolic Stroke group(SCEM)*. In the latter, ischemia was induced 90 minutes prior to ultrasound application.

Setup Overview The PXI waveform generator was used to drive transducer 4.1, including the associated impedance matching circuit as well as the power amplifier. Data was collected with the NI PXIe- 5122 data acquisition module. The analog filter customized for transducer 4.1 was used for any measurement. Figure 2.25 shows the small water bath positioned above the rabbits head for proper coupling of the transducer to the head. On the bottom, the box had a window in the size slightly larger than the transducer. After the window was covered with dental damn, the box was filled with degassed water that was heated up to match the rabbits body temperature prior to treatment. The box was lowered until the rabbit head started to dent the dental damn into the box.

Positioning The transducer was then immersed into the water bath above the rabbit head and lowered until the natural focus was located in the central-brain area. This was accomplished by setting the distance between the skulls bregma and the center of the transducer holding washer to a known value. Insonation was initiated and a real-time FFT display was furthermore used as a sanity check (e.g. no unusual high noise floor, no appearance of strong harmonic content).

Microbubbles Injection A solution of SonoVue microbubbles was injected intravenously as a bolus of 0.3 ml prior to a driving voltage ramp up to set the optimal individual output voltage

(i.e. *scouting*), followed by 30 minutes continuous insonation at this voltage value. Dosage and concentration of the 0.3 ml microbubble solution is equivalent to a double total dose in humans.

Parameter Settings Transcranial ultrasound of 5 ms pulse widths and PRT of 1 second (i.e. 0.5% duty cycle) was applied for a measurement time of 30 minutes per rabbit. The amplitude was defined according to the scouting procedure explained above.

Behavioral Assessment Score Changes in animal behavior over time, with special focus on stroke related symptoms, were monitored using the Behavioral Assessment Score for rabbits, developed by Lapchak et al.. This very well established Score allows to capture neurological deficits in a rabbit comparable to the *National Institute of Health Stroke Scale(NIHSS)* used in humans. Animals were monitored using the Score at the following time points:

- Time point 1: Prior to embolization / Pre collagenase injection
- Time point 2: After embolization / Post collagenase injection
- Time point 3: After ultrasound exposure
- Time point 4: After 24 hours
- Time point 5: After 48 hours

Serological Tests Blood was drawn to test for immediate tissue damage due to ultrasound only, or in combination with microbubbles. Therefore, venous blood draws were performed to assess *Matrix Metallo Proteinases(MMP)*, MMP 2 and MMP 9. MMP 2 and MMP 9 are known to degrade the major components of the BBB basal lamina (i.e. type IV collagen, laminin and fibronectin) and have been implicated in ischemic stroke. Blood samples were drawn at the following time points:

- Timepoint 1: Prior to the first isoflurane anesthesia
- Timepoint 2: After the first isoflurane anesthesia
- Timepoint 3: Prior to ultrasound exposure
- Timepoint 4: Immediately after ultrasound exposure
- Timepoint 5: 24 hours after ultrasound exposure
- Timepoint 6: 48 hours after ultrasound exposure

2.10 Human Cadaver Studies

Studies were done on two human cadaver heads at the University of California, San Diego (UCSD) School of Medicine.

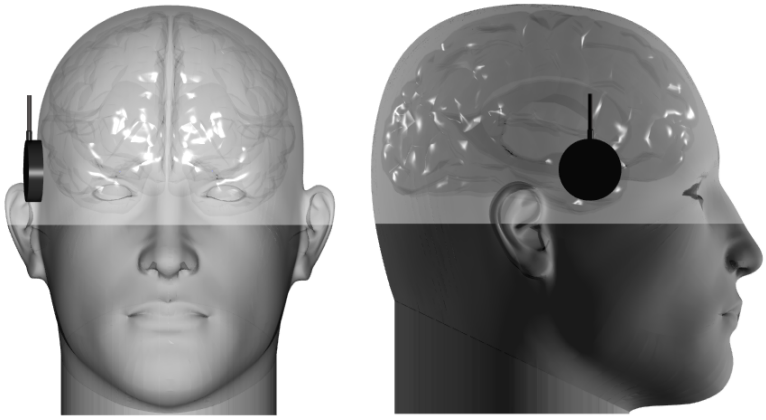

Figure 2.26: Transducer Positioning, Human Cadaver Studies

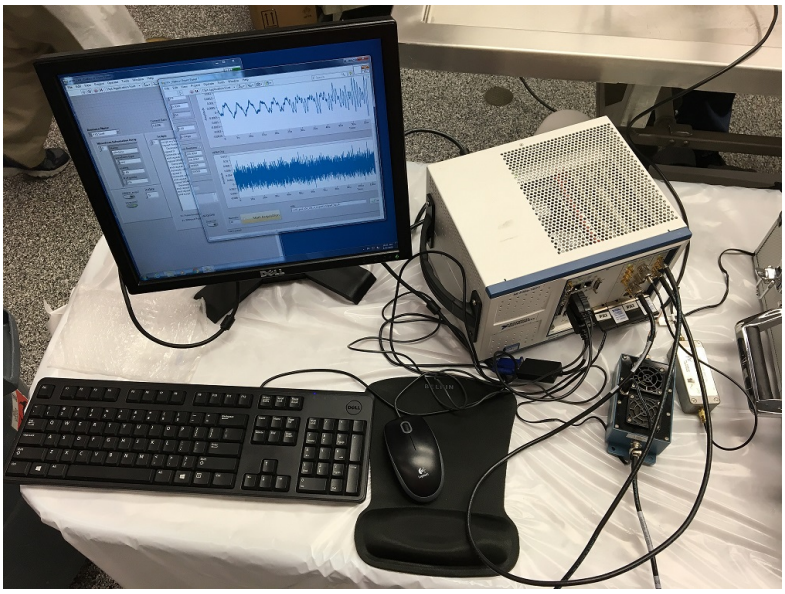

Figure 2.27: Human Cadaver Studies, PXI setup

Experimental Setup Overview Transducer 5.2 was positioned with its face upon the right temporal bone window and coupled to the skin by commercially available ultrasound coupling gel, according to Figure 2.26. To improve conductivity, gentle pressure was applied to the transducer. Using the first head, we acquired data at four different transducer positions with respect to the temporal bone window. For the second head the transducer remained at one position.

Parameter Settings In the scope of the studies, we used transducer 5.2 in combination with the PXI system to drive the transducer, to acquire and store tissue and microbubble responses

2.27. A LabVIEW algorithm performed a driving voltage modulation from 5 V_{PP} to 50 V_{PP} in 5 V_{PP} increments. A single transmitted pulse had a pulse width 10 cycles at 220 kHz (i.e. 45.45 μs) and a PRT of 100 ms. Acoustic responses were acquired and stored in a single dataset of 300,000 samples at a 100 MHz samling rate (i.e. 3 ms) per voltage. The amplitude modulation dataset consisting of 10 voltage steps was done with and without analog bandpass filter in the receive path. Note, that for the second cadaver head for the dataset with the analog bandpass filter, two consecutive pulses of inverted phase were transmitted in order to enable the *pulse inversion* feature in post processing.

Perfusion and Microbubble Application The second cadaver head was placed in a custom fixture to provide a supine, secured position. Both carotid arteries were catheterized and connected to the perfusion pump via a Y-shaped tube system. The perfusion device allowed to adjust for perfusion speed as well as perfusion pressure. Using a Y-shaped tube system allowed to perfuse both hemispheres simultaneously. Perfusion speed and pressure were adjusted on site as needed and to provide sufficient saturation with microbubbles in one of the hemispheres over an extended time window.The experimental set up allowed us to perfuse the brain very closely matched to the physiological perfusion in a living human. Once proper positioning was confirmed we unsuccessfully tried to establish brain perfusion with saline. As we noted, this was due to unsuitable preparation of the specimen for our purpose.

2.11 Acoustic Response Analysis in LabVIEW

Acoustic response analysis was done with a variety of analytical tools. Several standard tools for spectral analysis, such as a Fourier- or Gabor-Transformation are already implemented in LabVIEW. Other methods, such as the statistical support-vector machine or Matched Filters, needed to be programed.

Ultimately, the analytical approach depends on the main objective of the experiment. Initially, FFT was our tool of choice to examine acoustic responses of microbubbles and biological tissue. Our intention to have a more statistically way to characterize microbubble behavior made us consider the Support-Vector Machine. This approach, however, turned out to be impracticable for any real-time evaluation. About this time, we suspected a strongly time-variant microbubble response to cause inconclusive results and added the Gabor transform as a confirmation method. Again, because of its memory consumption, the Gabor transform was considered as an offline tool only. Ultimately, when we changed to shorter pulses, we started migrating to an signal detection approach that uses Matched Filters (i.e. Cross Correlation).

FFT The *FFT Spectrum (Mag-Phase) VI*, included in the *Waveform Measurements VIs* palette, was, for the vast majority of measurements, the main tool to prepare data for analysis. In general, the FFT requires a certain time window to be provided in the beginning that has to be chosen depending on the experimental condition. The VI furthermore allowed the us to select a either a Hanning Window or Blackman Harris Window amongst other Windows to be applied on the time signal prior to transforming it into the frequency domain. In fact, both Windows are very similar to each other and there is no wrong choice. A Hanning or Blackman-Harris Window is

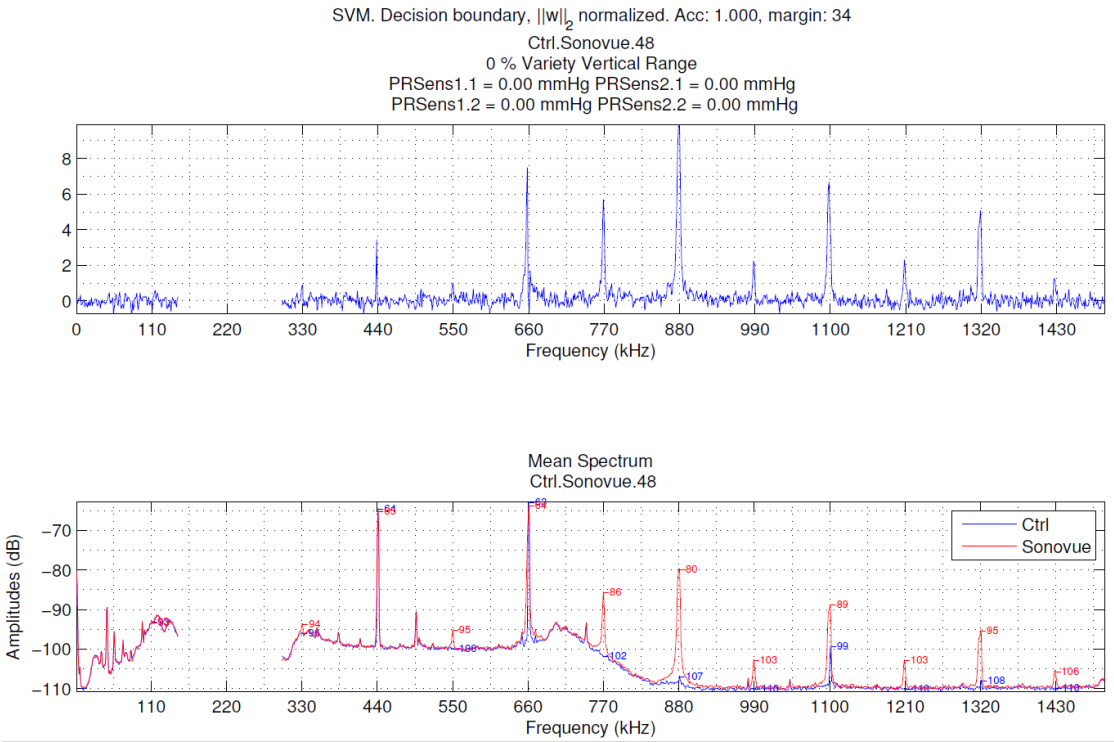

Figure 2.28: Example for SVM Result

applied to reduce the broadband leakage and bring out smaller signals. In the frequency domain, both Windows have a wide peak and low side lobes. In case of the Blackman-Harris Window the side lobes are better suppressed compared to a Hanning Window.

Support-Vector Machine Initially, the classification method SVM was implemented in MATLAB so that two datasets acquired under different conditions can be classified in a statistical way. For purpose of simplification the algorithm was translated into LabVIEW. The program calculated a margin and an accuracy of which both are shown in the header of the upper SVM plot. Furthermore, the lower plot displayed the mean FFT of all FFTs under one specific condition. The values above each peak along all frequencies of interest represent the peak amplitudes in decibel. Note, the intentional gap from 150 to 300 kHz. If no analog filter was used, the fundamental frequency caused the margin to be very high. However, this information was considered at meaningless. In analysis, the first step was to observe the differences in amplitudes of the mean spectra for each frequency of interest. Once this was done, the margin value indicated how separable the two datasets are. Ideally, the accuracy has its maximum value of 1.00.

Gabor-Transform The Gabor-Transform was part of the *Advanced Signal Processing Toolkit* in LabVIEW and the main VI that actually performed the operation was called *TFA Discrete Gabor Transform VI*. The Gabor coefficients were displayed in a 2D intensity plot 2.29. The

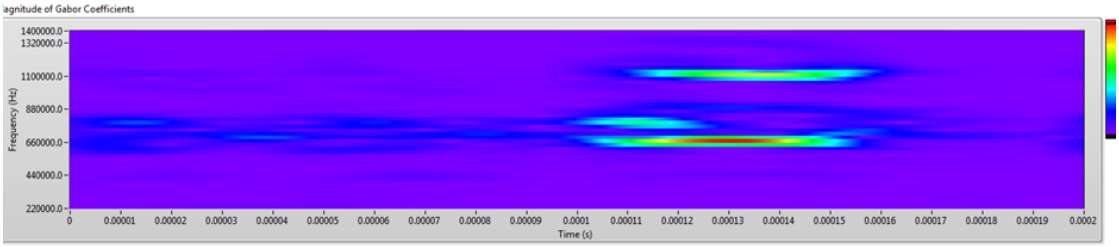

Figure 2.29: Example of a 2 ms Pulse examined with Gabor Transform

x- axis represented the time in seconds, the y-axis frequency in Hertz. A color bar showed the intensity of the signal. Prior to using the Gabor-Transform, the fundamental was filtered with a digital bandstop filter if it was not already filtered with one of the analog filters before digitization. Similar to the reason why an analog filter was used during data acquisition the reason for canceling the fundamental frequency digitally was its dominant character. If no filter was applied only the fundamental frequency component was clearly present in the graph.

Matched Filters A matched filter (i.e. cross correlation) approach programed in NI LabVIEW was used to detect signals. Essentially, as explained in the Introduction, Matched Filters are similar to the Cross-Correlation Function. In LabVIEW the TSA Cross-Correlation Function VI computeed the cross-correlation of two time series x(t) and y(t), whereas x(t) was the acquired signal and y(t) represented the correlation signal. The matched filter/correlation signal (i.e. signal to be detected within acquired signal) was a 1 V_{PP} sinusoidal waveform with a pulse width of 45.45 μs generated in LabVIEW. This signal was tuned to frequencies from 220 kHz to 1540 kHz in 110 kHz steps. Each matched filter was then applied to the first 80 μs of the acquired baseline dataset. The result was a correlation function of 125.45 μs (i.e. sum of acquired signal and correlation signal). For each frequency, we computed the average magnitude of the correlation function over the 125.45 μs. This number represented a common measure of the average signal energy at that specific frequency in that time window. This value was then recorded in a table for each measurement case (tissue or microbubble) for later comparison.

Additionally, for each frequency, for acquired time signals and correlation functions, for both the baseline as well as the microbubble dataset, the time domain plots were captured and stored as an image file on the processing system for data review sessions.

2.30 shows an example of a Matched Filter result for 880 kHz per definition by the user. The plot indicates the sampling rate and the number of samples used to generate the correlation signal y(t). In addition to these two parameters the user is furthermore allowed to specify which dataset (i.e. Dataset Index Control) should be used to calculate the *detection threshold*. The detection threshold, represented by the green line in 2.30, is a constant value calculated by the following equation:

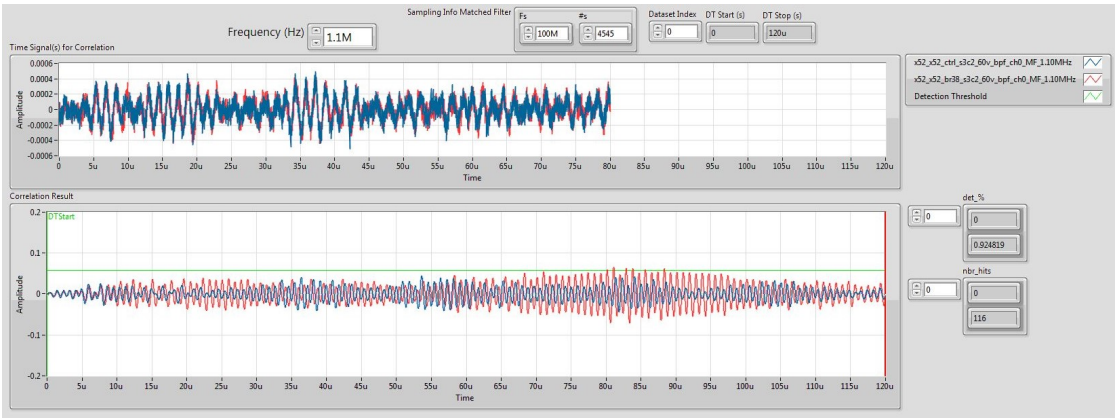

Figure 2.30: Example of 80 μs Pulse analyzed with a Matched Filter tuned to 1.1 MHz

CHAPTER 3

Results

3.1 Transducer Characterization

A complete transducer characterization comprises Impedance Measurements, 3D Acoustic field scans as well as analysis of the individual frequency components.

3.1.1 Impedance Measurements

Impedance measurements were done for each transducer. Figures 3.1a to 3.2b show the matched transmitter impedance over a frequency range from 100 to 440 kHz in 2 kHz increments for transducer 5.1 and 5.2. For transducer 5.1 the impedance expressed in rectangular form is 42.20-18.49 iΩ at 220 kHz. At the same frequency, transducer 5.2 has an impedance of 42.23+17.81 iΩ.

Figure 3.3a to 3.4b are the results of the impedance measurements of PCD elements of transducer 5.1 and 5.2. For transducer 5.1 the PCD impedance is 98.3-647.4 iΩ at a frequency of 1 MHz. Transducer 5.2 shows an impedance of 96.1-661i iΩ at the same frequency.

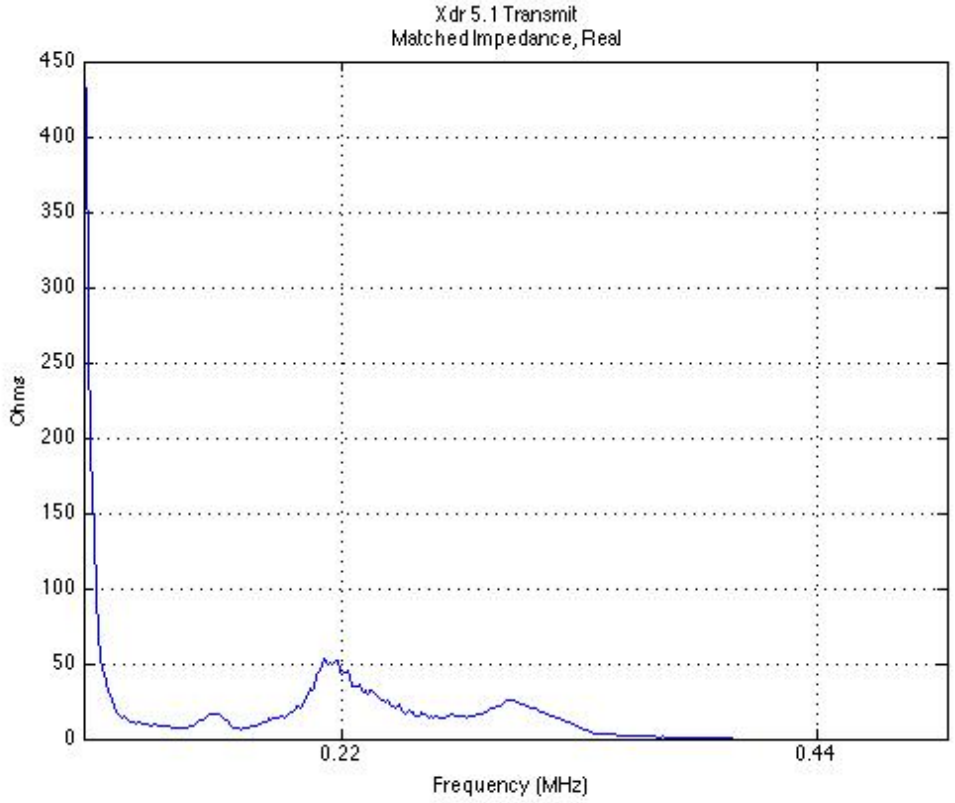

(a) Impedance Real

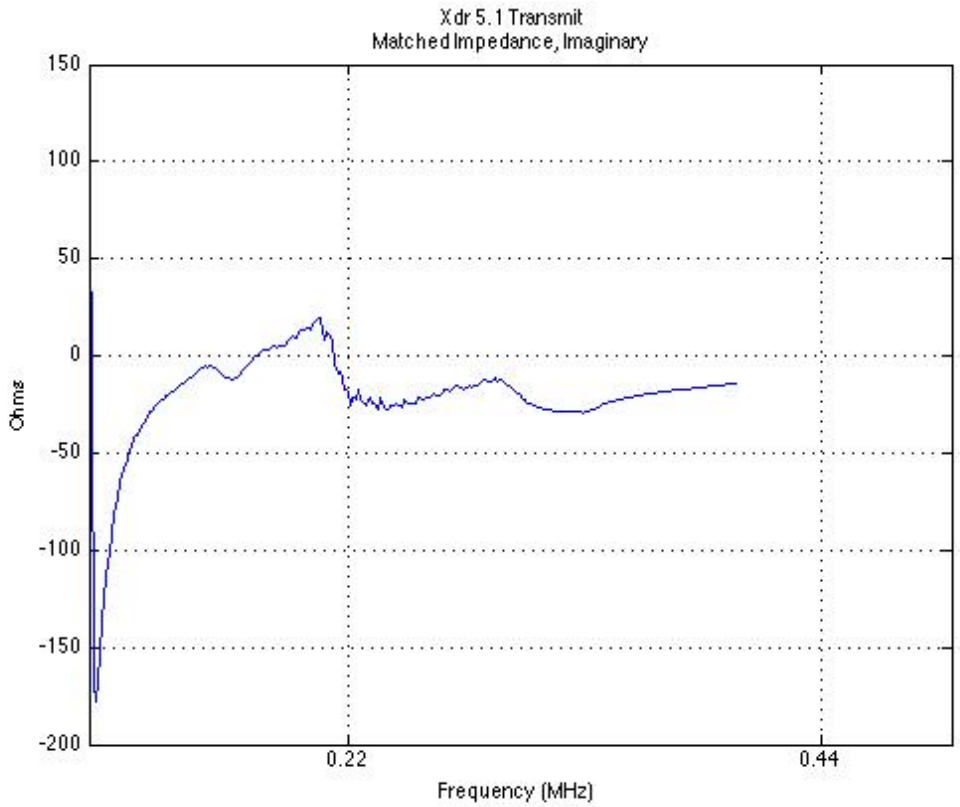

(b) Impedance Imaginary

Figure 3.1: Xdr 5.1 Transmitter, Matched Impedance

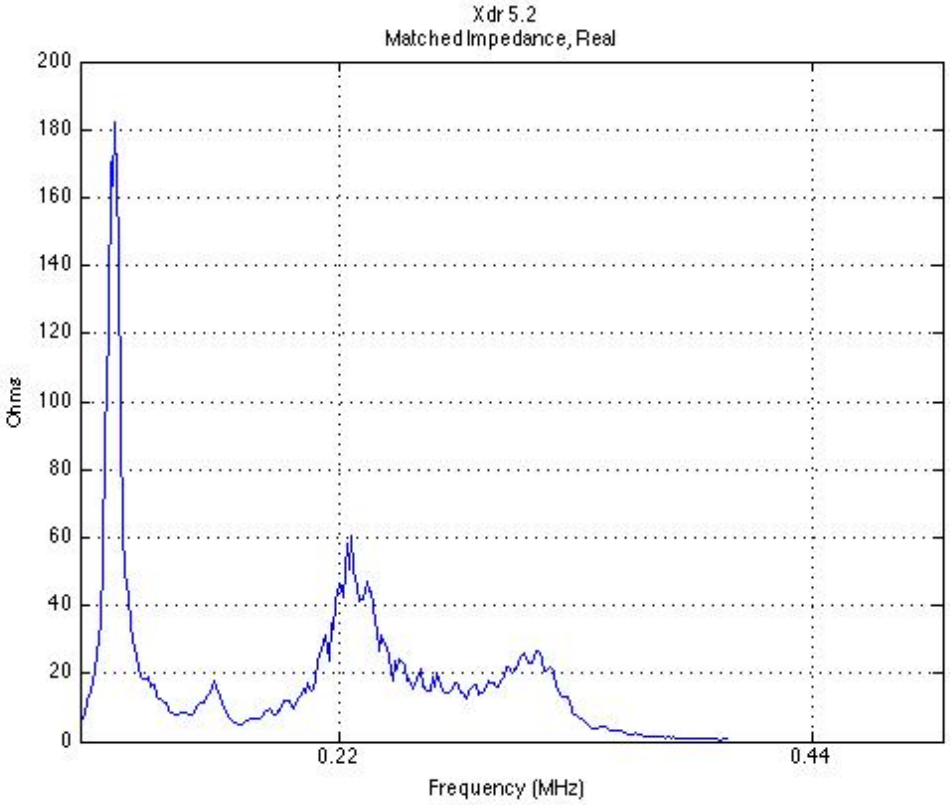

(a) Impedance Real

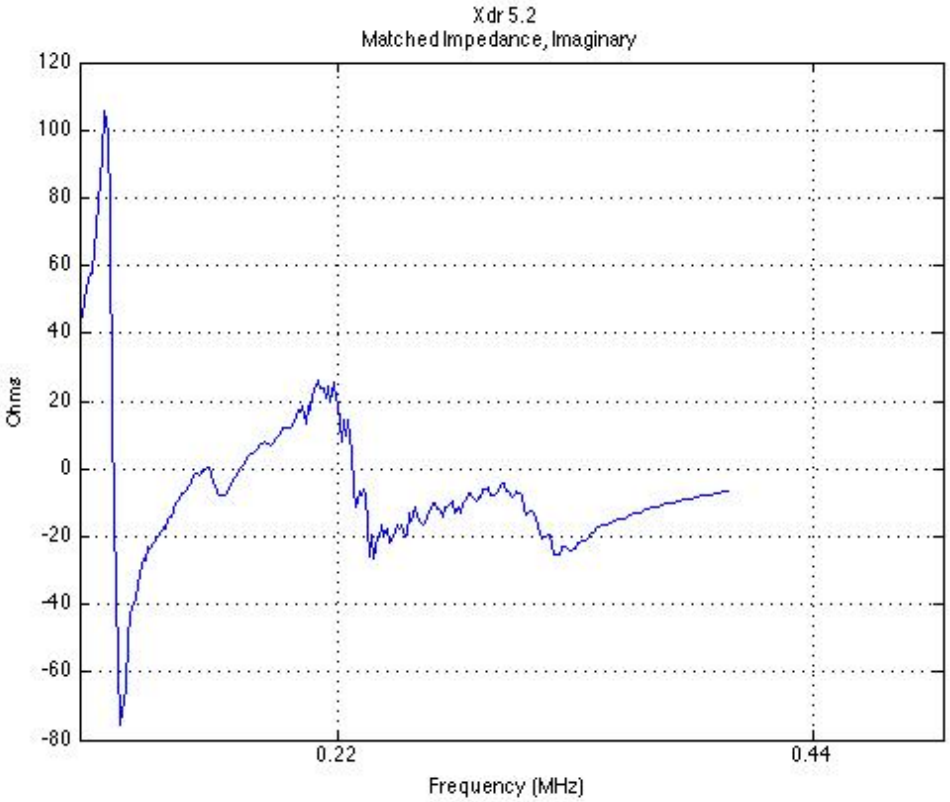

(b) Impedance Imaginary

Figure 3.2: Xdr 5.2 Transmitter, Matched Impedance

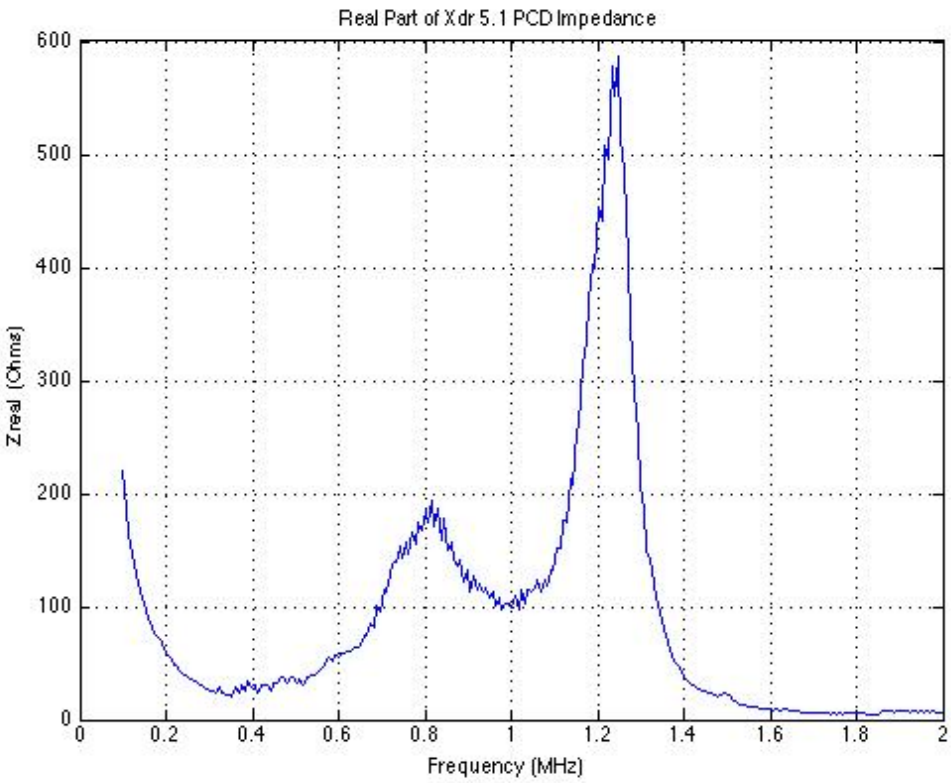

(a) Impedance Real

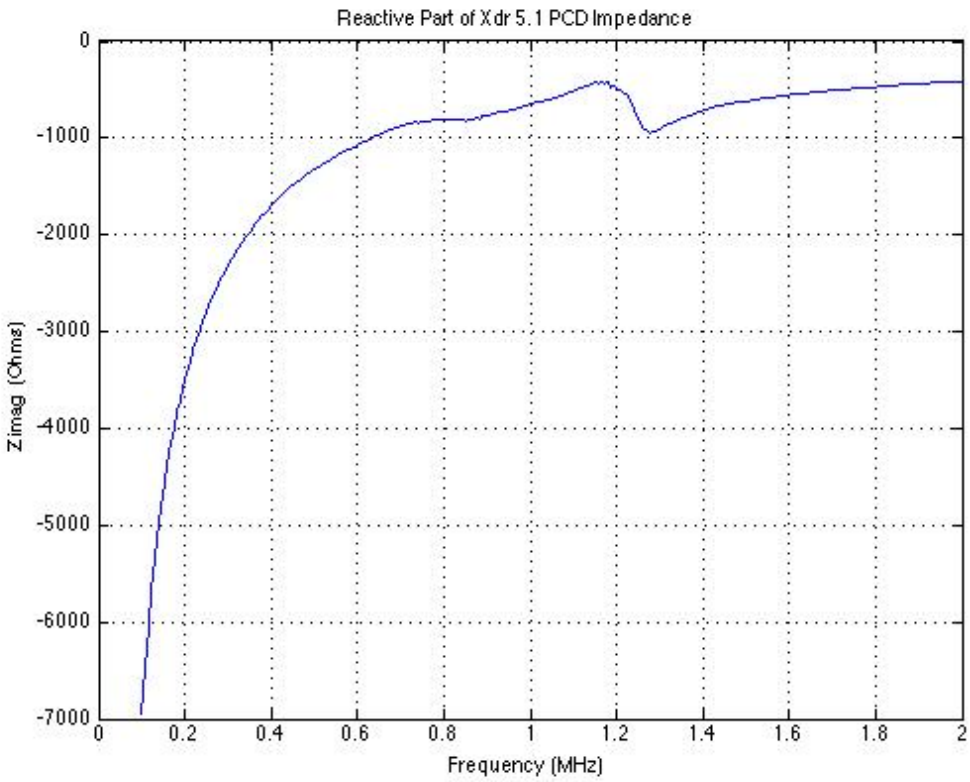

(b) Impedance Imaginary

Figure 3.3: Xdr 5.1 Receiver Impedance

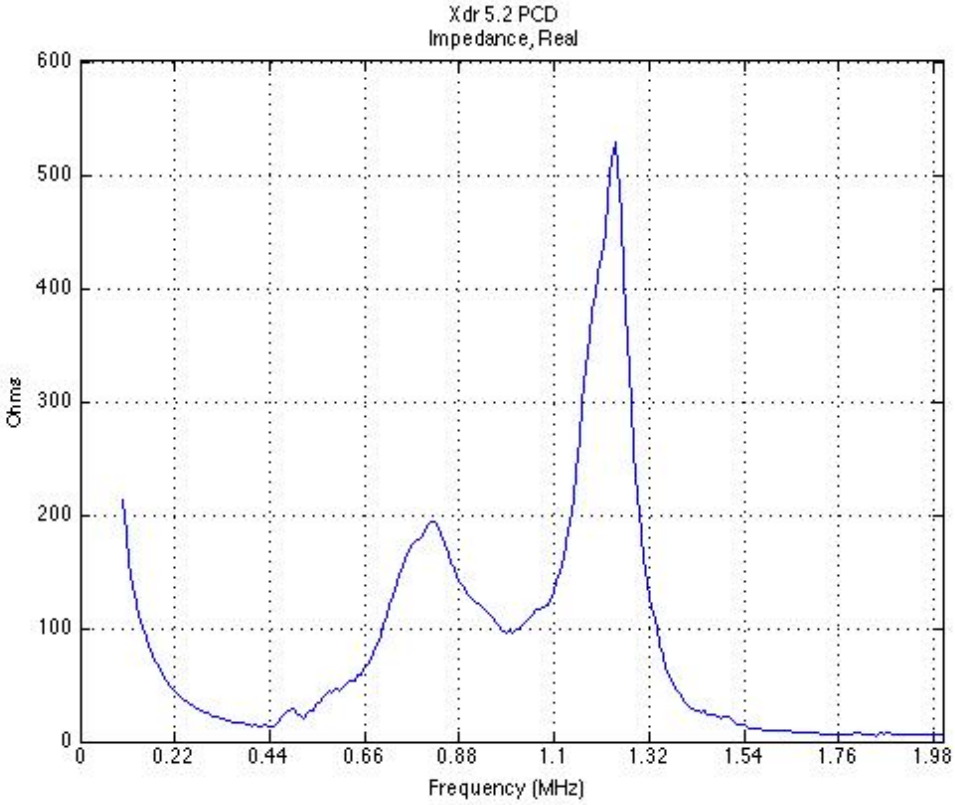

(a) Impedance Real

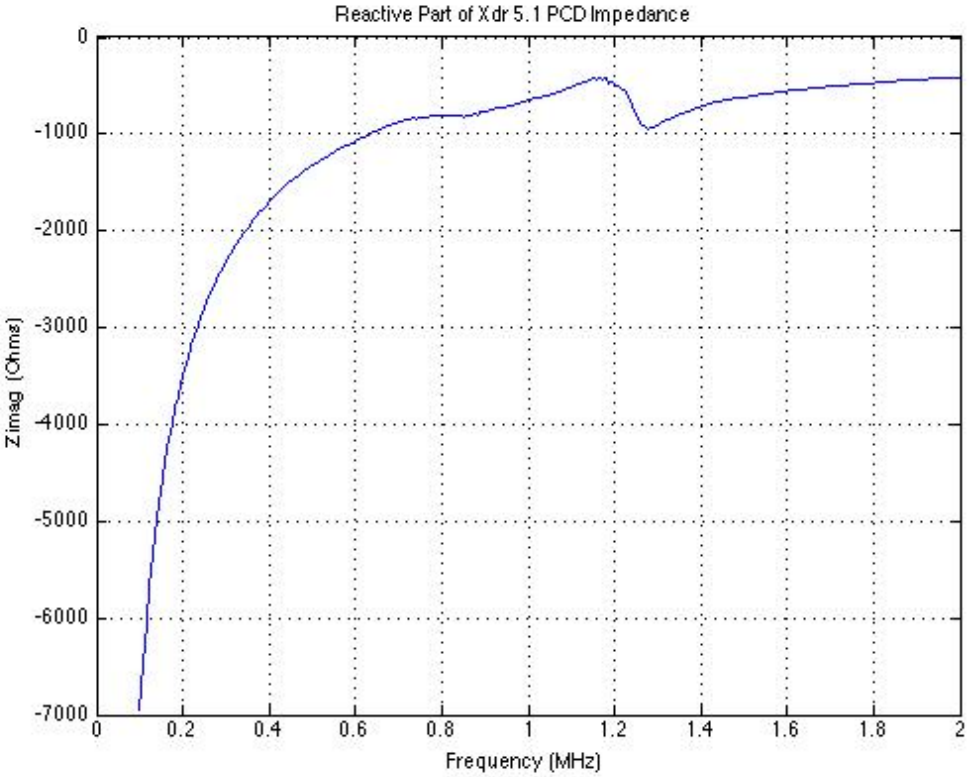

(b) Impedance Imaginary

Figure 3.4: Xdr 5.2 Receiver Impedance

3.1.2 Field Characterization

In the following (Figures 3.5a to 3.8c) results of the free-field measurements are shown for transducer 4.1, 4.2, 5.1 and 5.2. Three Figures per transducer indicate the peak negative pressure if the hydrophone is moved along the propagation axis (i.e. *axial*), from left to right in the focal zone (i.e. *lateral*) or in the 3D space (i.e. *orthogonal*).

3.1.2.a Transducer 4.1 Efficiency

Transducer 4.1 delivers a maximum peak negative pressure of 64 kPa at a distance of 29 mm away from the transducer surface (Figure 3.5a, 3.5b and 3.5c)

3.1.2.b Transducer 4.2 Efficiency

Transducer 4.2 delivers a maximum peak negative pressure of 57 kPa at a distance of 30 mm away from the transducer surface(Figure 3.6a, 3.6b and 3.6c).

3.1.2.c Transducer 5.1 Efficiency

Transducer 5.1 delivers a maximum peak negative pressure of 52 kPa at a distance of 36 mm away from the transducer surface(Figure 3.7a, 3.7b and 3.7c).

3.1.2.d Transducer 5.2 Efficiency

Transducer 5.2 delivers a maximum peak negative pressure of 55 kPa at a distance of 30 mm away from the transducer surface(Figure 3.8a, 3.8b and 3.8c).

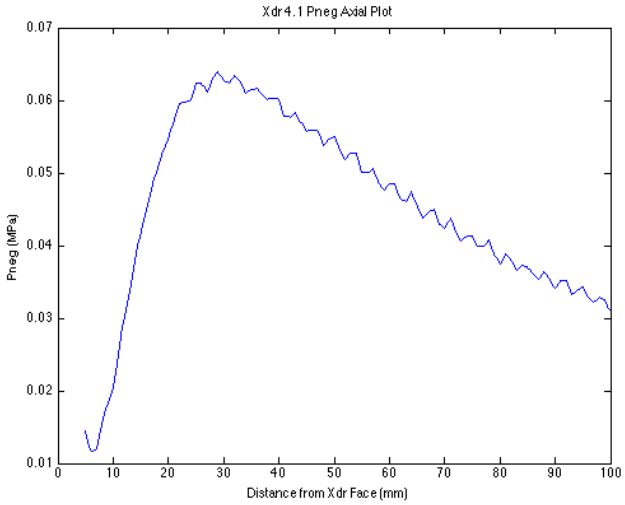

(a) PNP Axial Xdr 4.1

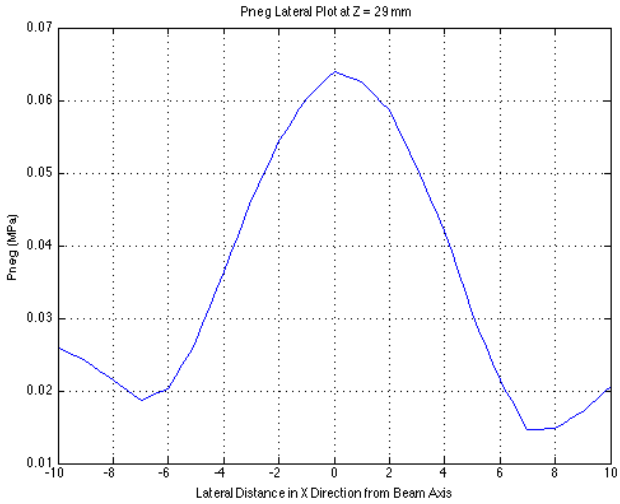

(b) PNP Lateral Xdr 4.1

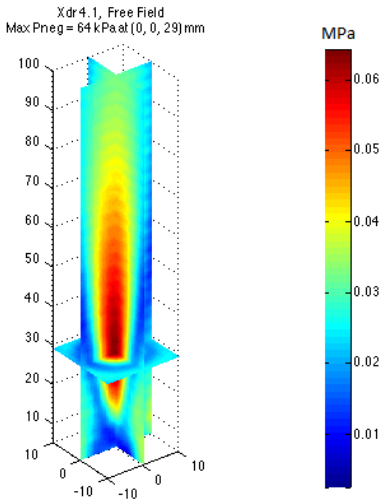

(c) PNP Orthogonal Xdr 4.1

Figure 3.5: Acoustic Field Scans 3D, Xdr 4.1

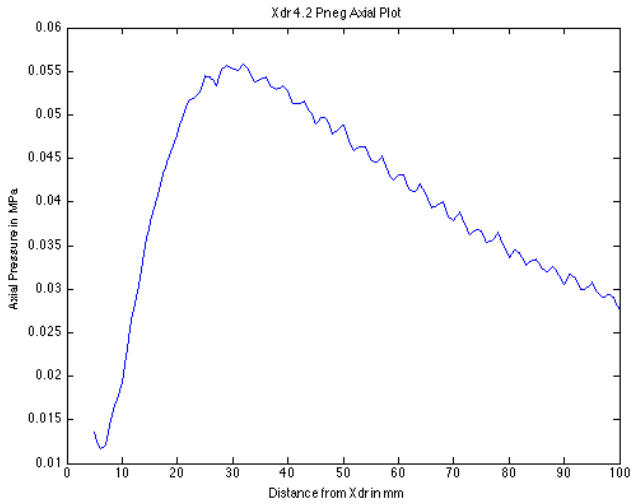

(a) PNP Axial Xdr 4.2

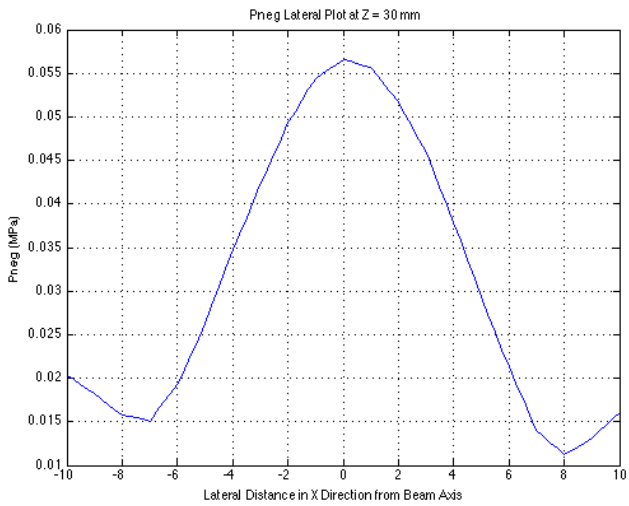

(b) PNP Lateral Xdr 4.2

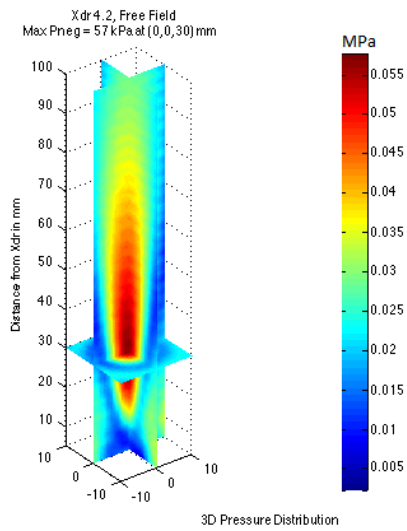

(c) PNP Orthogonal Xdr 4.2

Figure 3.6: Acoustic Field Scans 3D, Xdr 4.2

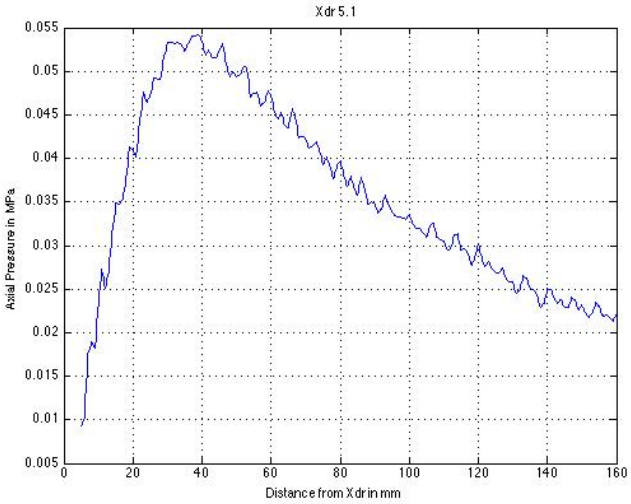

(a) PNP Axial Xdr 5.1

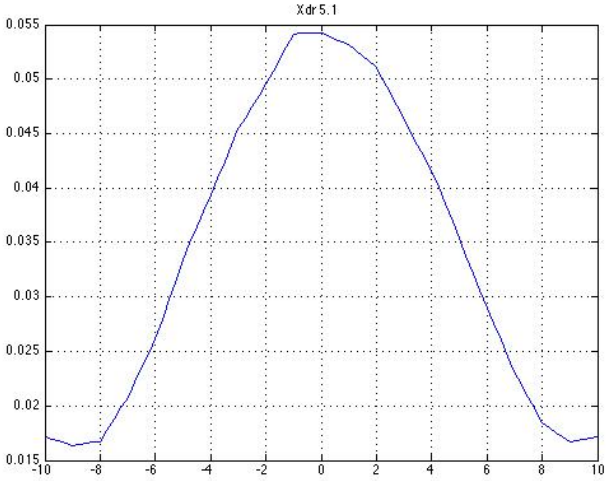

(b) PNP Lateral Xdr 5.1

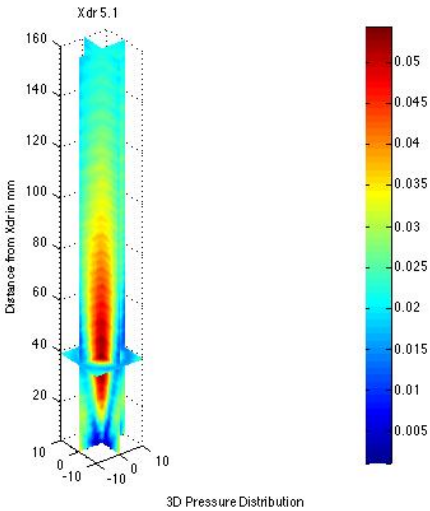

(c) PNP Orthogonal Xdr 5.1

Figure 3.7: Acoustic Field Scans 3D, Xdr 5.1

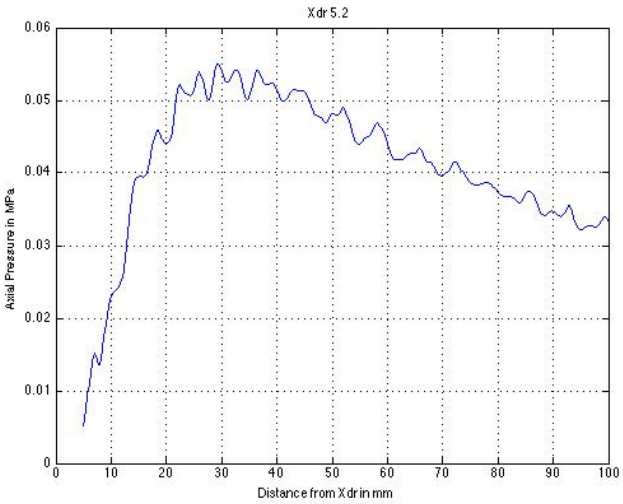

(a) PNP Axial Xdr 5.2

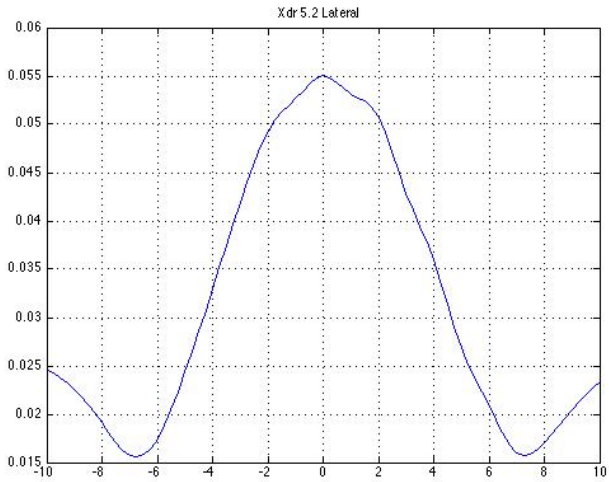

(b) PNP Lateral Xdr 5.2

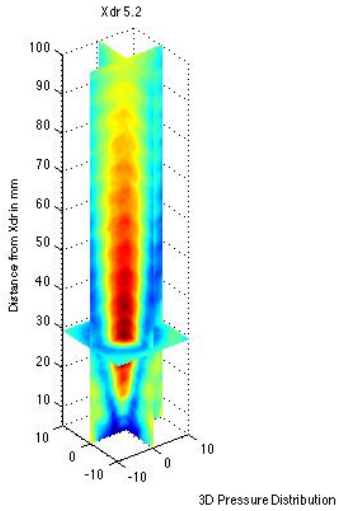

(c) PNP Orthogonal Xdr 5.2

Figure 3.8: Acoustic Field Scans 3D, Xdr 5.2

3.1.2.e Transducer 5.2 Sensitivity

Table 3.1 indicates the results of sensitivity measurements if the 1 MHz broadband transducer was driven at frequencies of 880, 1100 and 1320 kHz and the hydrophone was positioned along the acoustic centerline as a listening device. The first column shows the distance between hydrophone and transducer. The next columns show the following per frequency:

- average pressures being calculated over the 2D surface that the hydrophone scanned(i.e. Xmit on PA768, Y120 PMean(MPa))
- received voltage on PCD of transducer 5.2 in V_{PP} if the Y120 hydrophone is exchanged by transducer 5.2 and
- sensitivity calculated as $\mu V_{PP}/Pa$ based on the two previous items.

As for reasons explained in 2.5.3, we later changed to a different method of determining sensitivity. The following Figures 3.9, 3.10 and 3.11 show the pressure distributions if 5.1 is transmitting at 880, 1100 and 1320 kHz (i.e. driving receiver backwards) and transducer 5.2 placed opposite to 5.1 at a distance of 20 mm.

Table 3.1: PCD 5.2 Sensitivity Measurements

	Xmit on PA768 Y120 Pmean(MPa)			Rcv V on PCD 5.2 (V_{PP})			Sensitivity Values (μV_{PP}/Pa)		
Distance (mm)	880	1100	1320	880	1100	1320	880	1100	1320
20	0.0415	0.0376	0.0290	13.27	12.18	9.43	320	324	325
30	0.0419	0.0386	0.0309	13.83	12.46	9.63	330	323	312
40	0.0425	0.0399	0.0323	14.15	12.58	9.94	333	315	308
50	0.0433	0.0405	0.0335	14.38	12.84	9.98	332	317	298
60	0.0414	0.0413	0.0332	14.29	12.91	10.26	345	312	309
70	0.0402	0.0414	0.0340	14.41	13.07	10.38	358	316	305
80	0.0405	0.0403	0.0345	14.96	12.94	10.38	369	321	301
90	0.0414	0.0392	0.0340	15.44	13.00	10.22	373	332	301
100	0.042	0.0384	0.0326	15.58	13.17	10.43	371	343	320
110	0.0423	0.0387	0.0311	15.73	13.56	10.43	372	350	335
120	0.0423	0.0390	0.0312	15.66	13.63	10.38	370	350	333
130	0.0418	0.0396	0.0311	15.44	14.00	10.40	369	354	334
140	0.041	0.0398	0.0315	15.10	13.90	10.70	368	349	340
150	0.0401	0.0395	0.0319	14.90	14.07	10.73	372	356	336
160	0.0391	0.0393	0.0325	14.50	13.71	10.72	371	349	330

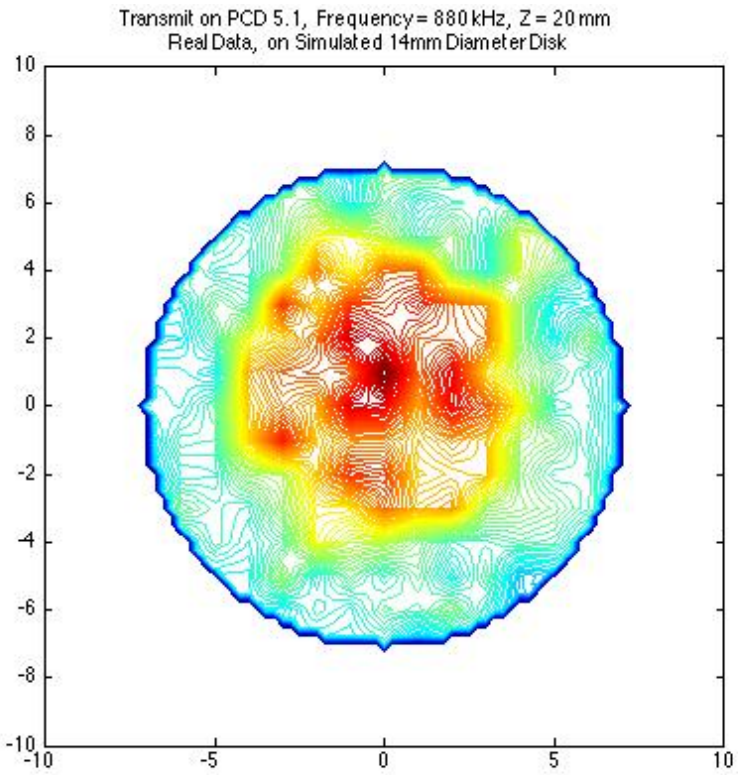

Figure 3.9: 880 kHz PNP distribution on Xdr5.2 PCD element

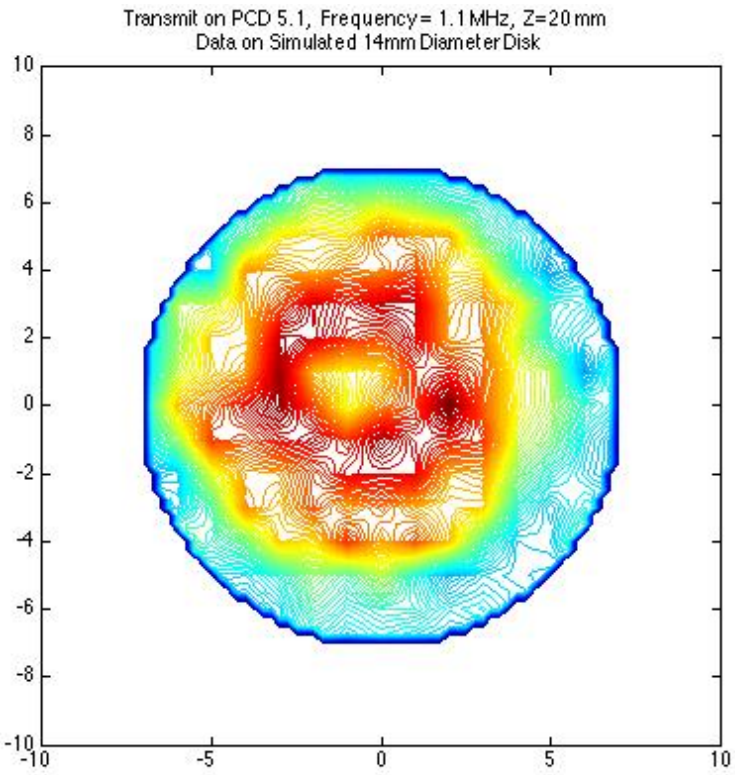

Figure 3.10: 1100 kHz PNP distribution on Xdr5.2 PCD element

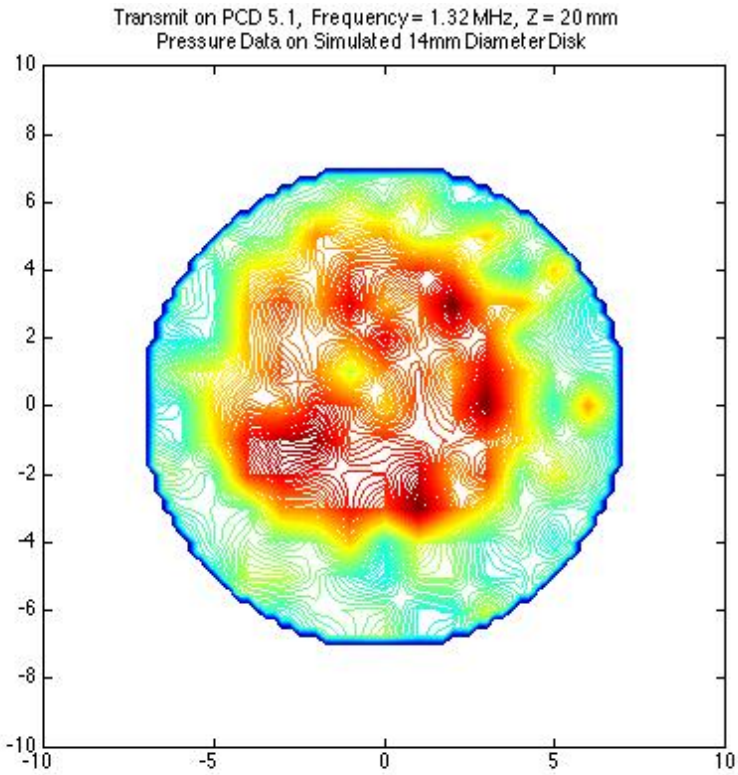

Figure 3.11: 1320 kHz PNP distribution on Xdr5.2 PCD element

3.1.3 Analysis of Time Signal and individual Frequency Components

Figure 3.12 shows an example of a received signal with the PCD element of transducer 5.1 in the free field of the acrylic chamber. 300,000 points were acquired at a sampling rate of 100 MS/s with the PXIe-5122 data acquisition module. In the following Figure 3.13 only 0 to 200 μs of the entire signal are shown in order examine transducer specific characteristics, such as *ringing*. The red cursor is set to 38.4 μs and the green cursor to 89.42 μs.

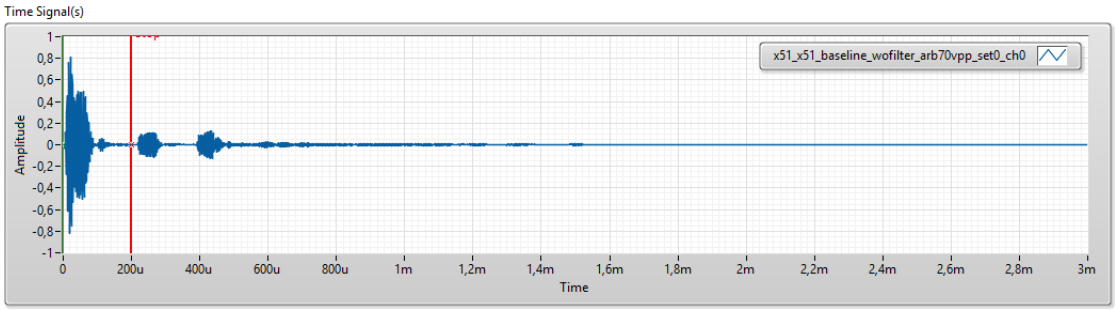

Figure 3.12: Received Time Signal, Free Field, Xdr5.1, 70 V_{PP}

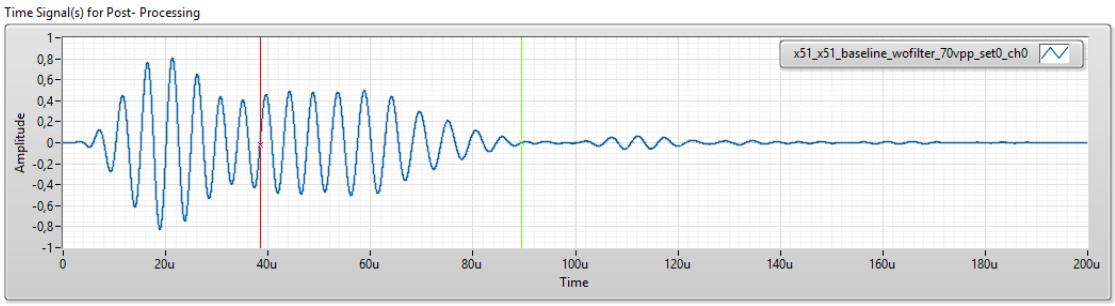

Figure 3.13: Time Domain Analysis, Received Signal, Free Field, Xdr5.1, 70 V_{PP}, 0 to 200 μs

With the aim to perform spectral analysis on the isolated transmit signal, we applied a rectangular window from 38.4 μs to 89.42 μs (i.e. counting 10 cycles backwards from ring-down end). The FFT was performed on this time part and is plotted in Figure 3.14. In the upper left corner, the time part considered for the FFT is shown. The lower plot shows the same signal when a Blackman Harris Window was applied.

A comparison between transducer 4.2 and 5.1 is shown in Figure 3.15, which is the received time signal from 0 to 300 μs.

Figure 3.16 shows an overlay of time signals when the driving signal is varied with regard to number of cycles. Used number of cycles were 1, 3, 5, 7 and 10, with transducer 5.2 at 70 V_{PP}.

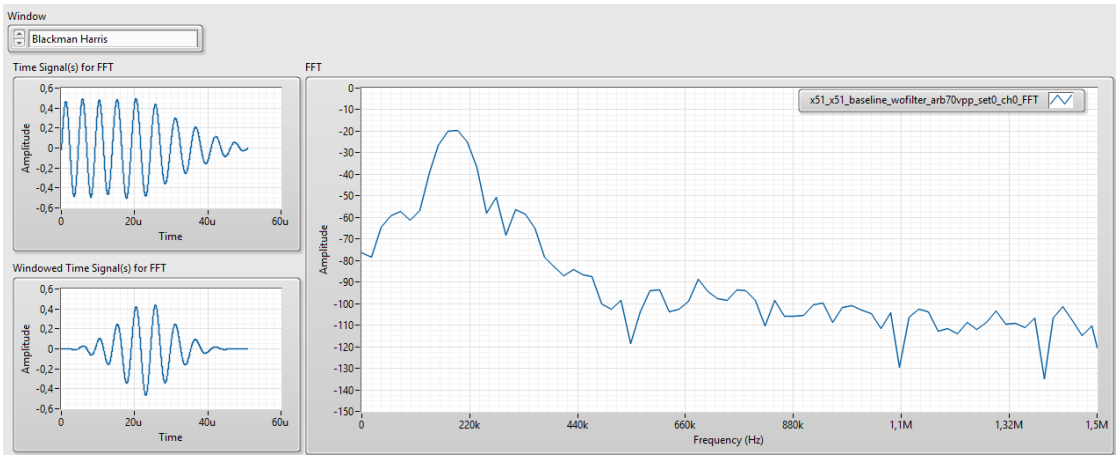

Figure 3.14: Frequency Domain Analysis, Received Signal, Free Field, Xdr5.1, 70 V_{PP}, 38.4 to 89.42 μs

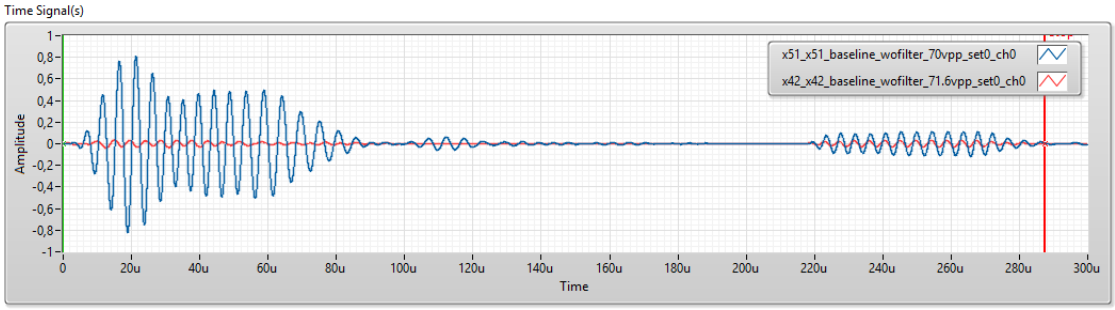

Figure 3.15: Time Domain Analysis, Received Signal, Free Field, Xdr5.1 at 70 V_{PP} and Xdr4.2 at 71.6 V_{PP}, 0 to 300 μs

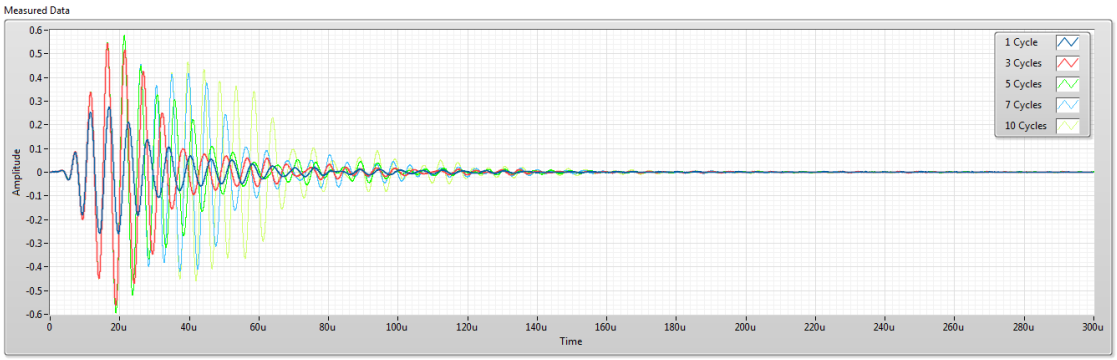

Figure 3.16: Time Signal X52; Overlay 1 cycle, 3, 5, 7, 10 cycles

Table 3.2: Mechanical Index(MI), Thermal Index Cranial(TIC), I_{SPTA}

PA (V_{PP})	PNP (kPa)	Power (W)	MI	TIC	I_{SPTA} (mW/cm^2)
10	58.8	0.18	0.13	0.01	0.58
20	117.9	0.71	0.25	0.03	2.32
30	171.9	1.52	0.37	0.06	4.92
40	235.7	2.86	0.50	0.12	9.26
50	295.0	4.48	0.63	0.19	14.50
60	354.7	6.47	0.76	0.27	20.97
70	414.5	8.84	0.88	0.37	28.64
80	471.6	11.44	1.01	0.48	37.07
90	532.8	14.60	1.14	0.61	47.31
100	586.5	17.69	1.25	0.74	57.33

3.2 Mechnical Index, Thermal Index Cranial, Intensity Calculations

Table 3.2 shows (from left to right) the output of the power amplifier in V_{PP}, measured *PNP* in *kPa*, calculated power in *Watt*, *MI*, *TIC* and I_{SPTA} in mW/cm^2.

3.3 In-Vitro Studies

Results of in-vitro studies performed either in one of the AIMS tanks or the customized acrylic chamber are presented in the following section. Furthermore, this includes measurements with the use of a PE Test Tube and transcranial experiments. Beside water for baseline acquisition, Br38 or SonoVue were used.

3.3.1 Transcranial Studies

3.3.1.a Transcranial Field Assessments

Figures 3.17, 3.18 and 3.19 show the impact of a skull on the acoustic field distribution. For each transducer, except 4.2, 5.1 and 5.1, the peak negative pressure loss was determined based on transcranial peak negative pressure measurements. The results are listed in Table 3.3.

1. Lateral-Posterior
2. Lateral-Superior
3. Lateral-Anterior

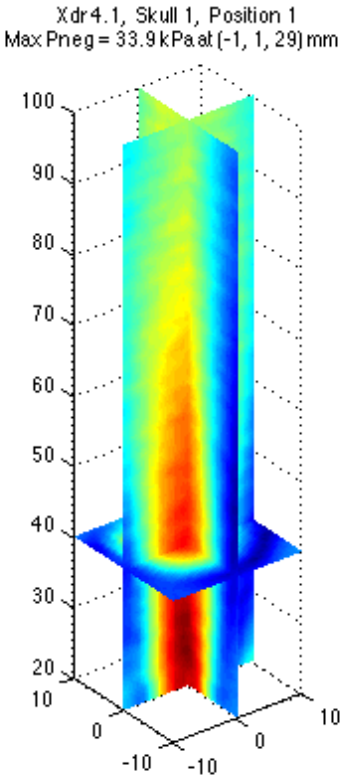

Figure 3.17: Lateral-Posterior (Position 1)

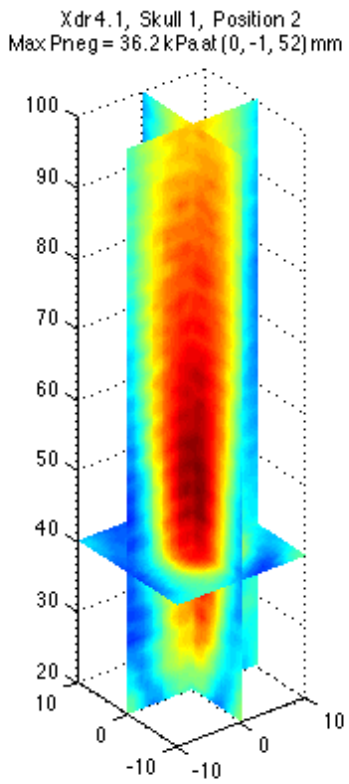

Figure 3.18: Lateral-Superior(Position 2)

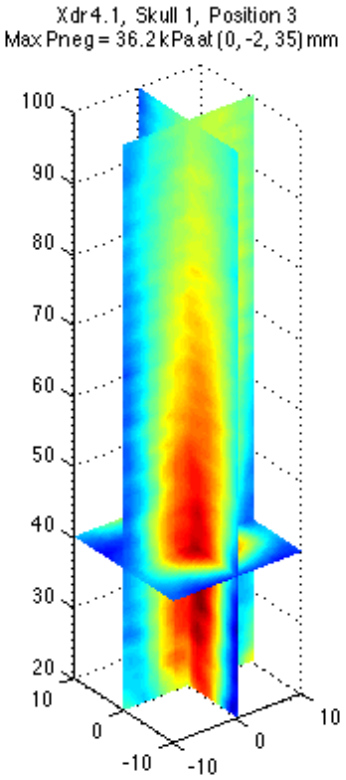

Figure 3.19: Lateral-Anterior(Position 3)

Table 3.3: Transcranial Field Assessments, PNP Loss

Xdr	Skull	Position	FF PNP Z40	Sk PNP Z40	% Loss PNP
2.1	1	1	47.2	22.1	53.2
2.1	1	2	47.2	22.2	53.0
2.1	2	1	47.2	21.5	54.4
2.1	2	2	47.2	25.6	45.8
2.1	2	3	47.2	26.4	44.1
2.1	3	1	47.2	31.8	32.6
2.1	3	2	47.2	22.7	51.9
2.1	3	3	47.2	30.3	35.8
2.2	1	1	43.0	20.4	52.6
2.2	1	2	43.0	25.6	40.5
2.2	1	3	43.0	24.1	44.0
2.2	2	1	43.0	19.8	54.0
2.2	2	2	43.0	22.2	48.4
2.2	2	3	43.0	21.8	49.3
2.2	3	1	43.0	21.3	50.5
2.2	3	2	43.0	21.5	50.0
2.2	3	3	43.0	26.0	39.5
2.3	1	1	37.9	20.0	47.2
2.3	1	2	37.9	23.9	36.9
2.3	1	3	37.9	20.2	46.7
2.3	2	1	37.9	22.1	41.7
2.3	2	2	37.9	23.8	37.2
2.3	2	3	37.9	25.7	32.2
2.3	3	1	37.9	24.7	34.8
2.3	3	2	37.9	24.9	34.3
2.3	3	3	37.9	28.7	24.3
3.1	1	1	62.8	32.2	48.7
3.1	1	2	62.8	33.6	46.5
3.1	1	3	62.8	33.7	46.3
3.1	2	1	62.8	30.2	51.9
3.1	2	2	62.8	27.0	57.0
3.1	2	3	62.8	25.2	59.9
3.1	3	1	62.8	36.3	42.2
3.1	3	2	62.8	32.0	49.0
3.1	3	3	62.8	45.0	28.3
4.1	1	1	60.2	28.8	52.2
4.1	1	2	60.2	35.6	40.9
4.1	1	3	60.2	31.3	48.0
4.1	2	1	60.2	26.8	55.5
4.1	2	2	60.2	27.6	54.2
4.1	2	3	60.2	31.5	47.7
4.1	3	1	60.2	37.6	37.5
4.1	3	2	60.2	34.5	42.7
4.1	3	3	60.2	37.1	38.4

3.3.1.b Skull Response Studies

Figures 3.20ff show the skull impact at certain distances between transducer 5.2 face and human temporal bone window. Two measurement sets were done first at 60 V_{PP} and furthermore repeated at 60, 180 and 360 V_{PP}. Distance between the transducer and the bone window were changed to 0, 5, 10, 20 and 30 mm. The driving signal was 20 cycles (i.e. 90.90 μs) long. The skull position relatively to the transducer was changed comparing all three datasets, as indicated by the terms Position 1 to 3. For Position 1 and 2, time parts from 15.18 μs with a length of 91.25 μs were examined. For Position 3 (i.e. dataset at different driving voltages), the considered time part was 17.95 μs, again with a length of 91.25 μs. The FFT graphs consist out of three subfigures which are the unprocessed time parts taken for the FFT (upper left), the time parts after a Blackman Harris window was applied (lower left) and the actual FFTs (main figures on the right).

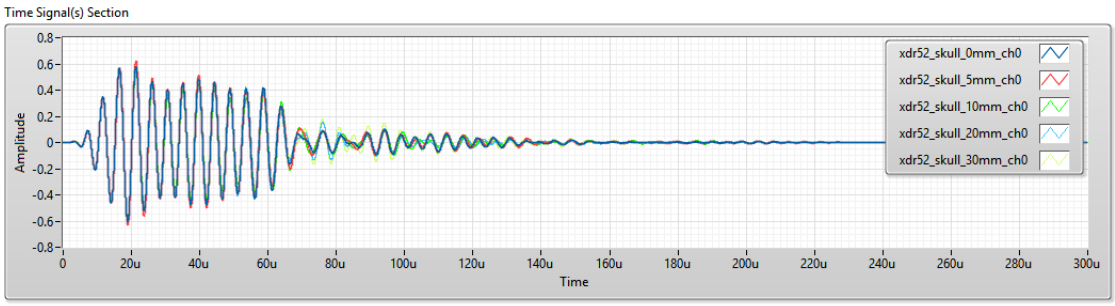

Figure 3.20: Overlay Time Signal at 0(blue), 5(red), 10(green), 20(lightblue), 30 mm(yellow) Distance between X52 and Temporal Bone Window, Position 1

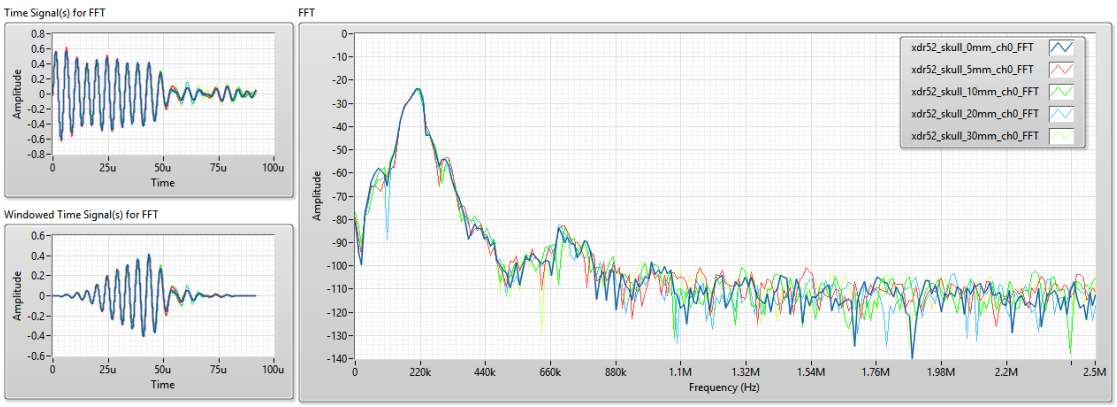

Figure 3.21: Overlay FFTs at 0(blue), 5(red), 10(green), 20(lightblue), 30 mm(yellow) Distance between X52 and Temporal Bone Window, Position 1

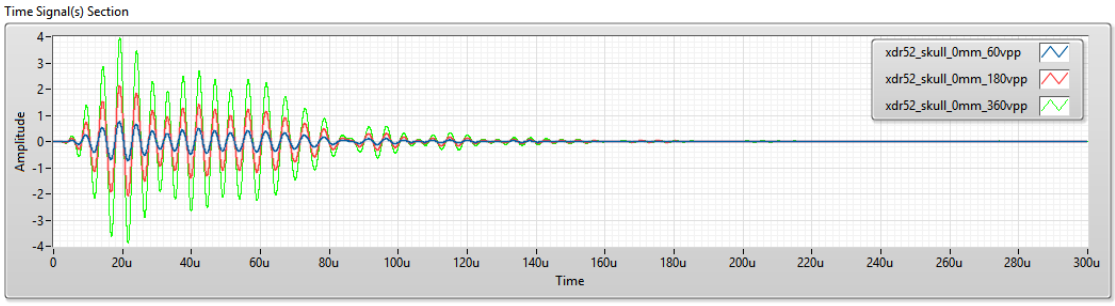

Figure 3.22: Skull Response, Time Signal, X52 to Skull Distance 0 mm, 60(blue)180(red)/360 V_{PP}(green)

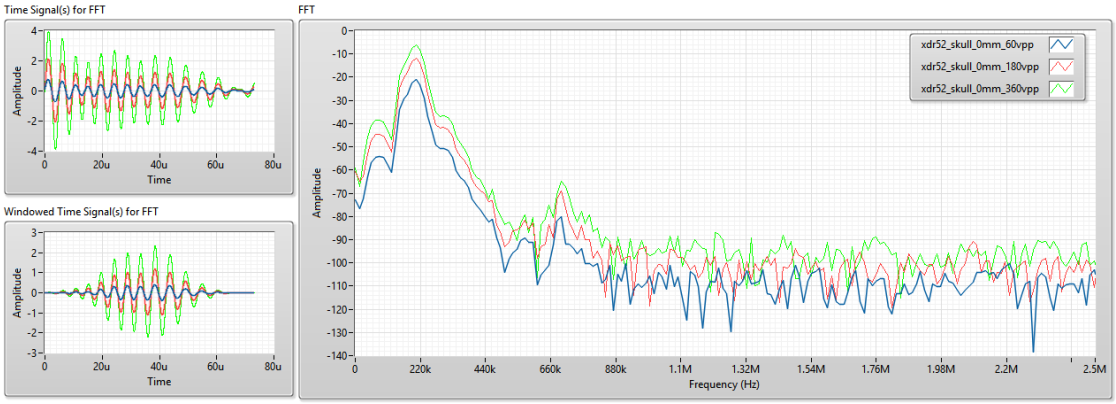

Figure 3.23: Skull Response, FFT, X52 to Skull Distance 0 mm, 60(blue)/180(red)/360 V_{PP}(green)

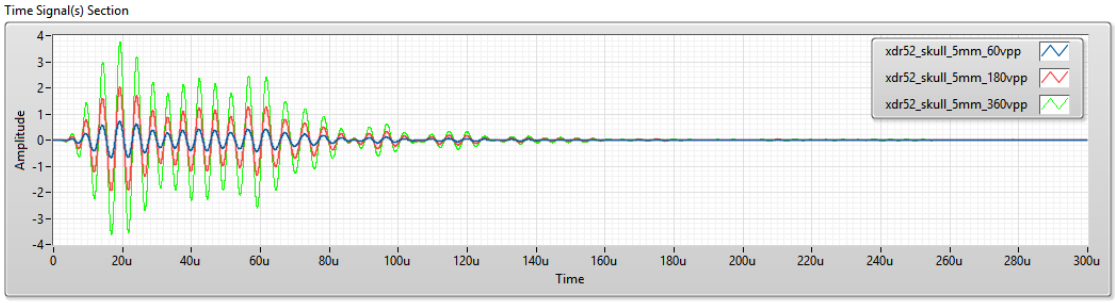

Figure 3.24: Skull Response, Time Signal, X52 to Skull Distance 5 mm, 60(blue)/180(red)/360 V_{PP}(green)

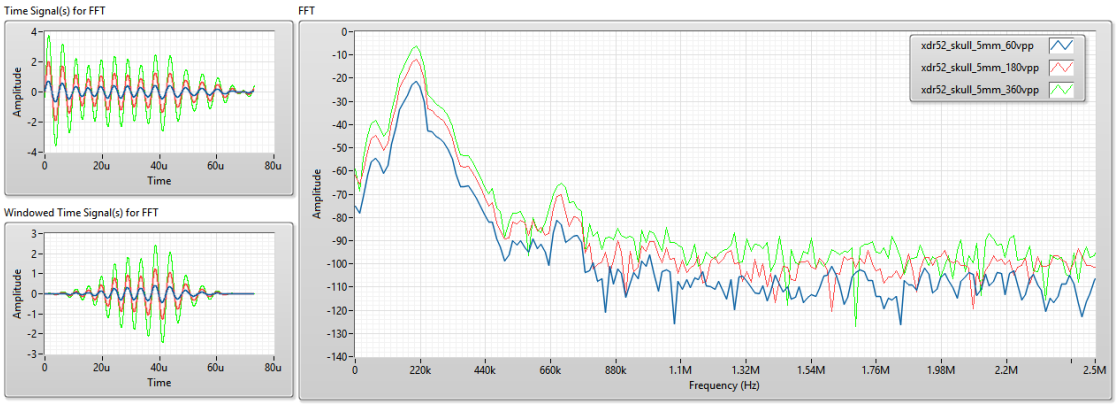

Figure 3.25: Skull Response, FFT, X52 to Skull Distance 5 mm, 60(blue)/180(red)/360 V_{PP}(green)

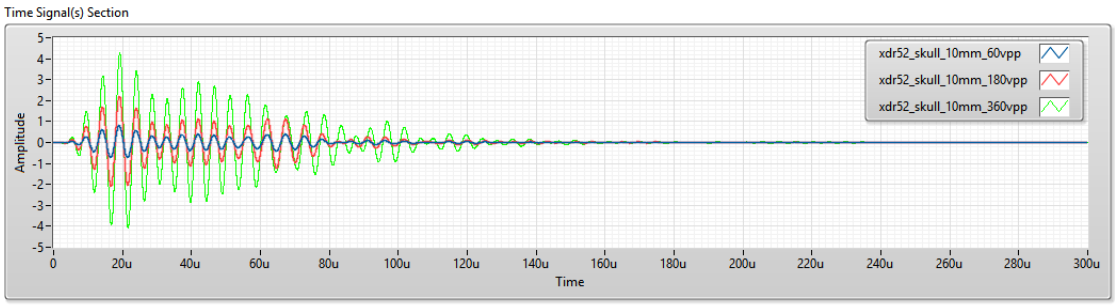

Figure 3.26: Skull Response, Time Signal, X52 to Skull Distance 10 mm, 60(blue)/180(red)/360 V_{PP}(green)

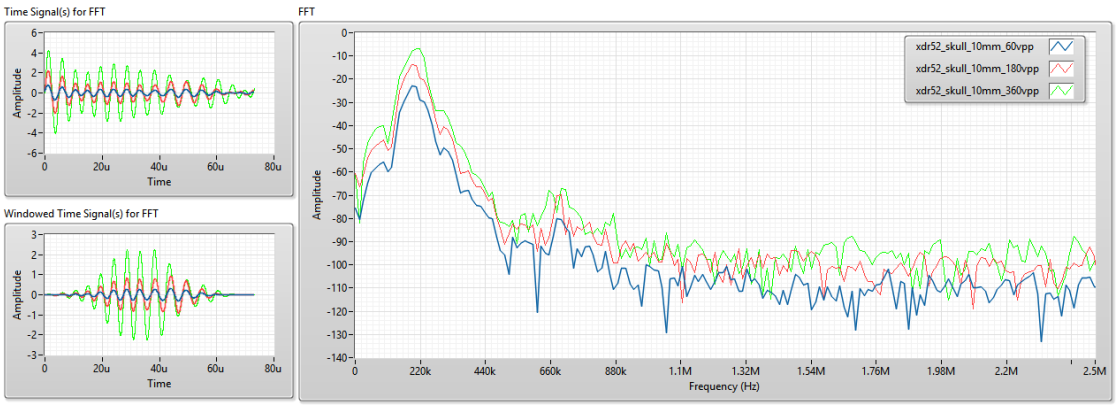

Figure 3.27: Skull Response, FFT, X52 to Skull Distance 10 mm, 60(blue)/180(red)/360 V_{PP}(green)

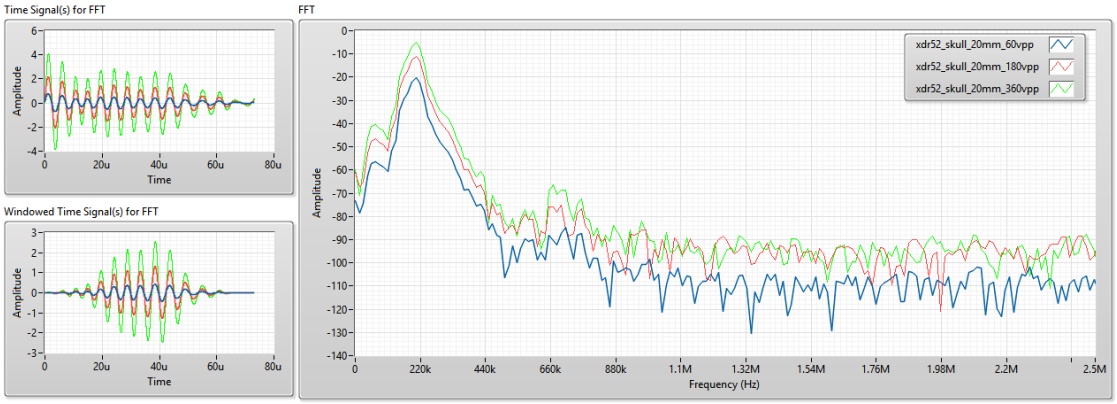

Figure 3.28: Skull Response, FFT, X52 to Skull Distance 20 mm, 60(blue)/180(red)/360 V_{PP}(green)

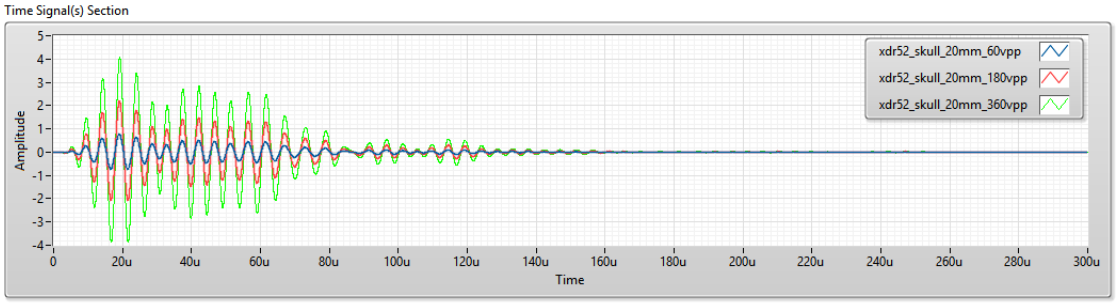

Figure 3.29: Skull Response, Time Signal, X52 to Skull Distance 20 mm, 60(blue)/180(red)/360 V_{PP}(green)

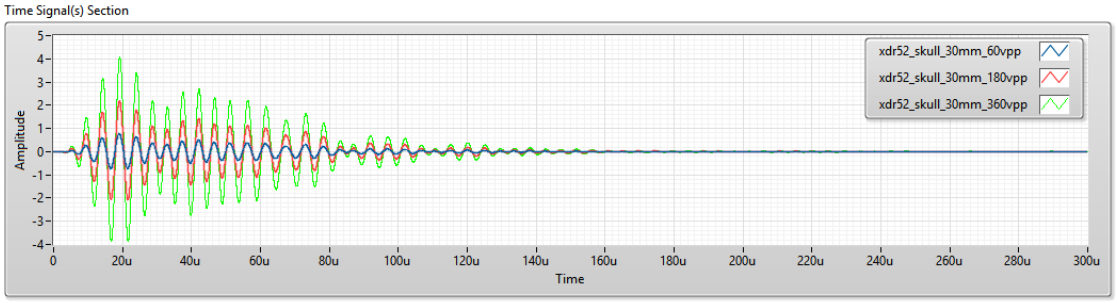

Figure 3.30: Skull Response, Time Signal, X52 to Skull Distance 30 mm, 60(blue)/180(red)/360 V_{PP}(green)

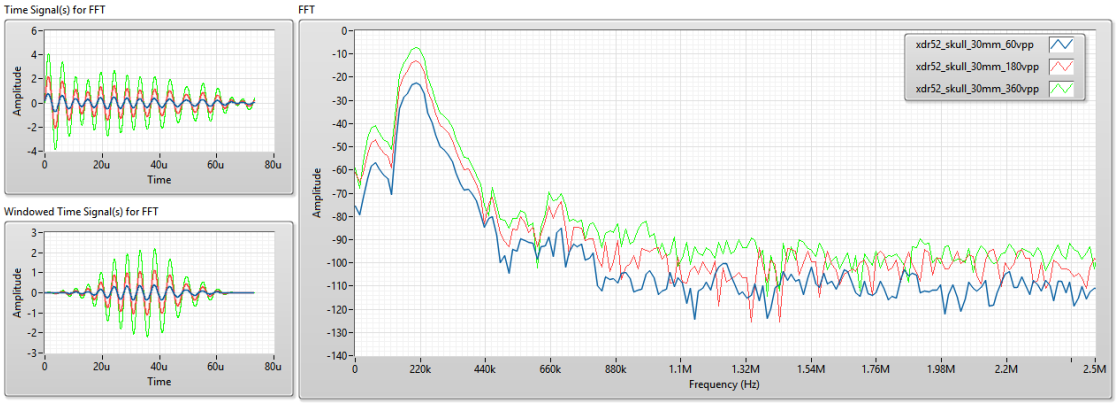

Figure 3.31: Skull Response, FFT, X52 to Skull Distance 30 mm, 60(blue)/180(red)/360 V_{PP}(green)

3.3.2 Microbubble Response Studies in AIMS tank

Prior to migrating the setup to the acrylic chamber for purpose of acoustic response measurements, a large amount of data has been acquired with the PE test tube positioned in a transducers focal zone. In the following only one generic result is presented to demonstrate the outcome of this specific experimental setup.

Measurements were performed with transducer 4.1 at driving voltages of 96, 120 and 144 V_{PP}. Pulses of 5 ms width were transmitted each second (i.e. 0.5 % duty cycle). The receive chain included an analog Notch and Lowpass Filter combination prior to the ADC. In this experimental setup, after recording a baseline (i.e. without microbubbles) datasets with microbubbles were acquired. As microbubbles we used in this case 0.25 ml of SonoVue immersed into a beaker of 1 l deionized water. The flow pump was set to generate a flow of 10 ml/min. In post-processing with LabVIEW data was prepared to generate Figures 3.32, 3.33 and 3.34 that show microbubble data superimposed on a baseline.

In addition to FFT analysis, the Gabor transform is used to determine the sinusoidal frequency content of the received signals. Figures 3.35 and 3.36 represent the Gabor transform of an arbitrarily chosen signal out of the one hundred 5 ms signals received per medium condition(i.e. with or without Microbubbles) at a transducer driving voltage of 144 V_{PP}. The settings of the Gabor Transform were selected to achieve a high frequency resolution. This included the application of a Hanning Window, a Window length of 4096 points and window shifting increments of 8 points.

Figure 3.35 (i.e. baseline) shows a maximum of 4.03mV_{rms}, whereas it indicates 5.41mV_{rms} in case microbubbles are present.

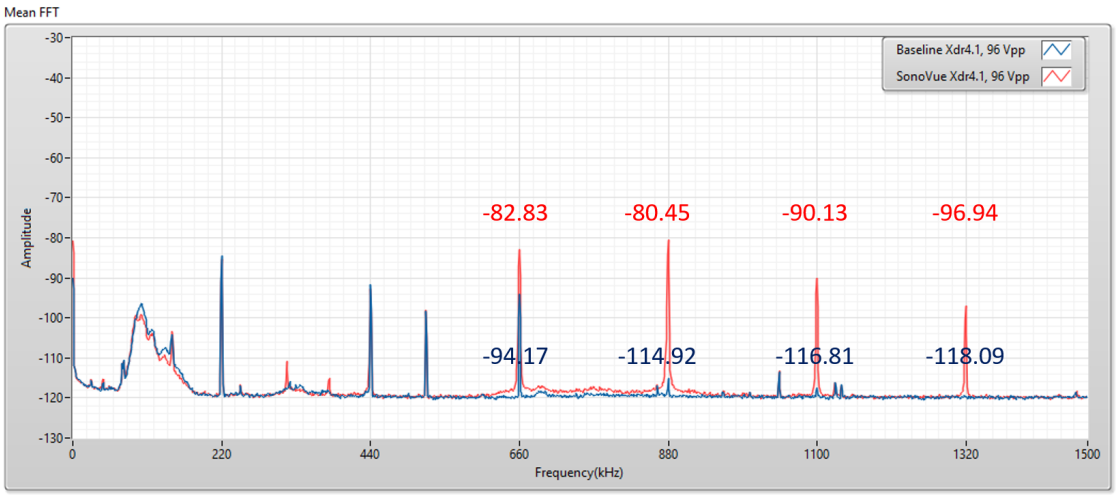

Figure 3.32: FFT Overlay of Baseline(blue) and SonoVue(red) Dataset, Xdr 4.1, Driving Voltage 96 V_{PP}

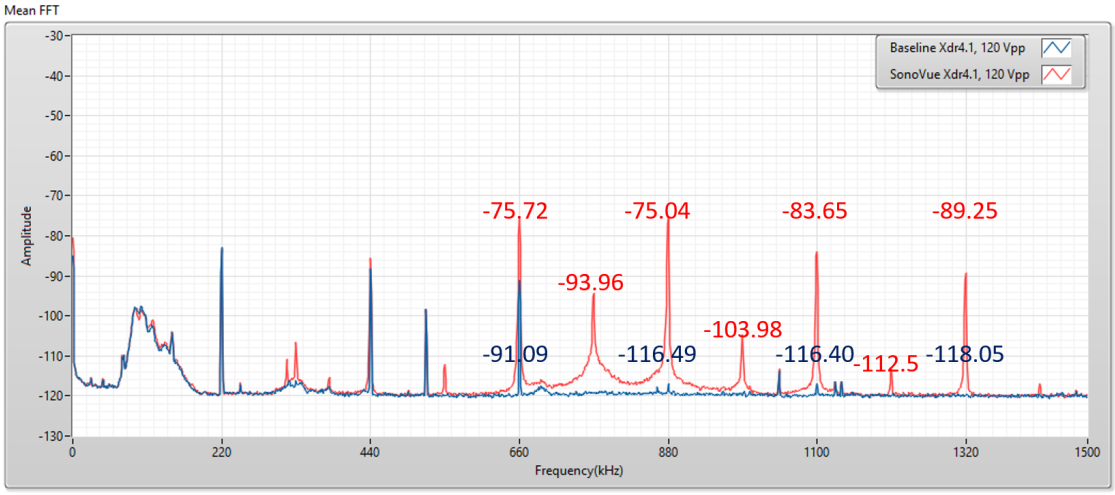

Figure 3.33: FFT Overlay of Baseline(blue) and SonoVue(red) Dataset, Xdr 4.1, Driving Voltage 120 V_{PP}

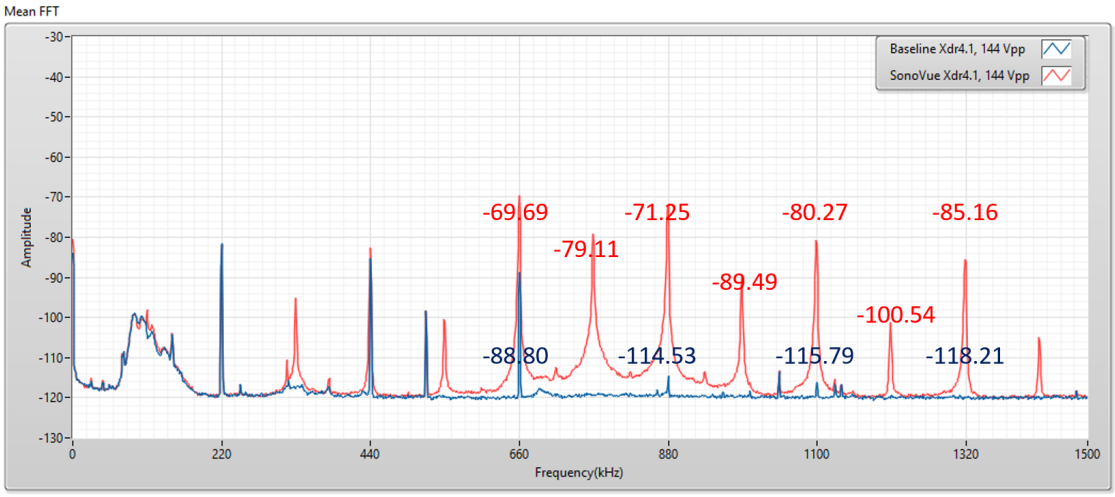

Figure 3.34: FFT Overlay of Baseline(blue) and SonoVue(red) Dataset, Xdr 4.1, Driving Voltage 144 V_{PP}

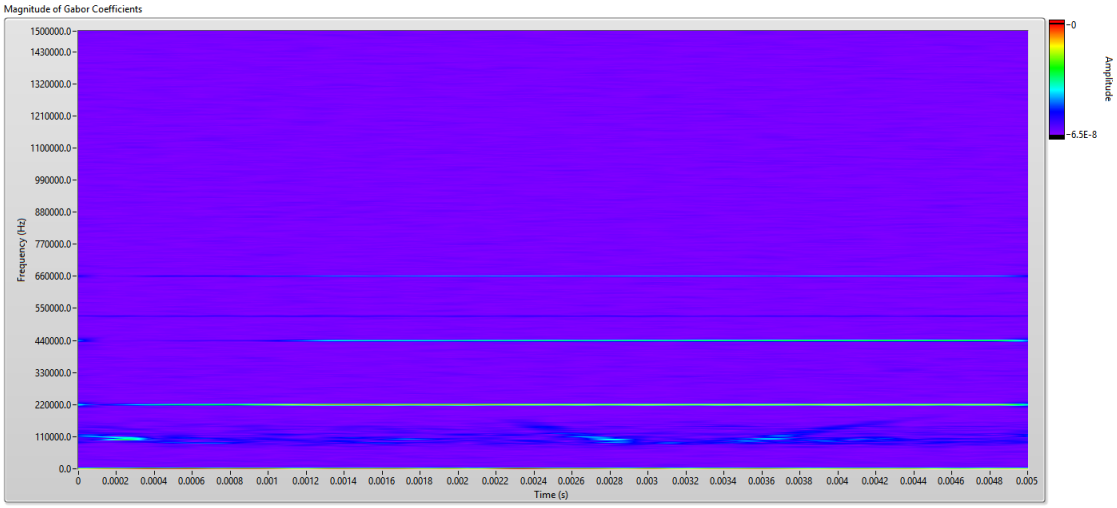

Figure 3.35: Gabor Transform of Baseline Dataset, Xdr4.1, Driving Voltage 144 V_{PP}

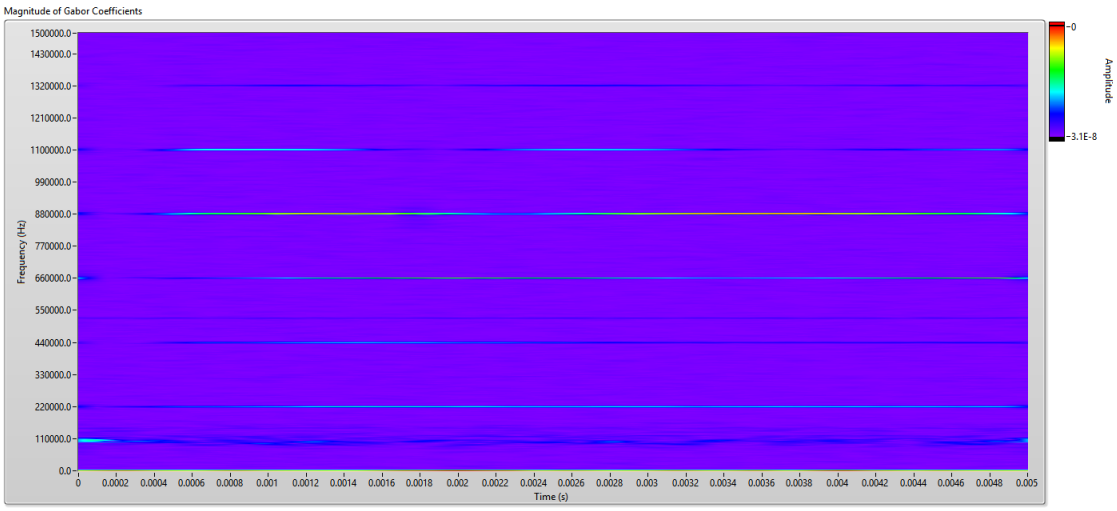

Figure 3.36: Gabor Transform of SonoVue Dataset, Xdr4.1, Driving Voltage 144 V_{PP}

3.3.3 Microbubble Response Studies in Acrylic Chamber

3.3.3.a Impact of Transducer driving Voltage on Microbubble Response

Results are shown for experiments with transducer 5.2 that was fully immersed into the acrylic chamber, initially filled with 2.5 l of degassed water (i.e. baseline dataset). Later, either 0.6 ml Br38 or 0.6 ml SonoVue were added to create a bubbly liquid. Between the two measurements the chamber was cleaned and refilled. Figures 3.37 through 3.42 are examples for a 880, 1100 and 1320 kHz tuned matched filter and a transducer driving voltage of 30 V_{PP}. Experiments were then repeated at 60, 90 and 120 V_{PP}. Results for baseline conditions are colored blue, whereas if microbubbles are added, red. Indicated in green is the Nyman-Pearson detection threshold. Expressed in Table 3.4 are the absolute values of detected microbubble signals above detection threshold, in comparison Br38 to SonoVue.

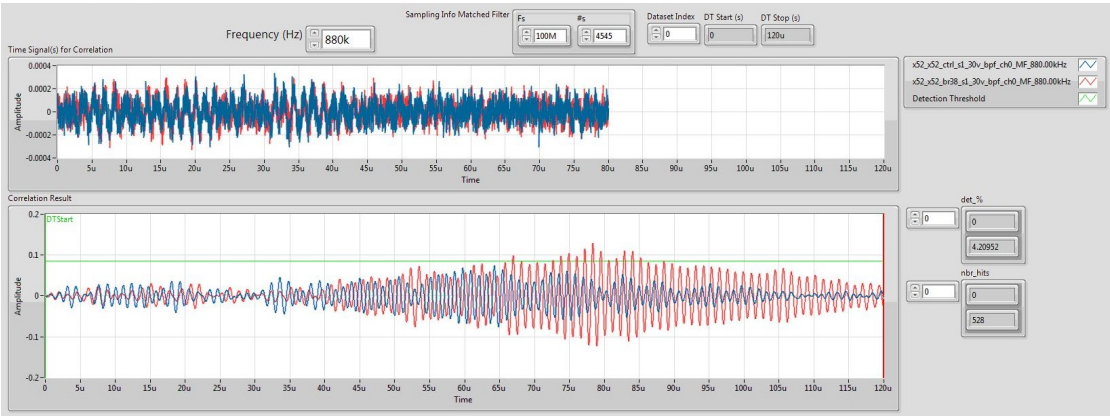

Figure 3.37: 880 kHz Matched Filter, Baseline and Br38 at 30 V_{PP} input voltage

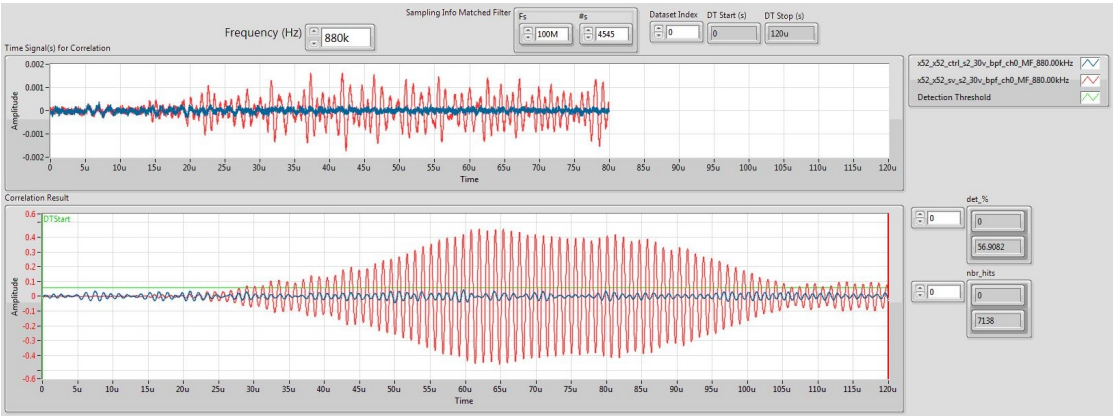

Figure 3.38: 880 kHz Matched Filter, Baseline and SonoVue at 30 V_{PP} input voltage

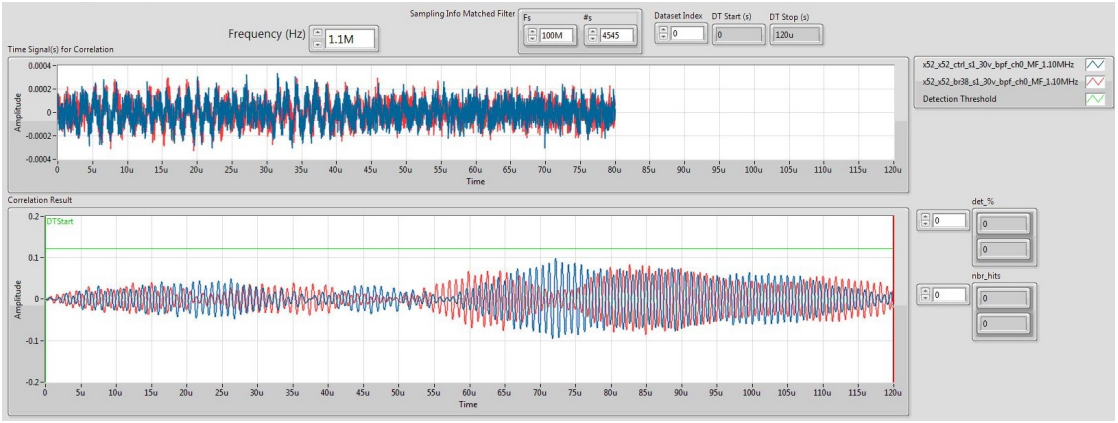

Figure 3.39: 1100 kHz Matched Filter, Baseline and Br38 at 30 V_{PP} input voltage

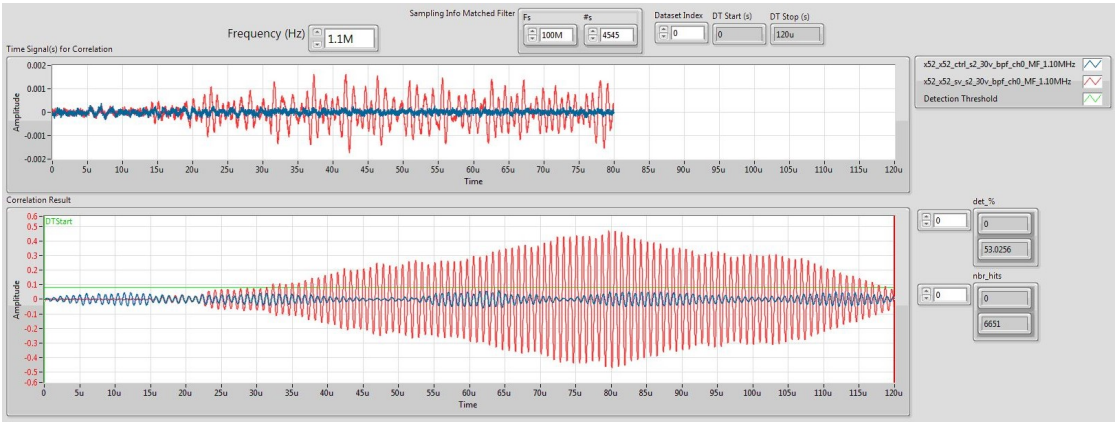

Figure 3.40: 1100 kHz Matched Filter, Baseline and SonoVue at 30 V_{PP} input voltage

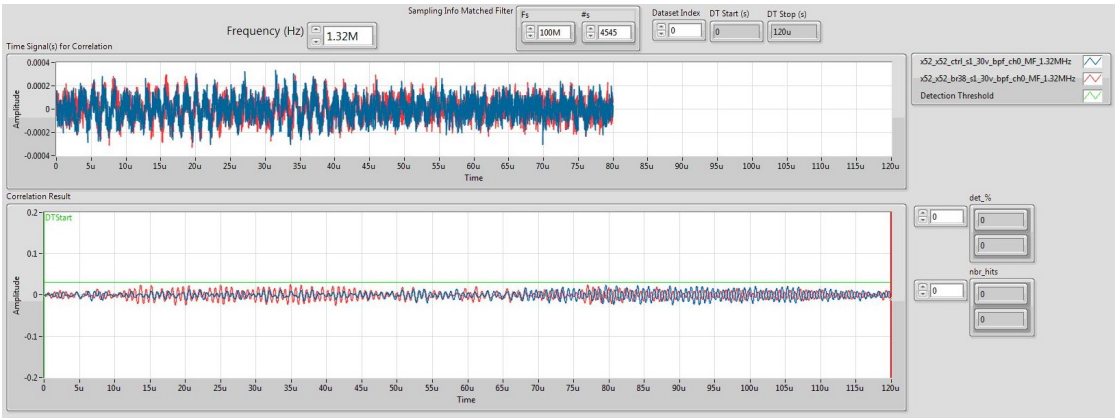

Figure 3.41: 1320 kHz Matched Filter, Baseline and Br38 at 30 V_{PP} input voltage

Figure 3.42: 1320 kHz Matched Filter, Baseline and SonoVue at 30 V_{PP} input voltage

Table 3.4: Impact of Driving Voltage on Microbubble Response

	30 V_{PP}		60 V_{PP}		90 V_{PP}		120 V_{PP}	
	Br38	SonoVue	Br38	SonoVue	Br38	SonoVue	Br38	SonoVue
770 kHz	- -	- -	- -	-	- -	- -	- -	- -
880 kHz	528 4.2%	7138 56.9%	129 1.0%	4338 34.5%	- -	5258 41.9%	2286 18.2%	- -
990 kHz	115 0.9%	- -	- -	317 2.5%	42 0.3%	72 0.6%	- -	56 0.4 %
1100 kHz	- -	6651 53.0%	126 1%	7121 56.7%	1168 9.3%	3427 27.3%	- -	- -
1210 kHz	202 1.6%	3581 28.5%	24 0.2%	665 5.3%	130 1.0%	907 7.2%	18 0.1%	1682 13.4%
1320 kHz	- -	5354 42.6%	17 0.1%	4877 38.9%	267 2.1%	2661 21.2%	44 0.35%	361 2.9%

3.3.3.b Microbubble Dose Escalation Studies

Similar to the previous, Table 3.5 lists the absolute values of detected microbubble signals above detection threshold, in comparison Br38 to SonoVue for various microbubble concentrations of 0.2 ml, 0.6 ml, 1.25 ml, 4.5 ml injected into 2.5 l degassed water.

Table 3.5: Microbubble Dose Escalation

	0.2 ml		0.6 ml		1.25 ml		4.5 ml	
	Br38	SonoVue	Br38	SonoVue	Br38	SonoVue	Br38	SonoVue
770 kHz	-	465	-	-	-	-	-	-
	-	3.7%	-	-	-	-	-	-
880 kHz	1964	496	129	4338	-	2677	21	2475
	15.7%	4.0%	1.0%	34.6%	-	21.3%	0.2%	19.7%
990 kHz	46	2430	-	317	-	471	19	622
	0.4%	19.4%	-	2.5%	-	3.8%	0.2%	5.0%
1100 kHz	1341	4083	126	7121	4817	5432	2769	2790
	10.7%	32.5%	1.0%	56.8%	38.4%	43.3%	22.1%	22.2%
1210 kHz	116	5690	24	665	46	1295	129	263
	0.9%	45.4%	0.2%	5.3%	0.4%	10.3%	1.0%	2.1%
1320 kHz	-	-	17	4877	1632	4092	3477	3645
	-	-	0.14%	38.9%	13.0%	32.6%	27.7%	29.1%

3.3.3.c Measurements through Acrylic Chamber Wall

In this experiment, transducer 5.2 is positioned outside of the acrylic chamber, 2 mm away with its face from the broadside acrylic wall. The box was filled with 2.5 l degassed water for baseline acquisition. 0.6 ml Br38 or Sonovue were injected to examine microbubble response from the inside of the box. Table 3.6 shows the absolute values of detected microbubble signals above detection threshold, in comparison Br38 to SonoVue.

Table 3.6: Measurements through Acrylic Chamber Wall

	30 V_{PP}		60 V_{PP}		90 V_{PP}		120 V_{PP}	
	Br38	SonoVue	Br38	SonoVue	Br38	SonoVue	Br38	SonoVue
770 kHz	-	-	-	-	-	-	-	-
	-	-	-	-	-	-	-	-
880 kHz	-	1025	11	1696	291	1642	254	2729
	-	8.2%	0.1%	13.5%	2.3%	13.1%	2.1%	21.8%
990 kHz	-	-	-	-	-	-	-	-
	-	-	-	-	-	-	-	-
1100 kHz	162	6764	256	4862	489	2737	4503	4019
	1.3%	53.9%	2.0%	38.8%	3.9%	21.8%	35.9%	32.0%
1210 kHz	8	3715	-	7177	10	3084	1200	566
	0.1%	29.6%	-	57.2%	0.1%	24.6%	9.6%	4.5%
1320 kHz	25	5777	-	7932	803	2335	3738	3828
	0.2%	46.1%	-	63.2%	6.4%	18.6%	29.8%	30.5%

3.4 Animal Safety Studies

In the following the outcome of the safety studies on rabbits, performed in Cedars Sinai, are shown.

3.4.1 Ultrasound Parameters

At the highest driving voltage (i.e. 60 V_{PP}) transducer 5.1 delivers a maximum peak negative pressure of 220 kPa in water. According to equation 1.1, intensity equals 120 mW/cm^2. Furthermore, considering the low duty cycle (i.e. 45.45 μs pulse width at a PRT of 100 ms), I_{SPTA} turns out to be 0.054 mW/cm^2. For animal studies, where transducer 4.1 was used and the duty cycle was significantly higher, we calculated an I_{SPTA} of 15 mW/cm^2.

3.4.2 Animal Safety and Survival Analysis

Table 3.7 indicates the survival rate of the rabbits. Note, that two fatalities are caused by either isoflurane application(*) in the one case, and by a severe stroke(**) in the other.

Table 3.7: Safety and Survival Analysis

Treatment Group	Parenchymal Hemorrhage	Hemorrhagic Infarction	Punctate Hemorrhage	Survival Rate
Normal + US/MB	0/12	0/12	0/12	11/12*
Embolized + US/MB	0/12	0/12	0/12	10/12**

3.4.3 Behavioral Assessment

According to the procedure explained in 2.9, table 3.8 shows the Behavioral Assessment Score.

Table 3.8: Behavioral Analysis

Treatment Group	Behavioral Score (Pre-US-MB)	Behavioral Score (Post-US-MB)
Normal + US/MB	0	0
Embolized + US/MB	24.58 $\pm$ 5.27	22.08 $\pm$ 8.19

3.5 Human Cadaver Studies

Figures 3.43 to 3.49 show the results of studies on the first cadaver head. Each graph represents the FFT of a received time signal trimmed to 0 to 95 μs. Five of these FFTs are overlaid in a single plot (center right). The none-windowed time parts (upper left) as well as the windowed time part show the input signals for the FFTs. Voltages 5 to 50 V_{PP} indicate the voltage at which the transducer was driven at. Furthermore, results are shown for acquisition with and without analog bandpass filter and at for four different transducer positions with respect to the temporal bone window.

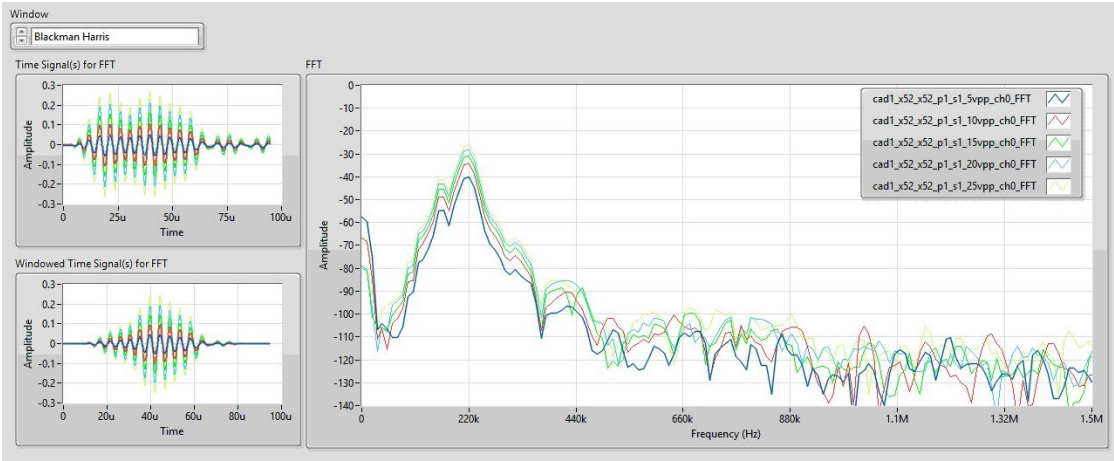

Figure 3.43: Cadaver Head 1, Xdr 5.2, 5 to 25 V_{PP}(blue,red,green,lightblue,yellow respectively), Position 1, FFT, without analog Filter

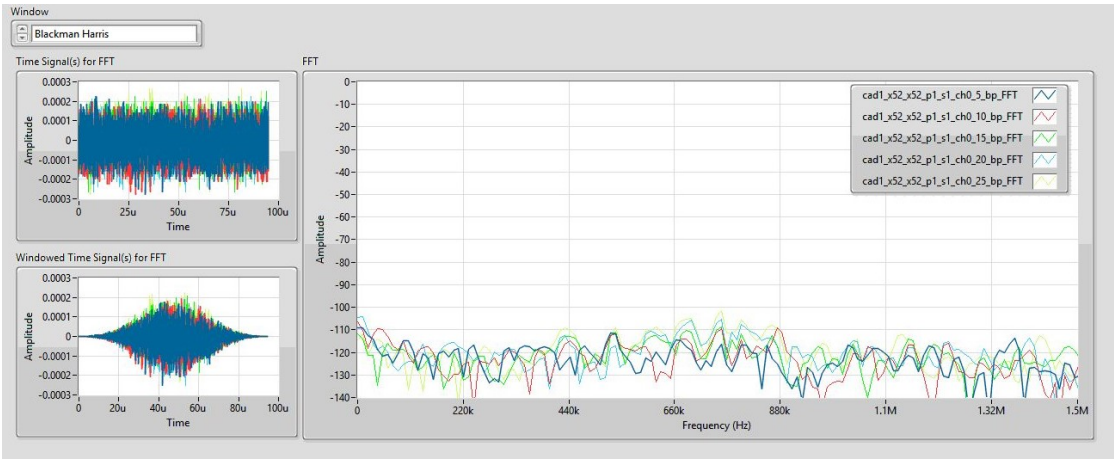

Figure 3.44: Cadaver Head 1, Xdr 5.2, 5 to 25 V_{PP}(blue,red,green,lightblue,yellow respectively), Position 1, FFT, with analog Bandpass Filter

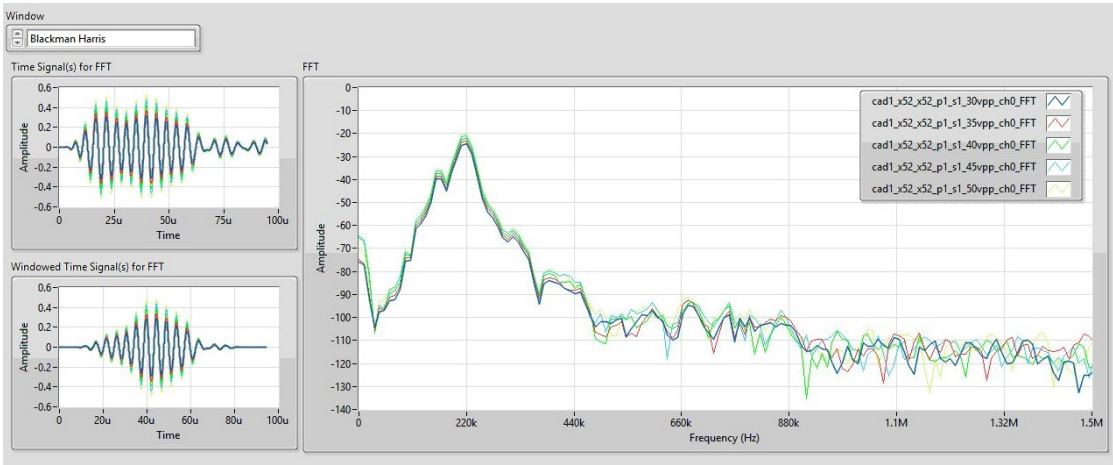

Figure 3.45: Cadaver Head 1, Xdr 5.2, 30 to 50 V_{PP}(blue,red,green,lightblue,yellow respectively), Position 1, FFT, without analog Filter

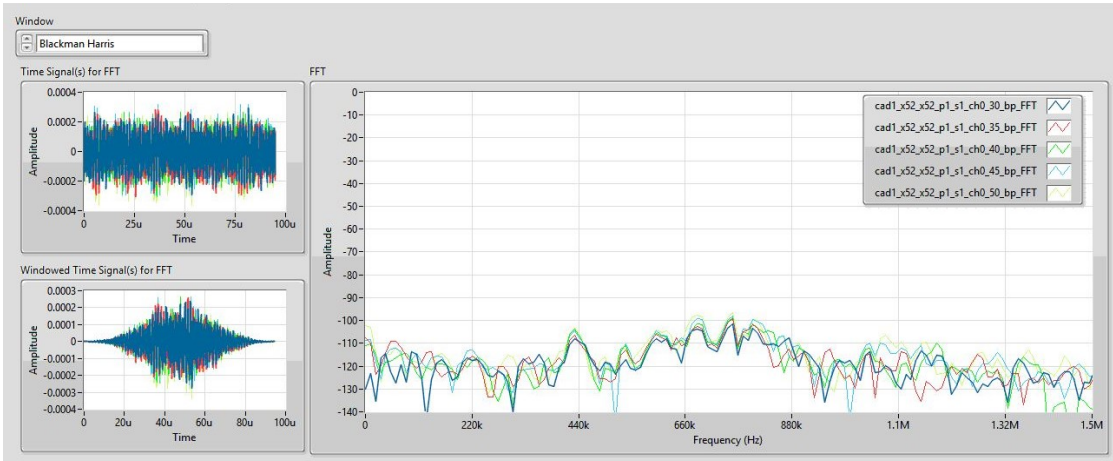

Figure 3.46: Cadaver Head 1, Xdr 5.2, 30 to 50 V_{PP}(blue,red,green,lightblue,yellow respectively), Position 1, FFT, with analog Bandpass Filter

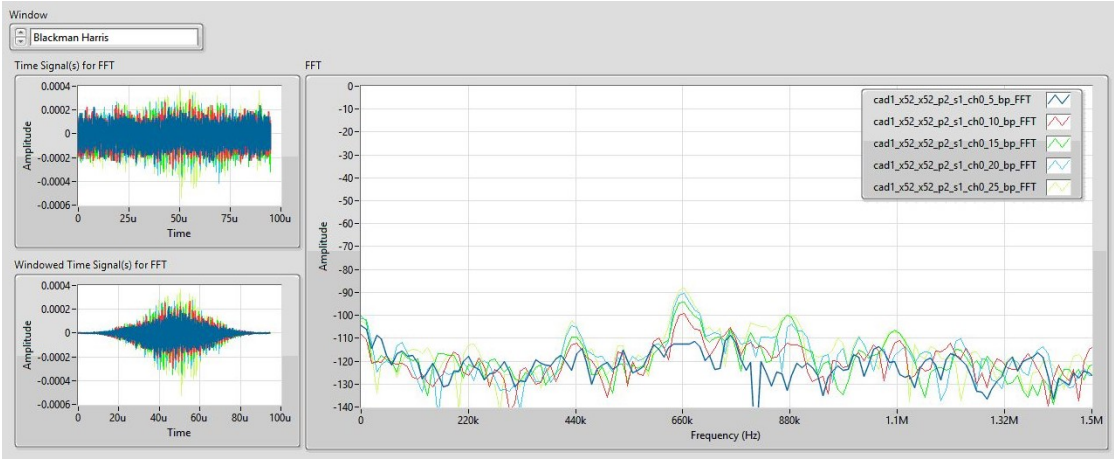

Figure 3.47: Cadaver Head 1, Xdr 5.2, 5 to 25 V_{PP}(blue,red,green,lightblue,yellow respectively), Position 2, FFT, with analog Bandpass Filter

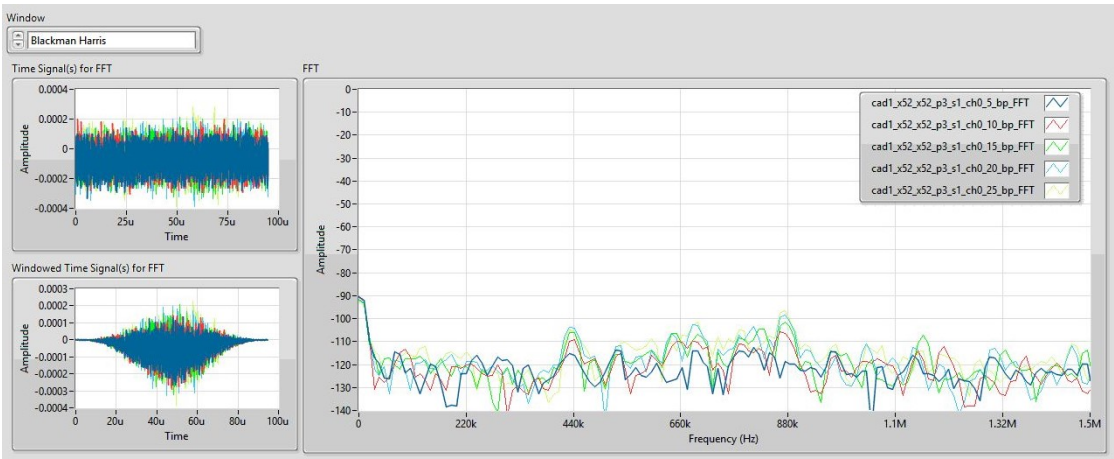

Figure 3.48: Cadaver Head 1, Xdr 5.2, 5 to 25 V_{PP}(blue,red,green,lightblue,yellow respectively), Position 3, FFT, with analog Bandpass Filter

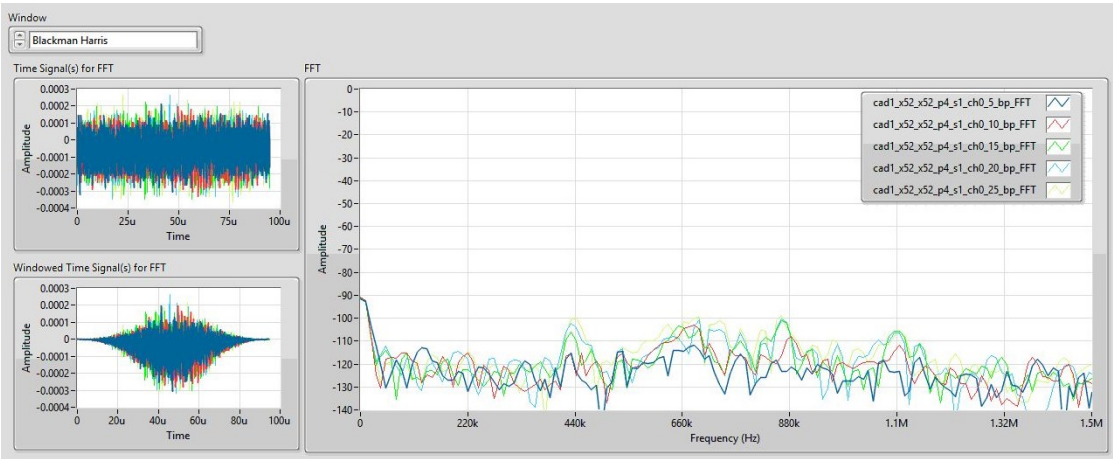

Figure 3.49: Cadaver Head 1, Xdr 5.2, 5 to 25 V_{PP}(blue,red,green,lightblue,yellow respectively), Position 4, FFT, with analog Bandpass Filter

Using the identical settings for post processing and data preparation as for the received signals from the first cadaver head, Figures 3.50 and 3.51 are the results of the second cadaver head.

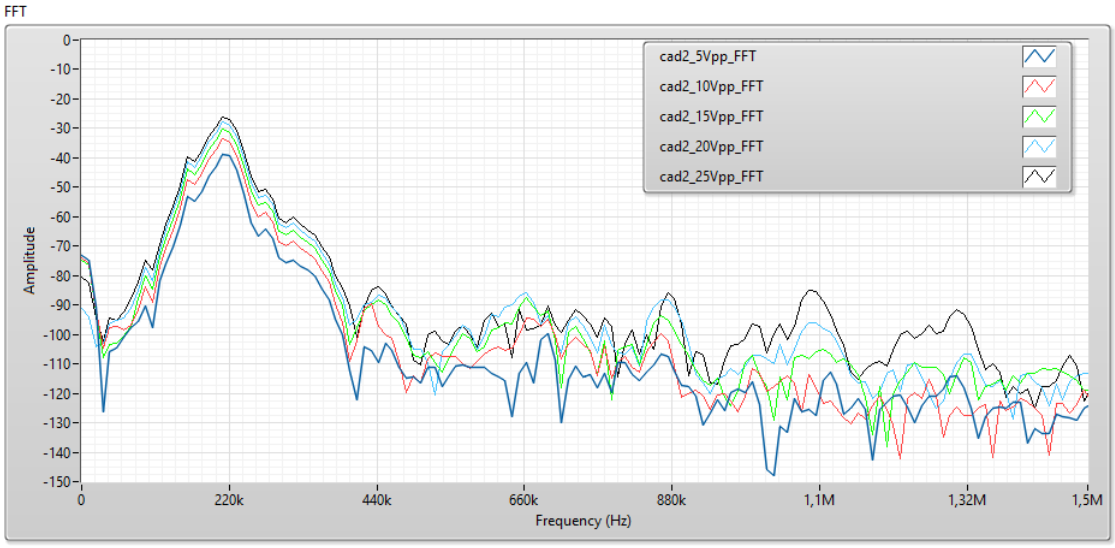

Figure 3.50: Cadaver Head 2, Xdr 5.2, 5 to 25 V_{PP}(blue,red,green,lightblue,yellow respectively), FFT, without analog Bandpass Filter

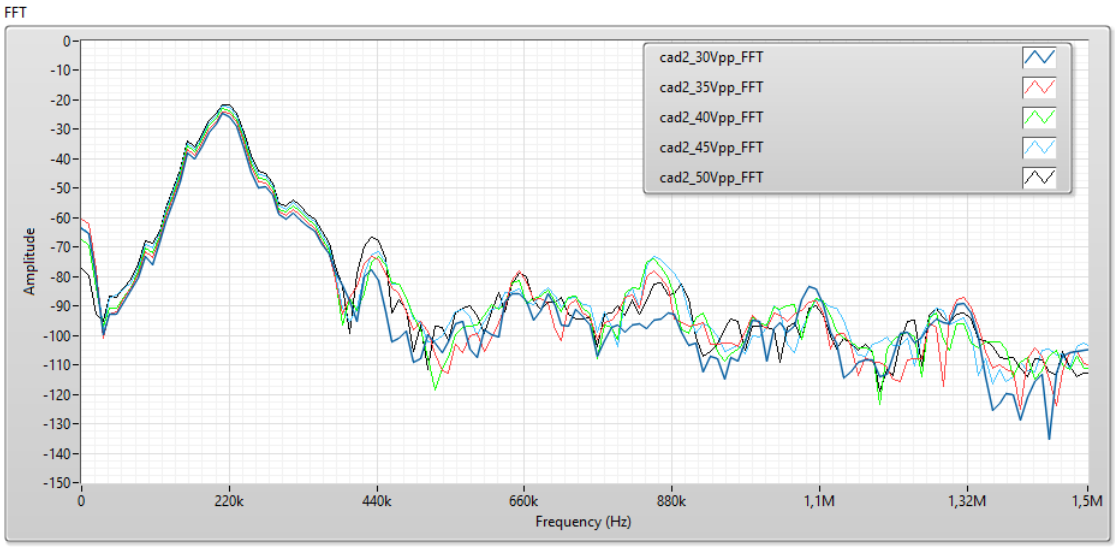

Figure 3.51: Cadaver Head 2, Xdr 5.2, 30 to 50 V_{PP}(blue,red,green,lightblue,yellow respectively), FFT, without analog Bandpass Filter

To generate Figures 3.54 and 3.55 pulse inversion was applied in the post processing.

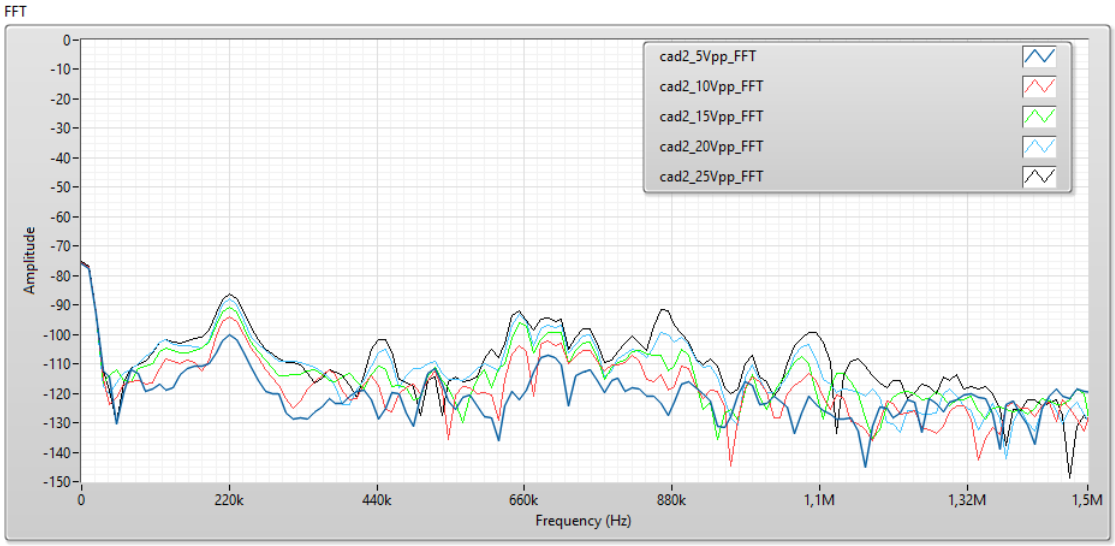

Figure 3.52: Cadaver Head 2, Xdr 5.2, 5 to 25 V_{PP}(blue,red,green,lightblue,yellow respectively), FFT, with analog Bandpass Filter

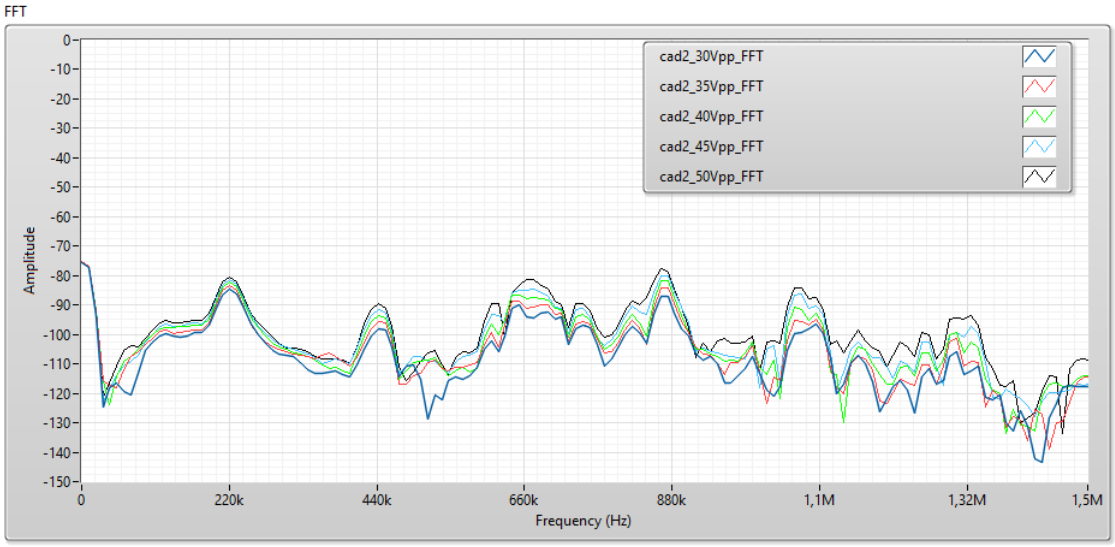

Figure 3.53: Cadaver Head 2, Xdr 5.2, 30 to 50 V_{PP}(blue,red,green,lightblue,yellow respectively), FFT, with analog Bandpass Filter

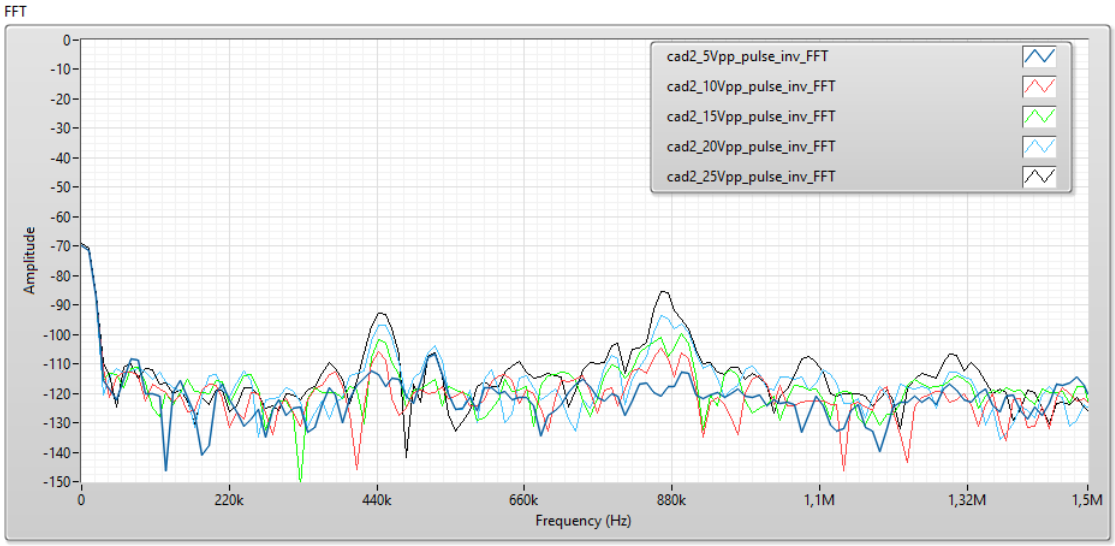

Figure 3.54: Cadaver Head 2, Xdr 5.2, 5 to 25 V_{PP}(blue,red,green,lightblue,yellow respectively), FFT, with analog Bandpass Filter, with Pulse Inversion

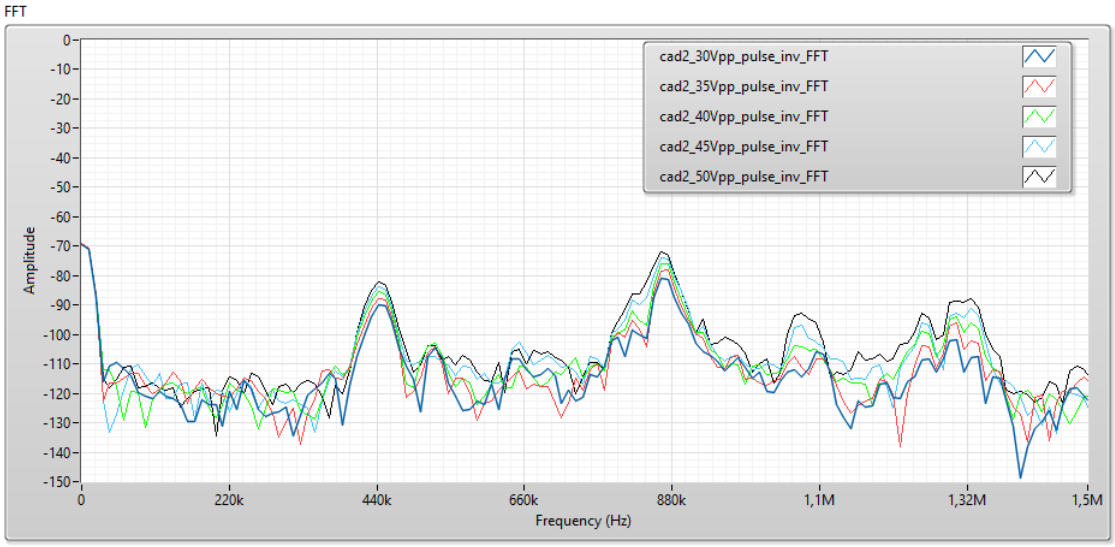

Figure 3.55: Cadaver Head 2, Xdr 5.2, 30 to 50 V_{PP}(blue,red,green,lightblue,yellow respectively), FFT, with analog Bandpass Filter, with Pulse Inversion

CHAPTER 4

Discussion and Conclusion

4.1 Transducers

Variations in the localization of the focal zone, differences in delivered peak negative pressure, in efficiency and sensitivity amongst our versions are present even if they belong to the same generation. This is due to the complex manufacturing process and the variance in material properties.

4.1.1 Impedance Measurements

From the transducer equivalent circuit 1.4 we know that at resonance inductance L_s and capacitance C_s are equally in magnitude, but of opposite phase. At resonance the phase angle θ is ideally 0, because L_s and C_s cancel each other out. The results of the impedance measurements 3.1.1 indicate that this is the case, as the θ approaches 0 at 220 kHz for transducers 5.1 and 5.2. on the transmission side and around 1 MHz at the receiver side. Oftentimes, broken wires, for example, led to substantial impedance differences between transducers, which shows that the impedance measurements are not only necessary to characterize transducers, they furthermore represent a valuable sanity check.

4.1.2 Acoustic Field Properties

The Acoustic Intensity Measurement System used in the facilities, was ideal to measure acoustic parameters such as intensity, peak positive and peak negative pressure. However, within the underlying research activities peak negative pressure was measured only. The reason why we examined peak negative pressue only was that most of the effects (such as cavitation) that are of relevance in our case are linked to peak negative pressure rather than to peak positive pressure.

Transmission The transmitting elements, in general, produce a fairly uniform field with most of the energy around the axis, despite being a ring element. Again, acoustic differences are

present, amongst all generations, even within generations. However, especially in the case of the 4th and 5th generations, we demanded a high degree of similarity, which the manufacturer tried to accomplish. Essentially, as seen in 3.1.2 Xdr 4.1 and Xdr 4.2, both transducers reach their maximum PNP at almost the same distance (i.e. Xdr 4.1 at 29 mm and Xdr 4.2 at 30 mm). Furthermore, the maximum PNP of 64 kPa in case of Xdr 4.1 and 57 kPa for Xdr 4.2, are reasonable small differences. The 3D geometry of the acoustic field for Xdr 5.1 is similar to Xdr 4.1 and 4.2, with a maximum of 52 kPa at a distance of 36 mm. In the case of Xdr 5.2 results are very similar to Xdr 5.1, with a maximum of 55 kPa at a distance of 30 mm. Compared to the 2nd and 3rd generations, the 4th and the 5th significantly improved the transmission efficiency, because of the increased dicing depth (e.g. Xdr 2.3 PNP_{max} = 35 kPa).

Reception Initially, it was noted that he receive sensitivity of a disc style transducer varies with distance. Hence, in order to have complete characterization of our transducers, sensitivity measurements of the PCD elements must be included. Ultimately, we established a good characterization method that takes into account the disc shape of the receiving element. However, results from the actual 14 mm disc were only loosely correlated to the 14 mm circular samples from the hydrophone. It was suggested that this may be because the hydrophone has the same sensitivity at every point on the 14 mm circle, whereas the 14 mm disc in the transducer has different sensitivity over the surface, depending on whether the energy is in the center or toward the edges. Therefore, slices of data were examined (i.e. sets of samples captured by the hydrophone over the 14 mm area) confirming that when the energy is dispersed toward the edges, the output of the transducer is lower then when the energy is concentrated more toward the center. Considering this effect, the deviations between expected sensitivity and actual voltage measurements were explained. Sensitivity measurements, in general, indicate that the 220 kHz suppression specification was not met with the new PZT material. The suppression relative to the 880 kHz component, for instance, turned out to be −17 dB. On the other side, measurements indicated a sensitivity of 263.8 μV_{PP}/Pa for X51 and of 255.4 μV_{PP}/Pa for X52 at 220 kHz. Compared to X41 with 12.3 μV_{PP}/Pa this was considered to be an extremely satisfying result. It is noteworthy, considering the almost identical transmission performance of the two generations, that although both transducers are excited with almost the same voltage (70 V_{PP} / 71.6 V_{PP}), the PCD element of transducer 4.2 receives about 90% less signal as indicated in Figure 3.15.

4.1.3 Time and Frequency Domain Analysis

Results in 3.1.3 show the characteristic behavior of our transducers. Since both elements, i.e. the transmitter and receiver, are active simultaneously, the results shown are electrical signals of the transmit picked up by the receiver (i.e. electrical/mechanical cross talk). Figure 3.13 demonstrates the sequence of transducer ring-up, stable state and ring-down. As the wave propagates through degassed water and there are no scatterer or reflecting objects in propagation direction (except the wall at about 16 cm distance), in the time domain we would expect nothing else than a sequence of convolution of the transfer and receiver function within the first 0 to 100 μs. In fact, this is the case from 0 to 140 μs. Beyond that time, the transducer stops oscillating, hence only noise is present. In Figure 3.12 the echo from the opposite chamber wall at 218 μs is re-

ceived by the PCD element. Comparing the signals received with transducer 4.2 and 5.1 (Figure 3.15), the difference in sensitivity becomes obvious. The amplitude of the received signals with transducer 5.1 (i.e. ring-up, stable signal, ring-down) reaches a maximum of 1.6 V_{PP} within the first 140 μs, whereas with 4.2 the maximum amplitude is 20 mV_{PP}. Furthermore, examining the echo from the opposite acrylic wall of the chamber (starting at 218 μs), transducer 5.2 receives 200 mV_{PP} maximum, whereas transducer 4.2 only shows 20 mV_{PP}. This implicates a significant difference in sensitivity of the PCD elements, which was to be expected. Note, that transducer 4.2 and 5.1 have almost identical transmit efficiency and should therefore generate the equal acoustic pressure driven at similar voltages (i.e. Xdr 4.2 at 71.6 V_{PP}, Xdr 5.1 at 70 V_{PP}).

Figure 3.16 demonstrates, when using 7 or more cycles to drive the transducer, ring-up and ring-down are clearly separable in time. Increasing the number of cycles further, the transducer reaches a stable mode and the actual pulse manifests itself in the signal. In the FFT (Figure 3.14) the fundamental frequency, but no harmonic content can be observed. From the experiments it can be concluded that a transducer will never produce a *perfect* pulse. There will always be an introduction of additional phenomena, such as ringing. Varying the excitation pulse length (i.e. number of cycles), does not prevent ringing, but more cycles allows a transducer to reach its stable state.

4.2 Critical Ultrasound Parameters

In Table 3.2 the three important parameters when it comes to safety of an ultrasound application are shown. Note, calculations are done considering a duty cycle of 0.5%. Up to 80 V_{PP} at the impedance matching network for transducer 4.1, which essentially results in 572.8 V_{PP} at the transducer, the *MI* stays below 1, which implicates a low probability of causing cavitation. The method of calculating the *TIC* based on the measured acoustic pressure values represented a better way for us to estimate temperature rise at the skull. The high specific heat capacity of water and the sheer volume of water would make any temperature change highly improbable if we attempted to perform measurements in the wet tank. However, the low thermal index with a maximum of 0.74 indicates that there is hardly no rise in temperature at the skull to be expected. Ultimately, the calculated I_{SPTA} is well below the safety limit.

4.3 In-Vitro Studies

4.3.1 Human Skull Response and Impact

In 3.3.1 the impact of the human skull on the acoustic response is demonstrated. 3D field scans do not show signficant distortion if the skull bone is inserted in between the hydrophone and the transducer. In general, the acoustic field maintains its characteristic shape. Analysis in the time and frequency domain indicate, that there is no appreciable nonlinear generation or noticeable difference in harmonic signal representation depending on transducer driving voltages or distances between the transducer and the bone window. Therefore, it can be concluded that the skull does not cause nonlinear wave propagation and may be treated as attenuator only according to Table 3.3. Results shown in this table further indicate, that the acrylic walls of our pressure

chamber represent a good model to simulate the skull bone as their impact on the acoustic field is similar (i.e. attenuation only). The mean peak negative pressure loss measured with transducers 2.1 to 4.1 indicated in Table 3.3 results in 45%. This explains our demand for the highest achievable PCD element sensitivity.

4.3.2 Microbubble Response

Main objective of this research project was to study acoustic responses from microbubbles in biological tissue if they are excited by ultrasound. Our in-vitro studies were the first step to understand and characterize microbubble behavior when stimulated with our customized transducers. Migrating this knowledge to complex biological structures, such as the human brain is one of the biggest challenges.

4.3.2.a Studies in AIMS tank

Results shown in Figure 3.32, 3.33 and 3.34 should represent an example that we are in general able to detect microbubble activity in-vitro. In fact, this is one of the very few important conclusions that we were able to draw using this specific experimental setup with a flow system in place. For reasons explained in 2.8.3, we migrated the experiments to the acrylic chamber.

4.3.2.b Studies in Acrylic Chamber

Three main questions were answered by studying microbubble activity in the acrylic chamber. First, we examined the potential impact of various acoustic pressures on microbubble excitation. Second, we assessed changes in signal detection in relation to varying microbubble concentrations. Third, we transmitted through one of the acrylic walls from outside into the box that was filled with bubbly liquid and were able to detect microbubble activity.

As indicated in Table 3.4, we observed that there is an overall, noticeable stronger acoustic signal detection in presence of SonoVue compared to BR38. Furthermore, there was no linear relationship between output voltage and signal response for both agents. SonoVue performs best at lower driving voltages (i.e. 30 or 60 V_{PP}), whereas Br38 response was present once the transducer was driven at higher voltages. Br38 had the strongest overall response at 880 kHz and 120 V_{PP} with 18.2% of signals above threshold. On the contrary, SonoVue showed the strongest response at 880 kHz and 30 V_{PP} with 56.9% above threshold. Noteworthy is the generation and detection of ultra-harmonic content, such as low amplitude at 990 kHz, but more so at 1210 kHz in case of SonoVue. However, the ultra-harmonics are in general lower in amplitude than amplitudes of signals at frequencies 880, 1100 or 1320 kHz.

In the microbubble dose escalation studies (Table 3.5), microbubbles show a similar response pattern compared to the studies where they are excited with different acoustic pressure (i.e. impact of transducer driving voltage). Maximum signal response was achieve at 1100 kHz and 1.25 ml Br38 with 38.4% of signals above threshold and SonoVue at 1100 kHz and 0.6 ml with 56.8% of signals above threshold. SonoVue performs best at lower microbubble concentrations, whereas Br38 better at higher concentrations. Again, comparing both agents to each other with regard to their acoustic response, SonoVue performs better. Experiments performed if the

transducer is placed outside the acrylic chamber (i.e. Table 3.6) show, as expected less signal detected, except for some outliers at the higher transducer driving voltages at higher frequencies.

4.4 Animal Safety Studies

The intention behind these studies was to evaluate the potential risk of ultrasound in combination with microbubbles to cause brain damage or intracranial hemorrhage in normal, non-stroke animals. Furthermore, it should demonstrate an effect on rabbits that were pre-conditioned with strokes prior to application of ultrasound. Considering an acoustic intensity of 120 mW/cm^2 that the animals were exposed to within these safety studies, results shown in Table 3.7 and 3.8 proof that our application does not have any harmful effect on living biological tissue. In total, two rabbits deceased, but the cause of death was either Isoflurane-related or due to a severe stroke, hence not associated with our application.

It is noteworthy, that after the animal safety studies, we were able to reduce the acoustic intensity to 0.054 mW/cm^2, still being able to excite and detect microbubbles. This is due to significantly higher sensitivity of the transducers PCD element and the better understanding of microbubble specific responses.

One minor thought behind the studies was to proof the concept of transcranial microbubble detection in a living organism and extrapolate the acquired knowledge to the human body. However, due to the complicated experimental setup and the rabbits different anatomy, we were not able to get conclusive results in this regard.

4.5 Human Cadaver Studies

The main objective of experiments on the first head was to test for feasibility to detect and acquire acoustic response signals generated by brain tissue itself. Measurements on the second cadaver head were performed to test whether acoustic signals caused by microbubbles can be detected following transcranial ultrasound transmission. Another intended outcome was to test for differences in acoustic signal response between microbubble perfused and non-microbubbble perfused hemispheres.

Results of signals received from the first cadaver head indicate that tissue harmonics might be present and detectable. Responses mainly occurred at 440, 660 and, to some extent, at 880 kHz. They do not seem to appear to a noticeable extent at our other target frequencies at 1100 and 1320 kHz. However, for the second cadaver head, the pronounced nonlinear components evolve with increasing voltage, especially at the higher target frequencies (i.e. 880, 1100, 1320 kHz). In both cases, the use of the analog bandpass filter confirms the significant presence of tissue harmonics, which were observed in the non-filtered signal. The fact that using a combination of pulse inversion and analog bandpass filter (i.e. Figure 3.54 and 3.55) does not eliminate 440, 880, 1320 kHz strongly suggests, that these are true tissue responses. Another indicator is the 1100 kHz component that is hardly suppressed even though pulse inversion is applied.

4.6 Signal Detection and Analytical Methods

Again, FFT proofed to be a great tool to examine and characterize microbubble responses. Using the Support Vector Machine did not turn out to be a promising approach. After changing the ultrasound parameters to a significantly lower pulse duration and decreased measurement time, establishing a statistical method did not seem feasibly or necessary. The Gabor transform, as shown in the example Figures 3.35 and 3.36), confirmed the variance of amplitude of a single frequency component over time. Matched Filter results (e.g. Figures 3.37 ff) are good examples that this method covers the time-variant characteristics of microbubbles, the establishment of a detection threshold and the capability of operating in real-time.

CHAPTER 5

Summary

5.1 Transducers

All measurements that served the purpose of transducer characterization demonstrate, that duplicating transducers is very difficult to accomplish. The transmitting efficiency significantly improved by changing the dicing depth of the 1-3 composite material. Comparing the 4th to 5th transducer generation once again points out the remarkable difference in sensitivity between PVDF and PZT as sensing element.

5.2 Transcranial Assessments

At a transmit frequency of 220 kHz, an average loss in peak negative pressure of 45% was measured transmitting through the temporal bone window. Signals coming from microbubbles are still being detected at the same location as the transmitting source. Ultimately, the acrylic wall seems to be a good method to mimic bone structures as it has no other effect on the acoustic field rather than attenuation.

5.3 Microbubbles

In general, both agents, SonoVue and Br38, react differently to certain acoustic pressures. Furthermore, Br38 requires higher acoustic pressure than SonoVue in order to emit detectable signals. Possible reason for that may be differences in size distribution and their molecular structure. However, Br38 is known to be used with higher frequency applications and therefore an inert behavior at low frequencies such as 220 kHz can be expected. Referring to the dose escalation results, concentrations definitely have an impact on the acoustic responses, although a behavioral pattern can not be observed.

5.4 Safety Aspect

Based on acoustic measurements, we were able to determine all critical ultrasound parameters and to proof that any of our application is well below safety limits in diagnostic ultrasound set by regulatory authorities worldwide. In addition to that, studies on the rabbits showed that our ultrasound application had no harmful effect on living biological tissue. Rabbits with and without stroke did not show any sign of different behavior after treatment compared to before. Furthermore, all serological tests showed no abnormalities. The positive outcome implicates that there is no potential risk linked to ultrasound parameters used in the animal safety studies and neither for such that are lower in amplitude, duty cycle or measurement time.

5.5 Human Cadaver Studies

Studies performed on postmortem tissue were extremely valuable as the experimental setup came probably closest to real life conditions compared to all other methods that we used to characterize tissue and microbubble responses. For the first time, we were able to show non-linear human tissue response as indicated by the pronounced occurrence of tissue harmonics. However, since cadaver preparation did not allow to perfuse the brain with microbubbles, the characterization of microbubble response in human tissue remains open.

CHAPTER 6

Outlook

By using 220 kHz driving pulses of low acoustic intensities to evoke tissue harmonics and microbubble responses, we generated a novelty in the field of medical ultrasound. The groundbreaking knowledge gained within this work is extremely valuable for development of noninvasive, safe, energy- and cost-efficient, transcranial ultrasound technologies. This includes monitoring, diagnosis and treatment of conditions within the human brain. Examples are devices that continuously measure intracranial pressure (ICP), devices that rapidly diagnose strokes in patients on their way to a hospital, or such that are able to treat hemodynamic disturbances within the brain. These are only a few examples of what is feasible if we successfully use the outcome of the performed research for development of technologies that have potential to significantly improve todays healthcare.

Bibliography

[1] Ahmadi, F., McLoughlin, I. V., Chauhan, S., and Ter Haar, G., 2012. Bio-effects and safety of low-intensity, low-frequency ultrasonic exposure. *Progress in Biophysics and Molecular Biology*, 108(3):119–138.

[2] Al-Farsi, K., Siddiqui, A. A., Sharef, Y. W., Al-Belushi, A. K., Al-Hashim, H., Al-Ghailani, M., and Johnston, W. J., 2013. Hemorrhagic cardioembolic stroke secondary to a left ventricular thrombus: a therapeutic dilemma. *Oman Medical Journal*, 28(1):56–59.

[3] Arda, K., Ciledag, N., Aktas, E., Arıbas, B. K., and Köse, K., 2011. Quantitative assessment of normal soft-tissue elasticity using shear-wave ultrasound elastography. *American Journal of Roentgenology*, 197(3):532–536.

[4] Averkiou, M., Mannaris, C., Bruce, M., and Powers, J., 2008. Nonlinear pulsing schemes for the detection of ultrasound contrast agents.

[5] Bailey, M. R., Khokhlova, V., Sapozhnikov, O. A., Kargl, S., and Crum, L. A., 2003. Physical mechanisms of the therapeutic effect of ultrasound. *Acoustical Physics*, 49(4):369–388.

[6] Barnett, S., Haar, G., Ziskin, M., Nyborg, W. L., Maeda, K., and Bang, J., 1994. Current status of research on biophysical effects of ultrasound. *Ultrasound Med Biol*, 20(3):205–218.

[7] Broussalis, E., Trinka, E., Killer, M., Harrer, A., McCoy, M., and Kraus, J., 2012. Current therapies in ischemic stroke, part b, future candidates in stroke therapy and experimental studies. *Drug Discov Today*, 17(13-14):671–684.

[8] Burgess, A. and Hynynen, K., 2014. Drug delivery across the blood-brain barrier using focused ultrasound. *Expert Opin Drug Deliv*, 11(5):711–721.

[9] Cochran, S., 2012. *Piezoelectricity and basic configurations for piezoelectric ultrasonic transducers*, pages 3–35. Woodhead Publishing Limited.

[10] Cosgrove, D. and Harvey, C., 2009. Clinical uses of microbubbles in diagnosis and treatment. *Med Biol Eng Comput*, 47(8):813–826.

[11] Couture, O., Aubry, J. F., Montaldo, G., Tanter, M., and Fink, M., 2008. Suppression of tissue harmonics for pulse-inversion contrast imaging using time reversal. *Physics in Medicine and Biology*, 53(19):5469–5480.

[12] Cox, B., 2013. Acoustics for ultrasound imaging.

[13] Daffertshofer, M., Gass, A., Ringleb, P., Sitzer, M., Sliwka, U., Els, T., Sedlaczek, O., Koroshetz, W. J., and Hennerici, M. G., 2005. Transcranial low-frequency ultrasound-mediated thrombolysis in brain ischemia: increased risk of hemorrhage with combined ultrasound and tissue plasminogen activator: results of a phase ii clinical trial. *Stroke*, 36(7):1441–1446.

[14] Deng, C. X., 2010. Targeted drug delivery across the blood-brain barrier using ultrasound technique. *Ther Deliv*, 1(6):819–848.

[15] Dirnbacher, M., 2013. *Effects of Ultrasound induced Cavitation Mechanisms on Biological Systems*. Thesis.

[16] Duck, A., 2002. Nonlinear acoustics in diagnostic ultrasound. *Ultrasound Med Biol*, 28:1–18.

[17] Ensminger, D. and Bond, L., 2011. *Elastic Wave Propagation and Associated Phenomena*. CRC Press.

[18] Franc, J.-P., 2007. *The Rayleigh-Plesset equation: a simple and powerful tool to understand various aspects of cavitation*. Fluid Dynamics of Cavitation and Cavitating Turbopumps.

[19] Hendee, W. and Ritenour, E., 2002. *Ultrasound Waves*, book section 19. 4 edition.

[20] Hoskins, P., Martin, K., and Thrush, A., 2010. *Diagnostic Ultrasound Physics and Equipment*, book section 15, page 227.

[21] Jameson, B. and Manduchi, R. Estimation and detection in the presence of ringing noise. In *Ultrasonics Symposium (IUS)*, pages 2032–2035.

[22] Lauterborn, W. and Mettin, R., 1999. Nonlinear bubble dynamics: response curves and more. *Sonochemistry and Sonoluminescence*, pages 63–72.

[23] Matte, G., 2010. *Exploiting Ultrasound Harmonics*. Thesis.

[24] Meairs, S. and Culp, W., 2009. Microbubbles for thrombolysis of acute ischemic stroke. *Cerebrovasc Dis*, 27 Suppl 2:55–65.

[25] Naranjo, D., Arkuszewski, M., Rudzinski, W., Melhem, E. R., and Krejza, J., 2013. Brain ischemia in patients with intracranial hemorrhage: pathophysiological reasoning for aggressive diagnostic management. *Neuroradiol J*, 26(6):610–628.

[26] Nelson, T. R., Fowlkes, J. B., Abramowicz, J. S., and Church, C. C., 2009. Ultrasound biosafety considerations for the practicing sonographer and sonologist. *Journal of Ultrasound in Medicine*, 28(2):139–150.

[27] Poon, C., McMahon, D., and Hynynen, K., 2016. Noninvasive and targeted delivery of therapeutics to the brain using focused ultrasound.

[28] Powers, J., Averkiou, M., and Bruce, M., 2009. Principles of cerebral ultrasound contrast imaging. *Cerebrovasc Dis*, 27 Suppl 2:14–24.

[29] Purves, D., Augustine, G., and Fitzpatrick, D., 2001. *The Blood Supply of the Brain and Spinal Cord*. Neuroscience. 2 edition.

[30] Quistgaard, J. U., Desilets, C., and Martin, P., 2010. High intensity focused ultrasound. *The European Aesthetic Guide*.

[31] Romero, J. R., Pikula, A., Nguyen, T. N., Nien, Y. L., Norbash, A., and Babikian, V. L., 2009. Cerebral collateral circulation in carotid artery disease. *Current Cardiology Reviews*, 5(4):279–288.

[32] Shaw, G. J., Meunier, J. M., Lindsell, C. J., and Holland, C. K., 2008. Tissue plasminogen activator concentration dependence of 120 khz ultrasound-enhanced thrombolysis. *Ultrasound Med Biol*, 34(11):1783–1792.

[33] Shen, C.-C., Chou, Y.-H., and Li, P. C., 2005. Pulse inversion techniques in ultrasonic nonlinear imaging. *Journal of Medical Ultrasound*, 13(1):3–17.

[34] Sherrit, S. and Mukherjee, B. K., 2007. Characterization of piezoelectric materials for transducers.

[35] Svilainis, L., Dumbrava, V., and G., M., 2008. Ultrasonic generator-transducer combined performance enhancement. *Journal of Applied Electromagnetism*, 10(2):35–44.

[36] Verweij, M. D. and van Dongen, K. W. A., 2012. Using nonlinear distortion to our benefit: Higher harmonic imaging of medical ultrasound. *Electromagnetics in Advanced Applications*, pages 531–534.

[37] Voie, A., Dirnbacher, M., Fisher, D., and Hoelscher, T., 2014. Parametric mapping and quantitative analysis of the human calvarium. *Comput Med Imaging Graph*, 38(8):675–682.

[38] Wallace, K. D., Lloyd, C. W., Holland, M. R., and Miller, J. G., 2007. Finite amplitude measurements of the nonlinear parameter b/a for liquid mixtures spanning a range relevant to tissue harmonic mode. *Ultrasound Med Biol*, 33(4):620–629.

[39] Wu, J. and Nyborg, W. L., 2008. Ultrasound, cavitation bubbles and their interaction with cells. *Advanced Drug Delivery Reviews*, 60(10):1103–1116.

[40] Yawada, S. and An, J. W., 2015. Performance evaluation of matched filter detection based on non-cooperative spectrum sensing in cognitive radio network. *International Journal of Computer Networks and Communications Security*, 3(12):442–446.

List of Figures

1.1 The major arteries of the brain. (A) Ventral view. The enlargement of the boxed area shows the circle of Willis. Lateral (B) and (C) midsagittal views showing anterior, middle, and posterior cerebral arteries. (D) Idealized frontal section showing course of middle cerebral artery[29] . . . 3
1.2 Cerebral Infarction Example of a cerebral infarction on the left hemisphere due to a M1 thrombosis of the middle cerebral artery: computed tomography (CT) scan with a demarcation zone (left side), CT angiography which shows a stop of flow (see arrow in the middle), DW MRI (diffusion weighted magnetic resonance imaging) which shows the extend of edema caused in the zone of tissue infarction (courtesy Department of Neuroradiology, Medical University of Vienna)[15] . . . 4
1.3 Resonance Geometries [34] . . . 8
1.4 Transducer Equivalent Circuit . . . 9
1.5 Waveform Steeping . . . 13

2.1 Acrylic Pressure Chamber . . . 19
2.2 Dual-Element Transducer . . . 20
2.3 Impedance Matching Circuit for Transducer 5.1, Input right, Output left. Power plug for Mini Fan from Top . . . 22
2.4 Analog Filter Insertion Loss Measurement . . . 24
2.5 Insertion Loss Xdr 4.1 . . . 24
2.6 Insertion Loss Xdr 4.2 . . . 25
2.7 Insertion Loss Xdr 5.1 . . . 25
2.8 Insertion Loss Xdr 5.2 . . . 26
2.9 AIMS Simple Measurement Overview (www.ondacorp.com) . . . 27
2.10 Example Power Amplifiers Linearity, Output Voltage/ Peak Negative Pressure . . . 30
2.11 LabVIEW Code for Automated Acquisition . . . 31
2.12 LabVIEW Transmission Control . . . 31
2.13 LabVIEW Acquisition Control . . . 32
2.14 Example of 5 ms 220 kHz Driving Pulse with initial 10% Ramp-Up . . . 34
2.15 Principle of Pulse Inversion . . . 35
2.16 Impedance Measurement Setup . . . 37
2.17 Acoustic Field 3D Scan Measurements Setup . . . 37
2.18 Lateral-Posterior (Position 1) . . . 40

2.19 Lateral-Superior (Position 2) 41
2.20 Lateral-Anterior (Position 3) 41
2.21 Overview Setup with PXI and AIMS tank 44
2.22 Flow Studies Schematic, Front View 44
2.23 Flow Studies Schematic, Side View 45
2.24 Setup Measurements with Acrylic Chamber 46
2.25 Animal Safety Studies Setup 47
2.26 Transducer Positioning, Human Cadaver Studies 49
2.27 Human Cadaver Studies, PXI setup 49
2.28 Example for SVM Result 51
2.29 Example of a 2 ms Pulse examined with Gabor Transform 52
2.30 Example of 80 μs Pulse analyzed with a Matched Filter tuned to 1.1 MHz 53

3.1 Xdr 5.1 Transmitter, Matched Impedance 56
3.2 Xdr 5.2 Transmitter, Matched Impedance 57
3.3 Xdr 5.1 Receiver Impedance 58
3.4 Xdr 5.2 Receiver Impedance 59
3.5 Acoustic Field Scans 3D, Xdr 4.1 61
3.6 Acoustic Field Scans 3D, Xdr 4.2 62
3.7 Acoustic Field Scans 3D, Xdr 5.1 63
3.8 Acoustic Field Scans 3D, Xdr 5.2 64
3.9 880 kHz PNP distribution on Xdr5.2 PCD element 66
3.10 1100 kHz PNP distribution on Xdr5.2 PCD element 67
3.11 1320 kHz PNP distribution on Xdr5.2 PCD element 68
3.12 Received Time Signal, Free Field, Xdr5.1, 70 V_{PP} 69
3.13 Time Domain Analysis, Received Signal, Free Field, Xdr5.1, 70 V_{PP}, 0 to 200 μs . 69
3.14 Frequency Domain Analysis, Received Signal, Free Field, Xdr5.1, 70 V_{PP}, 38.4 to 89.42 μs 70
3.15 Time Domain Analysis, Received Signal, Free Field, Xdr5.1 at 70 V_{PP} and Xdr4.2 at 71.6 V_{PP}, 0 to 300 μs 70
3.16 Time Signal X52; Overlay 1 cycle, 3, 5, 7, 10 cycles 70
3.17 Lateral-Posterior (Position 1) 72
3.18 Lateral-Superior(Position 2) 73
3.19 Lateral-Anterior(Position 3) 74
3.20 Overlay Time Signal at 0(blue), 5(red), 10(green), 20(lightblue), 30 mm(yellow) Distance between X52 and Temporal Bone Window, Position 1 76
3.21 Overlay FFTs at 0(blue), 5(red), 10(green), 20(lightblue), 30 mm(yellow) Distance between X52 and Temporal Bone Window, Position 1 76
3.22 Skull Response, Time Signal, X52 to Skull Distance 0 mm, 60(blue)180(red)/360 V_{PP}(green) 77
3.23 Skull Response, FFT, X52 to Skull Distance 0 mm, 60(blue)/180(red)/360 V_{PP}(green) 77
3.24 Skull Response, Time Signal, X52 to Skull Distance 5 mm, 60(blue)/180(red)/360 V_{PP}(green) 77
3.25 Skull Response, FFT, X52 to Skull Distance 5 mm, 60(blue)/180(red)/360 V_{PP}(green) 78
3.26 Skull Response, Time Signal, X52 to Skull Distance 10 mm, 60(blue)/180(red)/360 V_{PP}(green) 78

3.27 Skull Response, FFT, X52 to Skull Distance 10 mm, 60(blue)/180(red)/360 V_{PP}(green) 78
3.28 Skull Response, FFT, X52 to Skull Distance 20 mm, 60(blue)/180(red)/360 V_{PP}(green) 79
3.29 Skull Response, Time Signal, X52 to Skull Distance 20 mm, 60(blue)/180(red)/360 V_{PP}(green) 79
3.30 Skull Response, Time Signal, X52 to Skull Distance 30 mm, 60(blue)/180(red)/360 V_{PP}(green) 79
3.31 Skull Response, FFT, X52 to Skull Distance 30 mm, 60(blue)/180(red)/360 V_{PP}(green) 80
3.32 FFT Overlay of Baseline(blue) and SonoVue(red) Dataset, Xdr 4.1, Driving Voltage 96 V_{PP} 81
3.33 FFT Overlay of Baseline(blue) and SonoVue(red) Dataset, Xdr 4.1, Driving Voltage 120 V_{PP} 82
3.34 FFT Overlay of Baseline(blue) and SonoVue(red) Dataset, Xdr 4.1, Driving Voltage 144 V_{PP} 82
3.35 Gabor Transform of Baseline Dataset, Xdr4.1, Driving Voltage 144 V_{PP} 83
3.36 Gabor Transform of SonoVue Dataset, Xdr4.1, Driving Voltage 144 V_{PP} 83
3.37 880 kHz Matched Filter, Baseline and Br38 at 30 V_{PP} input voltage 84
3.38 880 kHz Matched Filter, Baseline and SonoVue at 30 V_{PP} input voltage 84
3.39 1100 kHz Matched Filter, Baseline and Br38 at 30 V_{PP} input voltage 85
3.40 1100 kHz Matched Filter, Baseline and SonoVue at 30 V_{PP} input voltage 85
3.41 1320 kHz Matched Filter, Baseline and Br38 at 30 V_{PP} input voltage 85
3.42 1320 kHz Matched Filter, Baseline and SonoVue at 30 V_{PP} input voltage 86
3.43 Cadaver Head 1, Xdr 5.2, 5 to 25 V_{PP}(blue,red,green,lightblue,yellow respectively), Position 1, FFT, without analog Filter 89
3.44 Cadaver Head 1, Xdr 5.2, 5 to 25 V_{PP}(blue,red,green,lightblue,yellow respectively), Position 1, FFT, with analog Bandpass Filter 89
3.45 Cadaver Head 1, Xdr 5.2, 30 to 50 V_{PP}(blue,red,green,lightblue,yellow respectively), Position 1, FFT, without analog Filter 90
3.46 Cadaver Head 1, Xdr 5.2, 30 to 50 V_{PP}(blue,red,green,lightblue,yellow respectively), Position 1, FFT, with analog Bandpass Filter 90
3.47 Cadaver Head 1, Xdr 5.2, 5 to 25 V_{PP}(blue,red,green,lightblue,yellow respectively), Position 2, FFT, with analog Bandpass Filter 91
3.48 Cadaver Head 1, Xdr 5.2, 5 to 25 V_{PP}(blue,red,green,lightblue,yellow respectively), Position 3, FFT, with analog Bandpass Filter 91
3.49 Cadaver Head 1, Xdr 5.2, 5 to 25 V_{PP}(blue,red,green,lightblue,yellow respectively), Position 4, FFT, with analog Bandpass Filter 92
3.50 Cadaver Head 2, Xdr 5.2, 5 to 25 V_{PP}(blue,red,green,lightblue,yellow respectively), FFT, without analog Bandpass Filter 93
3.51 Cadaver Head 2, Xdr 5.2, 30 to 50 V_{PP}(blue,red,green,lightblue,yellow respectively), FFT, without analog Bandpass Filter 93
3.52 Cadaver Head 2, Xdr 5.2, 5 to 25 V_{PP}(blue,red,green,lightblue,yellow respectively), FFT, with analog Bandpass Filter 94
3.53 Cadaver Head 2, Xdr 5.2, 30 to 50 V_{PP}(blue,red,green,lightblue,yellow respectively), FFT, with analog Bandpass Filter 94
3.54 Cadaver Head 2, Xdr 5.2, 5 to 25 V_{PP}(blue,red,green,lightblue,yellow respectively), FFT, with analog Bandpass Filter, with Pulse Inversion 95

3.55 Cadaver Head 2, Xdr 5.2, 30 to 50 V_{PP}(blue,red,green,lightblue,yellow respectively), FFT, with analog Bandpass Filter, with Pulse Inversion 95

List of Tables

2.1 Impedance Matching Circuit Transformation 21
2.2 Data Acquisition Loops 35

3.1 PCD 5.2 Sensitivity Measurements 65
3.2 Mechanical Index(MI), Thermal Index Cranial(TIC), I_{SPTA} 71
3.3 Transcranial Field Assessments, PNP Loss 75
3.4 Impact of Driving Voltage on Microbubble Response 86
3.5 Microbubble Dose Escalation 87
3.6 Measurements through Acrylic Chamber Wall 87
3.7 Safety and Survival Analysis 88
3.8 Behavioral Analysis 88

Acronyms

ABP arterial blood pressure

AIMS Acoustic Intensity Measurement System

ADC Analog-to-digital converter

BBB blood-brain barrier

BURL Brain Ultrasound Research Laboratory

CT computed tomography

DAQ data acquisition module

DC duty cycle

DW-MRI Diffusion-Weighted-Magnetic Resonance Imaging

FF free field

FFT Fast Fourier Transform

FUS focused ultrasound

ICP intracranial pressure

$\mathbf{I_{SPTA}}$ spatial peak-temporal average intensity

MB microbubble

MI mechanical index

MPP Matrix Metallo Proteinase

MRI Magnetic Resonance Imaging

NIHSS National Institute of Health Stroke Scale

PCD passive cavitation detection

P_{fa} probability of false alarm

PNP peak negative pressure

PRT pulse repetition time

PVDF polyvinylidene fluoride

PW pulse width

PZT lead zirconate titanate

SCEM Small Clot Embolic Stroke

SNR signal-to-noise ratio

TDS total dissolved solids

THI tissue harmonic imaging

TI thermal index

TIC thermal index cranial

TMDS Technical Data Management Streaming

TPA tissue plasminogen activator

VI virtual instrument

V_{PP} voltage peak-to-peak

V_{RMS} voltage root mean square

X transducer

Xdr transducer

CURRICULUM VITAE

First Name: Maximilian
Last Name: Dirnbacher

Date of Birth: 29th September 1985
Place of Birth: Vienna, AUSTRIA
Nationality: AUSTRIA

EXPERIENCE

01/2015 – 12/2015 **BURL Concepts, Inc.** San Diego, California, USA
10/2013 – 09/2014

- Internship/ Trainee focusing on transcranial Ultrasound

10/2012 – 03/2013 **Brain Ultrasound Research Laboratory Departments of Radiology and Neurosciences University of California, San Diego** San Diego, California, USA

- Research Activities using focused Ultrasound for the Master Thesis „Effects of Ultrasound induced Cavitation Mechanisms on biological Systems".

07/2012 – 09/2012 **B.Braun Austria GmbH** Graz, AUSTRIA

- Development of an Oxygen- Diffusion Model with the aim to predict the Oxygen- Diffusion in Glucose Sensors; Python was used to create the Model
- Testing of different Python Codes by Unit Tests; the Codes evaluate different parameters collected by the Glucose Sensors

08/2010 **Laboratory Dr. Winter (Research Activities)** Vienna, AUSTRIA

- Laboratory Assistant; Testing and Evaluation of biological Samples of Patients; Western Blots; PCR

08/2009
02/2009
07/2008 – 08/2008
07/2007 – 09/2007
Siemens AG (Programming and Development of Systems) Vienna, AUSTRIA

- Development of Visual Basic Codes for MS Word, MS Excel; Application of Databases, Oracle, MS Access; Programming of Macros in MS Word and MS Excel

07/2007 – 08/2007 **Pluradent (Service, Engineer)** Vienna, AUSTRIA

- Installation, Maintenance and Repair of Biomedical Devices at Dentist's Surgeries or at the Company

08/2006 – 09/2006	**Siemens AG (Programming and Development of Systems)**	Vienna, AUSTRIA

- Development of the Importfunction of XML- files for Oracle Siebel

06/2005 – 07/2005	**Austrian Airlines (Booking, Sales)**	London, GB

- Administrative Duties

08/2004 – 11/2004	**Immoplus projektmanagement Ges.m.b.H. (Secretary)**	Vienna, AUSTRIA
07/2002	**Intersport (Salesman)**	Tyrol, AUSTRIA
	Several times involved in the organisation of EA- Generali Tennis tournament	Tyrol, AUSTRIA

EDUCATION

07/2013 – present	**Technical University of Vienna, AUSTRIA** **Doctoral Program, Applied Physics** Main Focus on Ultrasound
10/2010 – 06/2013	**Technical University of Vienna, AUSTRIA** **Dipl.-Ing. (M.Sc.), Biomedical Engineering** Main Focus on Medical Physics & Imaging
10/2010	**Technical University of Graz, AUSTRIA** **B.Sc., Biomedical Engineering** Main Focus on Molecular Bioengineering
1996 – 2004	Albertus Magnus Gymnasium, Vienna, AUSTRIA Baccalaureat
2004-2005	Military Service

SCHOLARSHIPS

2012	Marshall Plan Scholarship (Austrian Marshall Plan Foundation)
2014	Stipendium für kurzwissenschaftliche Arbeiten im Ausland

PUBLISHED WORK:

Articles:

„Parametric mapping and quantitative analysis of the human“ (with A. Voie, D. Fisher, T. Hoelscher), Comput Med Imaging Graph (July 2014)

LANGUAGES

English: fluent

French: working knowledge

Language Studies at Great Britain, Scottland, USA, Sweden

ADDITIONAL SKILLS & ACHIEVEMENTS

Matlab, Python, MS Word, MS Excel (full working knowledge)

MS PowerPoint and MS Access (basic knowledge)

Programming languages: Labview, C++, programming in Matlab and Python, Visual Basic

Graphical design (Autodesk Maya, GIMP, Rhino)